



HAL
open science

Average Current Enhancement of Laser-Plasma Accelerators for Industrial Applications

Lorenzo Martelli

► **To cite this version:**

Lorenzo Martelli. Average Current Enhancement of Laser-Plasma Accelerators for Industrial Applications. Plasma Physics [physics.plasm-ph]. Institut Polytechnique de Paris, 2024. English. NNT : 2024IPPAE012 . tel-04791204

HAL Id: tel-04791204

<https://theses.hal.science/tel-04791204v1>

Submitted on 19 Nov 2024

HAL is a multi-disciplinary open access archive for the deposit and dissemination of scientific research documents, whether they are published or not. The documents may come from teaching and research institutions in France or abroad, or from public or private research centers.

L'archive ouverte pluridisciplinaire **HAL**, est destinée au dépôt et à la diffusion de documents scientifiques de niveau recherche, publiés ou non, émanant des établissements d'enseignement et de recherche français ou étrangers, des laboratoires publics ou privés.



INSTITUT
POLYTECHNIQUE
DE PARIS

NNT : 2024IPPAAE012

Thèse de doctorat



Average Current Enhancement of Laser-Plasma Accelerators for Industrial Applications

Thèse de doctorat de l'Institut Polytechnique de Paris
préparée à l'École nationale supérieure de techniques avancées

École doctorale n°626 École doctorale de l'Institut Polytechnique de Paris (EDIPP)
Spécialité de doctorat : Physique

Thèse présentée et soutenue à Palaiseau, le 19 septembre 2024, par

LORENZO MARTELLI

Composition du Jury :

Victor Malka Professeur des Universités, Weizmann Institute of Science (Department of Physics of Complex Systems)	Président
Sandrine Dobosz Dufrénoy Directrice de Recherche, Commissariat à l'Énergie Atomique et aux Énergies Alternatives (CEA)	Rapporteur
Emmanuel d'Humières Professeur des Universités, Université de Bordeaux (UMR 5107)	Rapporteur
Kevin Cassou Ingénieur de Recherche, Laboratoire de Physique des 2 Infinis - Irène Joliot-Curie (UMR 9012)	Examineur
Kristjan Pöder Subgroup Leader, Deutsches Elektronen-Synchrotron DESY (MPA4)	Examineur
Cédric Thauray Directeur de Recherche, Laboratoire d'Optique Appliquée (UMR 7639)	Directeur de thèse
Xuan Quyen Dinh Ingénieur, Thales-AVS (MIS)	Co-encadrant

*Ai miei genitori,
A Federico e a Sasha*

Acknowledgements

I want to first thank the jury members for their interest in my work. Victor Malka for accepting the role of president, Sandrine Dobosz Dufrénoy and Emmanuel d’Humières for examining this manuscript, and Kevin Cassou and Kristjan Pöder for being part of the jury.

The results of this manuscript have been obtained over more than three years of research at LOA and Thales-MIS. I thank Stéphane Sebban, LOA’s director, and Rodolphe Marchesin, Thales-MIS group leader, for their support and the opportunity to work with their teams.

Cédric Thauray, my supervisor at LOA, has always stimulated my interest with new challenges. I am deeply grateful for his mentorship. I am equally thankful to Xuan Quyen Dinh, my co-supervisor at Thales-MIS, for his enthusiasm and dedication, which significantly contributed to the success of this thesis. Henri Kraft from Thales-MIS also supervised my work and consistently showed genuine care and support, for which I am sincerely grateful.

During my Ph.D., I worked closely with the UPX team. Special thanks to Olena Kononenko, Julien Gautier, Jean-Philippe Goddet, Amar Tafzi, and Pascal Rousseau for their crucial help with the experimental activities. I also want to thank Igor Andriyash, Alessandro Flacco and Jonathan Wheeler from the APPLI team for their readiness to help. Thanks to Thomas Lavergne, Grégoire Fabreges, and Sébastien Brun, who were extremely helpful in designing and developing essential mechanical parts.

Many thanks to all my fellow Ph.D. students and colleagues. Kosta Oubrerie, Adam Traoré, and Camilla Giaccaglia have been invaluable colleagues at LOA and good friends. Thank you for your sense of humor and support. I would also like to extend my gratitude to Adeline Kabacinski and Erwan Morel, who shared the office with me.

Lastly, I thank the LOA administration office, which has always been extraordinarily helpful and efficient: Patricia Toullier, Catherine Buljore, Sandrine Tricaud, and Magali Tutou.

Author's Role

A brief statement is provided below to help the reader identify the author's contributions. The author conducted the measurements, analysis, and created the graphs presented in this work, except where otherwise acknowledged.

The author developed the gas target and magnetic dipoles discussed in Chapter 3, which were essential for the experimental campaign detailed in Chapter 4. This development utilized commercial software available at LOA and Thales AVS-MIS. Henri Kraft (Thales AVS-MIS) provided valuable input for running the magnetostatic simulations. Thomas Lavergne, Adam Traoré and Grégoire Fabrèges also helped with the design of the novel electron spectrometer proposed in Chapter 3.

The activities described in Chapter 4 were carried out by the author who prepared the experiment and performed data acquisition with the assistance of the UPX team. The dose reconstruction was performed with the help of Alessandro Flacco (APPLI) and Camilla Giaccaglia (APPLI - Institut Curie).

The code FBPIC-Electric Work Profiler, discussed in Chapter 5, was developed by the author in collaboration with Igor Andriyash (APPLI). Additionally, the PIC simulations presented in Chapter 5 were performed by the author at the National Computation Center TGCC, and also using LOA's CPU cluster ELSA and GPU HPC node Solaris.

In the Conclusion and Outlook, we briefly outline the results of a laser-plasma-based X-ray radiography experiment performed using the Salle Sheril laser system at LOA (i.e., Fig. 5.22). This experiment was carried out by Olena Kononenko, Erwan Morel, Achraf Ayeb, and Amar Tafzi (UPX), in collaboration with Jonathan Wheeler (APPLI).

Résumé en Français

L'interaction entre une impulsion laser intense (i.e., $I > 10^{18}$ W/cm²) et un plasma est un sujet qui intéresse la communauté scientifique depuis les années 80, quand T. Tajima et J. M. Dawson ont proposé de générer des oscillations dans des plasmas de densités $n_e > 10^{18}$ cm⁻³ en exploitant la force pondéromotrice d'une impulsion laser. La formation d'une onde plasma dans le sillage du laser permet la formation des gradients accélérateurs qui dépassent 100 GV/m, soit trois à quatre ordres de grandeur plus élevés que ceux des systèmes conventionnels. Cela ouvre la voie à la réalisation d'accélérateurs compacts, représentant une alternative économique aux accélérateurs linéaires actuels et aux cavités à radiofréquence. Aujourd'hui, par exemple, il est possible d'accélérer un faisceau d'électrons de quelques picocoulombs à environ 1 GeV sur une distance d'un centimètre de plasma. En outre, plusieurs efforts ont été déployés pour produire des faisceaux d'électrons monochromatiques et stables, à faible émittance et hautement énergétiques. Ces avancées prometteuses dans les accélérateurs laser-plasma offrent des perspectives révolutionnaires pour la recherche en physique des hautes énergies et pourraient potentiellement transformer le domaine des accélérateurs de particules en réduisant les coûts. Bien que ces résultats démontrent le potentiel de ces dispositifs, les propriétés des faisceaux accélérés par laser-plasma restent encore loin de celles des systèmes conventionnels. Par exemple, les accélérateurs linéaires médicaux actuels peuvent produire entre 10 à 100 microampères, tandis que les accélérateurs laser-plasma ne délivrent que quelques dizaines de nanoampères. Une manière directe d'augmenter le courant moyen des accélérateurs laser-plasma consiste à augmenter la charge du faisceau. L'utilisation de gaz à numéro atomique élevé tels que l'azote et l'argon s'est avérée efficace pour augmenter la charge au-delà du nano-coulomb. L'emploi d'un dopant comme l'azote ou d'un gaz pur à numéro atomique élevé facilite en effet le piégeage des électrons sur une ou plusieurs périodes de plasma à travers l'injection par ionisation. Une fois piégés, les électrons sont ensuite accélérés par le champ électrique du plasma, produisant généralement de larges spectres d'énergie atteignant quelques dizaines de MeV.

L'objectif principal de cette thèse de doctorat est d'augmenter le courant moyen

des accélérateurs laser-plasma à faible énergie, en particulier dans la gamme de quelques MeV. Cela pourrait être particulièrement intéressant pour des applications à faible énergie qui ne requièrent pas de faisceaux d'électrons monoénergétiques, telles que celles proposées par le projet européen *Multiscan 3D - Horizon 2020*, dédié au contrôle du fret aux douanes. Notamment, l'objectif du projet Multiscan 3D est de développer une technique révolutionnaire de génération de rayons X utilisant une source d'électrons laser-plasma. Cela permettrait d'améliorer les performances, l'interopérabilité et la sécurité, tout en réduisant le temps de contrôle et en minimisant l'impact sur les utilisateurs.

L'étude de cette thèse a été menée à travers des expériences utilisant le système laser de 60 térawatts de la Salle Jaune du Laboratoire d'Optique Appliquée, capable de fournir des impulsions de 30 fs. En explorant différentes densités plasma, énergies laser, cibles gazeuses et degré de focalisation nous identifions les conditions pour produire des faisceaux d'électrons hautement divergents (i.e., > 100 mrad), de quelques MeV avec des charges de 5 à 30 nC et une efficacité maximale de conversion d'énergie du laser vers les électrons d'environ 14 %, l'une des plus élevées jamais mesurées. En considérant les futurs systèmes laser qui promettent d'atteindre des puissances moyennes d'environ 100 W, ces configurations pourraient ouvrir la voie à la production de faisceaux d'électrons accélérés par laser-plasma avec des courants moyens supérieurs à 1 microampère, dépassant l'état de l'art actuel. Afin de mener les expériences, nous avons conçu une buse supersonique en verre en collaboration avec le laboratoire FTMC en Lituanie. De plus, nous avons développé des dispositifs essentiels pour l'activité expérimentale, notamment des dipôles magnétiques permanents permettant de dévier les électrons vers des écrans scintillants pour effectuer la spectrométrie des faisceaux produits.

Les travaux de cette thèse ont également été consacrés aux simulations Particle-In-Cell (PIC), permettant d'étudier en profondeur la physique des configurations explorées expérimentalement. L'étude numérique a permis d'identifier les principaux mécanismes d'accélération. Grâce à un outil numérique que nous avons spécifiquement développé pour le traitement des résultats des simulations PIC, nous démontrons que la plupart des électrons sont accélérés par la force pondéromotrice du laser. Notamment, nous observons que la majorité des particules ne sont pas injectées dans les ondes du plasma, mais glissent plutôt sur l'impulsion laser en gagnant une faible énergie de l'ordre de quelques MeV grâce à la force pondéromotrice même du laser.

Contents

Acknowledgements	i
Author's Role	iii
Résumé en Français	v
Introduction	1
1 Physics of Laser-Plasma Accelerators	5
1.1 Laser-Plasma Physics Fundamentals	6
1.1.1 Electromagnetic Waves in Plasmas	6
1.1.2 Ionization Mechanisms	11
1.1.3 Ponderomotive Force and Non-Linear Effects	16
1.2 Particle Acceleration in a Plasma Wave	21
1.2.1 Linear Regime	21
1.2.2 Non-Linear Regime and Wave-Breaking	24
1.2.3 Electron Injection and Acceleration	25
1.2.4 Limitations of Laser-Plasma Accelerators	40
1.3 State of the Art	41
1.4 Conclusion	42
2 Methods	43
2.1 Numerical Simulations of Laser-Plasma Accelerators	44
2.1.1 Particle-In-Cell Method	44
2.1.2 FBPIC: Fourier-Bessel Particle-In-Cell	48

2.2	Salle Jaune Laser System	49
2.3	Diagnostics	51
2.3.1	Electron Spectrometer	51
2.3.2	Beam Profile Monitor	52
2.3.3	Phasics SID4 Camera	53
2.3.4	Focal Spot Camera	54
2.3.5	Dosimetry Stack	55
2.4	Conclusion	57
3	Development of Gas Targets and Magnetic Dipoles	59
3.1	Development of Gas Targets	60
3.1.1	Fundamentals of Supersonic Nozzles	60
3.1.2	Computational Fluid Dynamics of Supersonic Nozzles . .	62
3.2	Development of Magnetic Dipoles	65
3.2.1	Magnetic dipole for few-MeV electrons	65
3.2.2	Spectrometer for few-MeV Highly-Divergent Electrons . .	66
3.3	Conclusion	69
4	Production of few-MeV Highly-Charged Beams	71
4.1	Experimental Setup	72
4.2	Experimental Results	75
4.2.1	Laser and Gas Targets Characterization	75
4.2.2	Electron Beam Charge-per-Joule	78
4.2.3	Electron Beam Energy Spectrum and Divergence	81
4.2.4	Electron Beam Dose	85
4.3	Conclusion	87
5	Simulations on few-MeV Highly-Charged Beams	89
5.1	FBPIC-Electric Work Profiler	90
5.2	Numerical Simulations: Idealized Case	91
5.2.1	Simulation Setup	91
5.2.2	Laser Diffraction in High Plasma Densities	93

5.2.3	Acceleration of few-MeV Electron Beams	96
5.2.4	Charge-per-Joule Saturation Effect	105
5.3	Numerical Simulations: Experimental Conditions	107
5.3.1	Simulation Setup	108
5.3.2	Laser Diffraction and Plasma Structures	109
5.3.3	Beam Properties	112
5.4	Conclusion	113
Conclusion and Outlook		115
Appendix A FBPIC Simulation Setup		119
Appendix B List of Figures		121
Appendix C List of Publications and Contributions		131
Bibliography		145

Introduction

Context and Motivation

The interaction between a superintense laser pulse (i.e., $I > 10^{18}$ W/cm²) and a plasma has been of interest to the scientific community for almost fifty years. [Tajima and Dawson \(1979\)](#) were the first to propose generating plasma oscillations in densities $n_e > 10^{18}$ cm⁻³ by exploiting the ponderomotive force of a laser pulse. The formation of a plasma wave in the wake of the laser allows for the creation of accelerating gradients that exceed 100 GV/m, $10^3 - 10^4$ times those of conventional systems. This paves the way for the realization of compact accelerators, offering an economical alternative to current linear accelerators and radiofrequency cavities. Today, for example, it is possible to accelerate an electron beam of a few-picocoulombs to about 1 GeV over a few-centimeter plasma ([Leemans et al., 2006](#), [Oubrie et al., 2022](#)). Considerable efforts have also been made to produce monochromatic and stable electron beams with low emittance and high energy, through recent optimization studies ([Maier et al., 2020](#), [Jalas et al., 2021](#)). These promising advances in laser-plasma accelerators offer revolutionary prospects for high-energy physics research and could potentially transform the field of particle acceleration. Moreover, over the last three decades, laser-plasma accelerators have been studied for the generation of X-rays. This can be achieved through different mechanisms ([Corde et al., 2013a](#)), such as betatron oscillations ([Rousse et al., 2004](#)), Thomson backscattering ([Sprangle et al., 1992](#), [Phuoc et al., 2012](#), [Brümmer et al., 2022](#)), bremsstrahlung radiation ([Edwards et al., 2002](#), [Glinec et al., 2005](#), [Albert and Thomas, 2016](#)) or even using an undulator made of nanowires ([Andriyash et al., 2014](#)). This development has heightened interest in laser-plasma accelerators as potential candidates for compact X-ray sources, capable of resolving features down to a few micrometers. For instance, in Fig. 1(a) and (b), we present laser-plasma-based betatron computed tomographies of a *Chrysopa* ([Svendsen et al., 2018](#)) and of a mouse embryo ([Cole et al., 2018](#)), respectively.

Although these results demonstrate the potential of these devices, the properties of laser-plasma accelerated beams are still far from those of conventional systems.

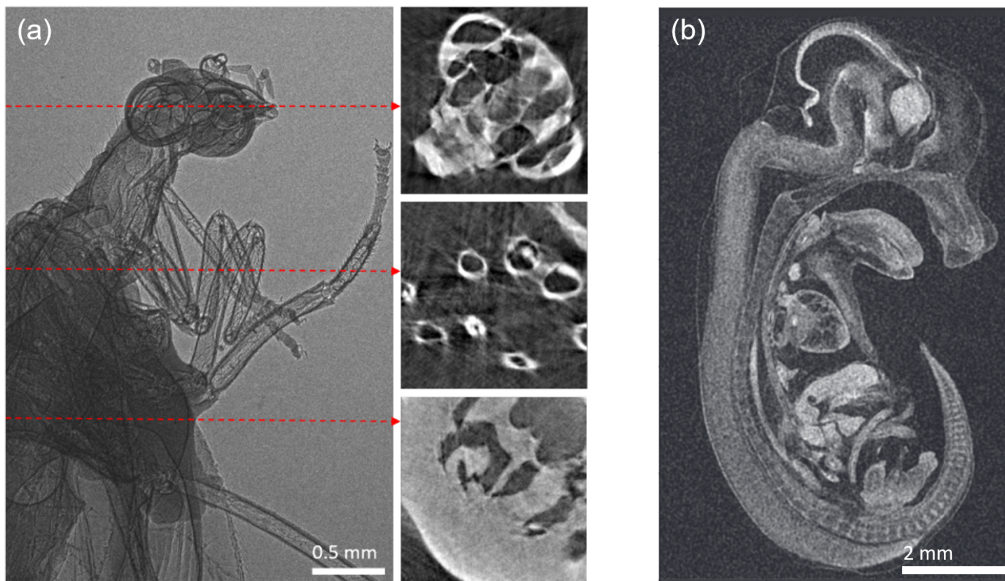


Figure 1: Examples of laser-plasma-based betatron computed tomographies. (a) A Chrysopa. Each inset refers to a tomographic slice along the dashed arrows. *Figure adapted from Svendsen et al. (2018)*. (b) Tomographic slice of a mouse embryo. *Figure adapted from Cole et al. (2018)*.

For example, current medical linear accelerators can produce between 10 to 100 μA , while laser-plasma accelerators only deliver tens nanoamperes (Couperus Cabadağ et al., 2017, Rovige et al., 2020). Despite efforts to improve beam quality and stability, as discussed above, little progress has been made in increasing the electron beam’s average current. Within this context, the main objective of this doctoral thesis was to increase the average current of laser-plasma accelerators aiming at accelerating electrons to just a few MeV. This could be particularly beneficial for low-energy applications that do not require high-quality, monoenergetic electron beams, but rather high-average currents. For instance, the project cited in Multiscan 3D project (2020), funded by the European Union’s Horizon 2020 research and innovation programme, focuses on the development of a novel laser-plasma 3D X-ray tomography machine for border control freight inspection. This device could present advantages over current systems, such as enhanced performance, interoperability, and increased compactness, while reducing inspection time and impact on users. It offers large divergence, good spatial resolution, and requires a very small area for radiation protection. The possibility of transporting the laser and using it for generating X-rays with a peaked spectrum via Compton scattering, as well as for producing neutrons, further enhances its versatility. For clarity, in Fig. 2 we present the conceptual design of the device. The freight passes through a

rectangular frame containing multiple laser-plasma-based bremsstrahlung X-ray sources and detectors, which collects the X-rays and enables 3D tomography of the freight itself. As highlighted by the inset on Fig. 2, each source consists of a small vacuum chamber housing a supersonic nozzle that generates a gas jet (e.g., nitrogen). Upon interaction with the laser pulse, the gas jet becomes a plasma. The laser pulse drives the production of an electron beam, which subsequently interacts with a high-Z target (e.g., tungsten), emitting X-rays via bremsstrahlung. While

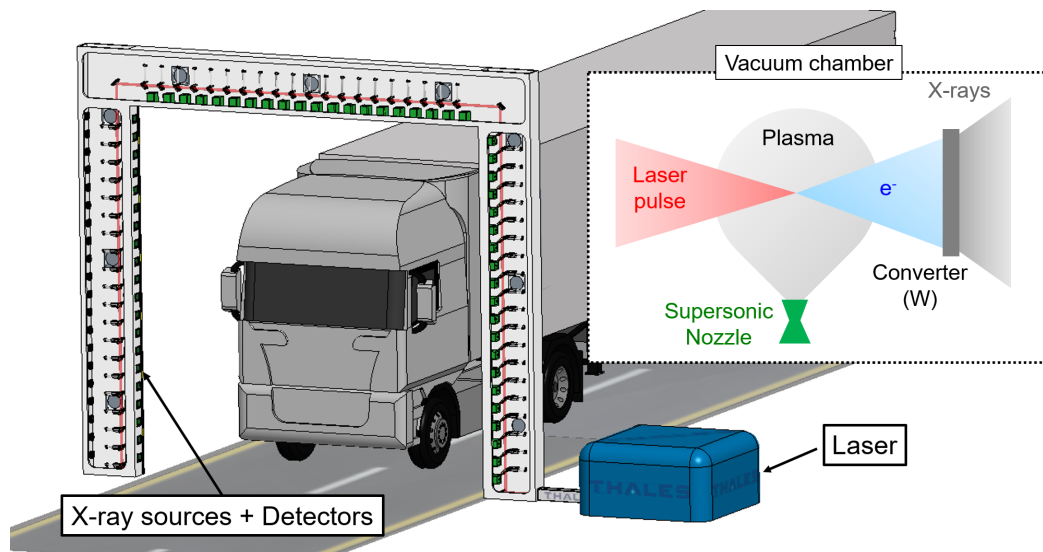


Figure 2: Multiscan 3D project conceptual design. A rectangular frame hosts multiple laser-plasma-based bremsstrahlung sources and the X-ray detector. Each source is reached by a laser pulse, allowing to generate an electron beam. (Inset) Schematic representation of a laser-plasma X-ray source.

current laser-plasma accelerators typically achieve average beam currents around 10 nA, a significant increase by two orders of magnitude is necessary to satisfy the requirements of the Multiscan 3D project. This enhancement will be enabled by further advancements in laser technology (Pellegrina et al., 2022, Kiani et al., 2023), allowing the development of laser systems with average powers exceeding 100 W. However, the primary focus of this thesis is to increase the average beam current in laser-plasma accelerators by improving beam charge. Specifically, our objective is to surpass the charge-per-Joule ratio of 10 nC/J recently achieved by Feng et al. (2023), ultimately allowing us to reach currents of 1 μ A with a laser average power of 100 W.

The activities of this work include an extensive experimental campaign conducted using the 60 TW Salle Jaune laser system at the *Laboratoire d'Optique Appliquée* (LOA), which provides 30 fs pulses. This campaign aimed to investi-

gate and optimize the production of laser-plasma electron beams under various conditions, including different plasma densities, gas targets, laser energies and laser focusing degrees. By systematically varying these parameters, we sought to identify the optimal conditions for maximizing beam charge. Additionally, our research involved detailed Particle-In-Cell simulations to deepen our understanding of the physics underlying the experimental configurations, providing insights into the acceleration mechanisms.

Thesis Outline

The manuscript is organized as follows:

- In Chapter 1, we detail the fundamental concepts of laser-plasma interactions. We cover the prerequisites for plasma wave generation, review electron injection mechanisms, and explore the main acceleration processes. Finally, we discuss key scientific works on generating highly charged electron beams.
- Chapter 2 focuses on the numerical and experimental tools utilized in our research. This chapter introduces the Particle-in-Cell code employed for numerical studies and provides an in-depth overview of the primary diagnostic techniques used during the experimental campaigns discussed in this thesis.
- Chapter 3 details the development of essential components for the experimental campaigns. Specifically, it covers the creation of a supersonic nozzle, which serves as a gas target, and the design and implementation of magnetic dipoles that are crucial for accurately measuring the electron beam energy.
- In Chapter 4, we present the experimental findings of this work. Here, we present the production of few-MeV electron beams, achieving charge-per-Joule values up to 45 nC/J, with laser-to-electron conversion efficiencies reaching approximately 14 %, which are among the highest efficiencies ever recorded.
- In Chapter 5, we present an extensive numerical study designed to uncover the main phenomena occurring under the configurations of interest. Additionally, this chapter provides an analysis of the main acceleration mechanisms, demonstrating that the vast majority of the electron beam is accelerated by the laser ponderomotive force.

Chapter 1

Physics of Laser-Plasma Accelerators

In this chapter, we discuss the principles of laser-plasma acceleration. First, we explore the propagation of electromagnetic waves in plasmas, introducing the notion of Gaussian beams. We conclude the first section of this chapter by discussing the different ionization mechanisms of gases and the laser ponderomotive force. In the second section, we provide the rudiments of laser-plasma acceleration physics, examining the main acceleration regimes, injection mechanisms and limitations of laser-plasma accelerators. We conclude this chapter by briefly discussing the state of the art of highly-charged laser-plasma accelerators.

Contents

1.1	Laser-Plasma Physics Fundamentals	6
1.1.1	Electromagnetic Waves in Plasmas	6
1.1.2	Ionization Mechanisms	11
1.1.3	Ponderomotive Force and Non-Linear Effects	16
1.2	Particle Acceleration in a Plasma Wave	21
1.2.1	Linear Regime	21
1.2.2	Non-Linear Regime and Wave-Breaking	24
1.2.3	Electron Injection and Acceleration	25
1.2.4	Limitations of Laser-Plasma Accelerators	40
1.3	State of the Art	41
1.4	Conclusion	42

1.1 Laser-Plasma Physics Fundamentals

1.1.1 Electromagnetic Waves in Plasmas

Lasers represent a class of devices able to produce electromagnetic waves with unique properties (e.g., spatial and temporal coherency) via *stimulated emission* of atoms or ions, making them a powerful tool for different fields of science. In this section, we will introduce the basic notions of laser physics, following the approach presented by [Svelto \(2010\)](#).

In order to describe the diffraction of a laser pulse through matter, we can first consider Maxwell's equations:

$$\nabla \cdot \mathbf{E} = \frac{\rho}{\epsilon_0} \quad (1.1)$$

$$\nabla \cdot \mathbf{B} = 0 \quad (1.2)$$

$$\nabla \times \mathbf{E} = -\frac{\partial \mathbf{B}}{\partial t} \quad (1.3)$$

$$\nabla \times \mathbf{B} = \mu_0 \left(\mathbf{J} + \epsilon_0 \frac{\partial \mathbf{E}}{\partial t} \right) \quad (1.4)$$

where \mathbf{E} and \mathbf{B} are the electric and magnetic field respectively, while ρ , ϵ_0 , μ_0 and \mathbf{J} are the charge density, the electric permittivity, the magnetic permeability and the electric current density of the medium. Considering the curl of Eq. (1.3), vacuum as the propagation medium (i.e., $\rho, \mathbf{J} = 0$) and from Eq. (1.4), we can yield the wave equation

$$\nabla^2 \mathbf{E} - \frac{1}{c^2} \frac{\partial^2 \mathbf{E}}{\partial t^2} = 0, \quad (1.5)$$

where $c = 1/\sqrt{\mu_0 \epsilon_0}$ is the speed of light in vacuum. Considering a uniformly polarized monochromatic wave under the so-called *scalar approximation* ([Shimoda, 1986](#)), it is possible to describe the electric field propagating in the z -direction with the following scalar quantity

$$E(x, y, z, t) = \tilde{E}(x, y, z) e^{i\omega t}, \quad (1.6)$$

where the term $e^{i\omega t}$ represents a function called *wave carrier*, oscillating at the angular frequency ω . The complex amplitude $\tilde{E}(x, y, z, t)$ must satisfy the wave equation (i.e., Eq. (1.5)) in scalar form. This yields Helmholtz equation

$$(\nabla^2 + k^2) \tilde{E}(x, y, z) = 0, \quad (1.7)$$

with $k = \omega/c = |\mathbf{k}|$ that represents the wavenumber and \mathbf{k} the wavevector. A solution to Eq. (1.7) can be provided using the Huygens-Fresnel principle. Indeed, considering a given point in space $P_0 = (x_0, y_0, z_0)$ where we assume to know $\tilde{E}(x_0, y_0, z_0)$, we can write the following integral solution of Eq. (1.7)

$$\tilde{E}(x, y, z) = \frac{i}{\lambda} \iint_S \tilde{E}(x_0, y_0, z_0) \frac{e^{-ikr}}{r} \cos \theta dx_0 dy_0 \quad (1.8)$$

where λ is the wavelength, r is the distance between the points $P_0(x_0, y_0, z_0)$ and $P(x, y, z)$ and θ is the angle between the z -axis and the segment PP_0 . The double integral is evaluated along the surface S of a given aperture as shown in Fig. 1.1.

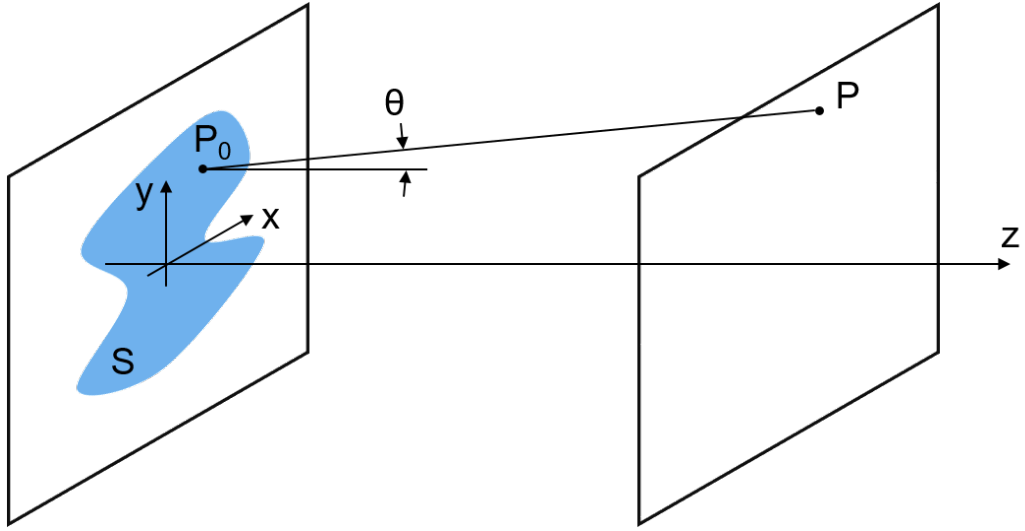


Figure 1.1: Field calculation at the position P , assuming $\tilde{E}(x_0, y_0, z_0)$ to be known. The image has been adapted from Svelto (2010).

Considering small θ angles under the *paraxial approximation* (i.e., $\cos \theta \sim 1$) it is possible to write

$$\tilde{E}(x, y, z) = u(x, y, z) e^{-ikz}, \quad (1.9)$$

where $u(x, y, z)$ is a slowly varying function on the z -direction on a wavelength scale. Thus, Eq. (1.8) becomes

$$u(x, y, z) = \frac{i}{\lambda(z - z_0)} \iint_S u(x_0, y_0, z_0) \times \exp \left(-ik \frac{(x - x_0)^2 + (y - y_0)^2}{2(z - z_0)} \right) dx_0 dy_0, \quad (1.10)$$

assuming the *wavelet* term originating from the elemental area dx_0dy_0 to be

$$u(x_0, y_0, z_0) \frac{e^{-ikr}}{r} dx_0 dy_0 \approx \frac{u(x_0, y_0, z_0)}{(z - z_0)} \times \exp\left(-ik \frac{(x - x_0)^2 + (y - y_0)^2}{2(z - z_0)}\right) dx_0 dy_0. \quad (1.11)$$

Eq. (1.10) represents an integral solution to Eq. (1.7) under the paraxial approximation, allowing to reconstruct the electric field at any given point in space (i.e., $u(x, y, z)$).

Gaussian Beams

Now we can consider a particular set of eigensolutions to Eq. (1.10), called *Gaussian beams* (Kogelnik and Li, 1966). If we perform the surface integral of Eq. (1.10) (i.e., we assume no limiting aperture on the $z = z_0$ plane) we can yield

$$u(x, y, z) \propto \exp\left(-ik \frac{x^2 + y^2}{2q}\right), \quad (1.12)$$

where $q = q(z)$ is called the *complex beam parameter*. At $P_0(x_0, y_0, z_0)$ we can write

$$u(x_0, y_0, z_0) \propto \exp\left(-ik \frac{x_0^2 + y_0^2}{2q_0}\right), \quad (1.13)$$

Since we are considering eigensolutions of Eq. (1.10), the shape of the field (i.e., $u(x, y, z)$) must preserve its functional form as it propagates. Thus, inserting Eq. (1.13) into Eq. (1.10) yields

$$u(x, y, z) \propto \frac{1}{1 + z/q_0} \exp\left(-ik \frac{x^2 + y^2}{2q}\right), \quad (1.14)$$

with $q = q_0 + z$. Hence, Eq. (1.14) represents one possible eigensolution of the diffraction integral (i.e., Eq. (1.10)), often referred as to as the *fundamental mode*, if compared to higher order solutions of Eq. (1.10). For convenience, we write the complex beam parameter as

$$\frac{1}{q} = \frac{1}{R} - i \frac{\lambda}{\pi w^2}. \quad (1.15)$$

It is possible to show (Kogelnik and Li, 1966) that R and w represent the wavefront's radius of curvature and beam radius, usually called *spot-size*. Assuming

$R(z = z_0) \rightarrow \infty$, where for simplicity we consider $z_0 = 0$, we obtain

$$\frac{1}{q_0} = -\frac{i\lambda}{\pi w_0^2}, \quad (1.16)$$

where w_0 is called *beam waist* and it corresponds to beam radius at $1/e$ of the field amplitude (i.e., the smallest transverse dimension of the Gaussian beam). Knowing

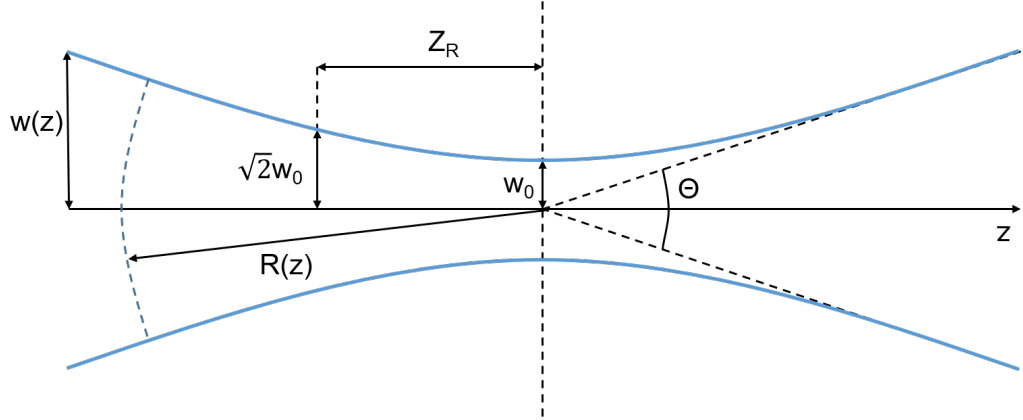


Figure 1.2: Illustration of the characteristic Gaussian beam parameters. *The image has been adapted from Svelto (2010).*

that $q = q_0 + z$ and from Eqs. (1.15) and (1.16) we can write

$$w(z)^2 = w_0^2 \left[1 + \left(\frac{z}{Z_R} \right)^2 \right], \quad (1.17)$$

$$R(z) = z \left[1 + \left(\frac{Z_R}{z} \right)^2 \right], \quad (1.18)$$

with

$$Z_R = \frac{\pi w_0^2}{\lambda}. \quad (1.19)$$

The characteristic length Z_R is called *Rayleigh range* and it corresponds to the distance at which the spot size is $w(\pm) = \sqrt{2}w_0$ and the laser intensity is reduced by a factor two¹. Furthermore, considering $z \gg Z_R$ in Eq. (1.17) it is possible to observe that the spot-size increases linearly. Thus, it is possible to define the

¹Indeed, the laser intensity is inversely proportional to the surface $\pi w^2(z)$.

so-called *beam divergence* as follows

$$\Theta = \frac{2\lambda}{\pi w_0}. \quad (1.20)$$

In Fig. 1.2 it is possible to observe all the characteristic Gaussian beam parameters defined in Eqs. (1.17), (1.18) and (1.19). Combining Eqs. (1.17) and (1.18) with Eqs. (1.14), (1.15) and (1.16) allows us to write the field amplitude of a Gaussian beam:

$$u(x, y, z) = \frac{w_0}{w(z)} \exp\left(-\frac{x^2 + y^2}{w(z)^2}\right) \exp\left[-ik\left(\frac{x^2 + y^2}{2R(z)}\right)\right] \exp(i\phi), \quad (1.21)$$

where $\phi = \arctan(z/Z_R)$ is called the *Gouy phase*.

Introducing a *longitudinal envelope*

$$E_{env} = E_0 \exp\left(-\frac{t}{\tau_e}\right)^2 \quad (1.22)$$

allows us to define a finite time duration of our laser pulse τ_e at $1/e$ of the envelope electric field. Thus, from Eqs. (1.6), (1.9) and (1.21) we can write

$$\begin{aligned} \mathbf{E}(x, y, z) = E_0 \exp\left(-\frac{t}{\tau_e}\right)^2 \frac{w_0}{w(z)} \exp\left(-\frac{x^2 + y^2}{w(z)^2}\right) \\ \exp\left(-ikz - \omega t + k\frac{x^2 + y^2}{2R(z)} - \phi\right) \mathbf{e}_x, \end{aligned} \quad (1.23)$$

with \mathbf{e}_x being the versor indicating the laser polarization direction (i.e., along the x-direction). In this case, the laser is said to be *linearly polarized*. It is also worth mentioning that the proper combination of the two versors \mathbf{e}_x and \mathbf{e}_y allows for the *circular* and *elliptical* polarization. Further information about the subject can be found in [Svelto \(2010\)](#) and in [Siegman \(1986\)](#). In Fig. 1.3 it is possible to observe an example of the field obtained with Eq. (1.23). Finally, for Gaussian beams the peak intensity is ([Siegman, 1986](#)):

$$I_0 = \frac{2U_0}{\sqrt{\pi}\tau_e\pi w_0^2} \approx \frac{2U_0}{\tau_0\pi w_0^2}, \quad (1.24)$$

with U_0 the total energy contained in the Gaussian beam and $\tau_0 = \sqrt{2\ln(2)}\tau_e$. The Ti:Sapphire *Salle Jaune* laser system at LOA allows to reach intensities $I_0 = 6 - 24 \times 10^{19} \text{ W/cm}^2$, assuming $\tau_e \sim 30 \text{ fs}$ and $w_0 = 3 - 6 \mu\text{m}$, for $U_0 = 1 \text{ J}$.

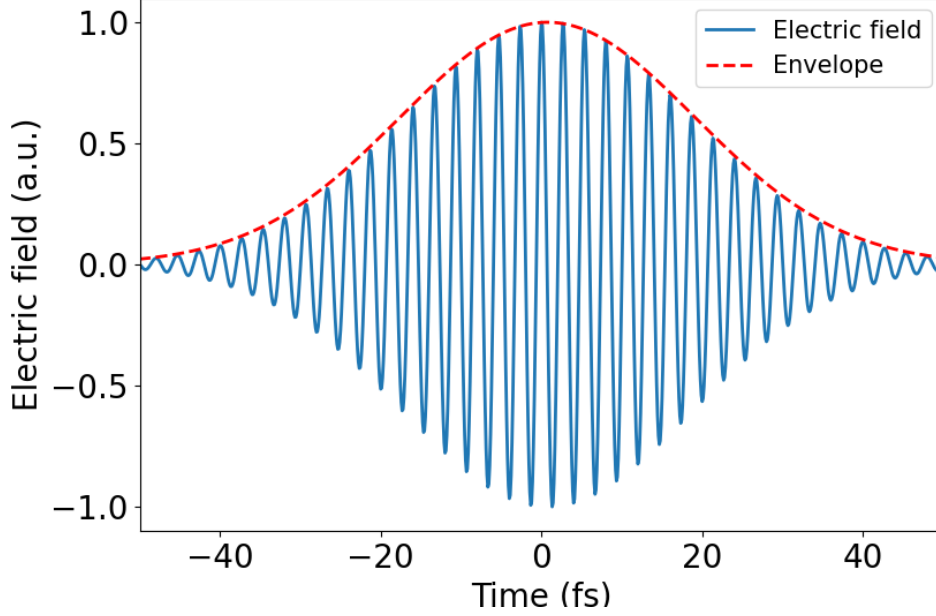


Figure 1.3: Depiction of the electric field E and its envelope E_{env} . Here, we have assumed a time duration $\tau_e \sim 30$ fs and $\lambda = 0.8 \mu\text{m}$.

1.1.2 Ionization Mechanisms

As will be further discussed, all plasmas generated in the experiments presented in this work have been produced via direct ionization with a highly intense laser pulse. Therefore, before discussing the fundamentals of laser pulse propagation in plasma, it is important to briefly review how a superintense laser pulse can ionize a gas to produce plasma. Moreover, in some cases, the ionization in itself might play an important role concerning the electron beam formation mechanism (see Section 1.2.3).

A highly intense laser pulse can fully or partially ionize a gas, creating a plasma. This is possible thanks to the high-power laser electric potential, which is close to the electron binding potential (i.e., Fig. 1.4(a)). In general, it is possible to distinguish two main different ionization regimes: the multi-photon ionization (Mainfray and Manus, 1991) and the tunnel ionization (Landau and Lifshitz, 1969, Bisgaard and Madsen, 2004). In order to distinguish the two different mechanisms, it is possible to make use of the so-called *Keldysh parameter* (Keldysh, 1964, Boroumand et al., 2022):

$$\gamma_K = \frac{\omega\sqrt{2P_{ion}}}{E_{las}}. \quad (1.25)$$

Here P_{ion} is the ionization potential of the considered electron and E_{las} is the laser electric field strength. When $\gamma_K \gg 1$ the ionization is mainly dominated by the multi-photon regime. Instead, for $\gamma_K < 1$ the main ionization process is due to quantum tunneling (Griffiths et al., 2005). As shown in Fig. 1.4(b) when $\gamma_K \gg 1$ the laser field strength is not sufficient to effectively perturb the electron binding potential. Considering, for instance, the first ionization energy of nitrogen (i.e., ~ 14.6 eV) and the energy of one laser photon with a wavelength around $0.8 \mu\text{m}$ (i.e., 1.5 eV), we conclude that one single laser photon cannot ionize a nitrogen atom to N^{+1} . However, as shown in Fig. 1.4(b), *multiple* photons of 1.5 eV each can ionize the nitrogen atom. Instead, for $\gamma_K < 1$, namely for higher E_{las} , the laser can strongly perturb the binding potential, allowing for quantum tunneling to happen, as depicted in Fig. 1.4(c). Finally, Fig. 1.4(d) highlights a third regime, where the laser field strength is intense enough (i.e., $\gamma_K \ll 1$) to suppress the electron binding potential, allowing to directly free the electron. This mechanism is called *barrier suppression ionization* or *over-the-barrier-ionization*.

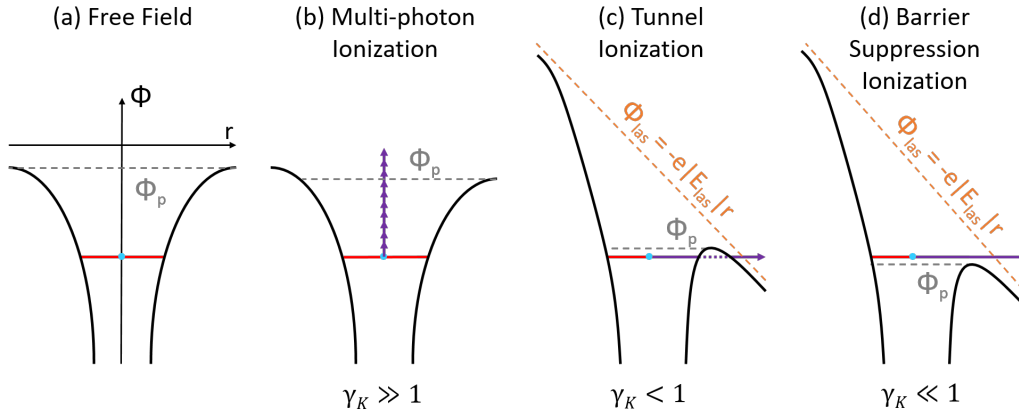


Figure 1.4: Depiction of the atomic Coulomb potential in the presence of a strong-field. Φ_p denotes the actual bonding potential (a) Unperturbed atom potential. (b) Multi-photon ionization. (c) Tunnel ionization. (d) Barrier suppression Ionization. *The image has been adapted from Hansen (2012).*

If we now assume the disturbed potential to be equal to the ionization potential, it is possible to yield (Gibbon, 2005)

$$I_{ion}(\text{W/cm}^2) = 4 \times 10^9 \frac{(P_{ion}(\text{eV}))^4}{Z^2}, \quad (1.26)$$

where Z is the atomic number. Eq. (1.26) represents the threshold laser intensity necessary to trigger the over-the-barrier-ionization. Here, using Eq. (1.26) we also list the intensity threshold necessary to reach different nitrogen ionization states

along with the corresponding ionization potential (Lide, 1995). As we have already mentioned, this is the gas used for all the experiments discussed in the following.

Ionization state	P_{ion} (eV)	I_{ion} (W/cm ²)
N ⁺¹	14.53	3.64×10^{12}
N ⁺²	29.59	6.27×10^{13}
N ⁺³	47.49	4.14×10^{14}
N ⁺⁴	77.47	2.94×10^{15}
N ⁺⁵	97.89	7.49×10^{15}
N ⁺⁶	552.1	7.58×10^{18}
N ⁺⁷	667.1	1.62×10^{19}

Nitrogen has two electronic shells: the outer L- and the inner K-shell. The first contains five electrons, while the second contains two electrons. As we can deduce from the previous table, nitrogen is easily ionized up to N⁺⁵ by a laser that exceeds $\sim 10^{16}$ W/cm². All the lasers used in this work have leading-edge intensities greater than this threshold. Therefore, this allows us to free all L-shell electrons obtaining ten electrons per nitrogen molecule². Instead, the ionization states N⁺⁶ and N⁺⁷ are more difficult to reach since the laser intensity we would need to exceed $\sim 10^{19}$ W/cm². This is usually possible only for a tightly focused pulse and close to the laser peak intensity. For these reasons, we will always consider the nitrogen plasma to be partially ionized.

Propagation in Plasmas

Plasmas represent one of the fundamental states of matter and, despite not being as common in our everyday life as gases, solids and liquids, they are the most abundant form of matter in the universe. More than 99% of the visible universe is made of some form of ionized gas, namely a plasma (Gurnett and Bhattacharjee, 2005). Thanks to their unique properties, they have been the subject of study in different fields of physics and engineering, embodying the core of some cutting-edge research like thermonuclear fusion reactors and particle acceleration.

In view of understanding the interaction between a laser pulse and a plasma, we now introduce a simple model (Pucella and Segre, 2009), in order to introduce some of the most fundamental plasma parameters. Let us consider a 1-D system, where we assume to displace a layer of electrons at $x \rightarrow +\infty$ from the corresponding positive ions. In the region $[0, x_0]$, where we assume to have a positive charge

²Since nitrogen is bi-atomic, if we consider one nitrogen atom to be ionized up to N⁺⁵ a nitrogen molecule would free ten electrons.

density³ n_e , it is possible to yield the electric field using Gauss's law (i.e., Eq. (1.1)):

$$E_x = \frac{n_e e x}{\epsilon_0}, \quad (1.27)$$

with e being the elementary charge. Considering the force exerted by the electric field E_x in the region $[0, x_0]$ on one electron, it is possible to write

$$F_x = -e E_x = m_e \ddot{x}. \quad (1.28)$$

Combining Eqs. (1.27) and (1.28) yields

$$\ddot{x} + \omega_p^2 x = 0, \quad (1.29)$$

where we have defined

$$\omega_p = \sqrt{\frac{e^2 n_e}{m_e \epsilon_0}}, \quad (1.30)$$

with m_e being the electron rest mass. Eq. (1.29) is the equation of a harmonic oscillator, with a characteristic pulsation ω_p , called *plasma frequency*. Hence, it is also possible to define the *plasma wavelength* as $\lambda_p = 2\pi c/\omega_p$, that can also be re-written as

$$\lambda_p(\mu m) \approx \frac{3.34 \times 10^{10}}{\sqrt{n_e(cm^{-3})}}. \quad (1.31)$$

Now we want to study the linear response of a cold, collisionless and uniform plasma while traversed by an electromagnetic wave. Moreover, we neglect any possible external field and we assume that the quantities of interest (e.g., the electric field \mathbf{E}) are created by small perturbations with respect to an initial unperturbed plasma state. There are different possible ways to describe plasmas, for instance via the *kinetic model*, which allows for the most complete description of plasmas. However, in light of the aforementioned hypotheses, we can model our system assuming the *cold fluid approximation* (Pucella and Segre, 2009). Thus, considering the Navier-Stokes equation for this particular case, we can write the following equation for one plasma population (i.e., plasma electrons):

$$m_e \frac{\partial \mathbf{u}}{\partial t} = -e \mathbf{E}, \quad (1.32)$$

where \mathbf{u} is the electron average velocity and $\mathbf{J} = -e n_e \mathbf{u}$. Calculating the Fourier

³Considering an overall neutral system, the positive charge density corresponds to the electron density. From now on we will refer to n_e as the electron density

transform of Eq. (1.32) with respect to t reads

$$\tilde{\mathbf{J}} = \frac{i}{\omega} \frac{e^2 n_e}{m_e} \tilde{\mathbf{E}}, \quad (1.33)$$

where $\tilde{\mathbf{J}}$ and $\tilde{\mathbf{E}}$ are the Fourier transform of \mathbf{J} and \mathbf{E} respectively. We also know that

$$\mathbf{J} = \underline{\underline{\sigma}} \cdot \mathbf{E} \quad (1.34)$$

and

$$\underline{\underline{\epsilon}} = \underline{\underline{I}} + \frac{i}{\epsilon_0 \omega} \underline{\underline{\sigma}}, \quad (1.35)$$

where $\underline{\underline{I}}$, $\underline{\underline{\sigma}}$ and $\underline{\underline{\epsilon}}$ are the identity tensor, the electrical conductivity tensor and the electrical permittivity tensor respectively. Furthermore, considering the plasma as an isotropic medium (i.e., neglecting the space dispersion) from Eqs. (1.33), (1.34) and (1.35) we can write:

$$\epsilon = 1 - \left(\frac{\omega_p}{\omega} \right)^2. \quad (1.36)$$

Furthermore, we can write the following dispersion relation⁴ using Eqs. (1.34), (1.36) and Ampère's law (i.e., Eq. (1.4)):

$$\underline{\underline{\Lambda}} : \mathbf{E} = 0. \quad (1.37)$$

The tensor $\underline{\underline{\Lambda}}$ is defined as

$$\underline{\underline{\Lambda}} = \begin{pmatrix} \frac{k^2 c^2}{\omega^2} - \epsilon & 0 & 0 \\ 0 & \frac{k^2 c^2}{\omega^2} - \epsilon & 0 \\ 0 & 0 & \epsilon \end{pmatrix}. \quad (1.38)$$

Eq. (1.37) represents a linear system. This means that it has a non-trivial solution only if $\det(\underline{\underline{\Lambda}}) = 0$, which allows us to write

$$\epsilon(n^2 - \epsilon)^2 = 0, \quad (1.39)$$

where n is the plasma refractive index. Eq. (1.39) has the following solutions: $\epsilon = 0$ and $n^2 = \epsilon$, which has multiplicity 2. The former gives $\omega = \omega_p$, which describes the dispersion relation of a longitudinal standing wave. The latter, instead, yields $\omega^2 = \omega_p^2 + k^2 c^2$, which is the characteristic dispersion relation of two transverse modes in a cold, collisionless and uniform plasma.

Moreover, we introduce the phase velocity $v_{ph} = c/n$ and the group velocity in

⁴Here we consider $\mathbf{k} = (0, 0, k)$

plasma $v_g = d\omega/dk = cn$, while the refractive index reads

$$n = \sqrt{1 - \frac{\omega_p^2}{\omega^2}} = \sqrt{1 - \frac{n_e}{n_c}}, \quad (1.40)$$

where $n_c(\text{cm}^{-3}) = \omega^2 m_e \epsilon_0 / e^2 \approx 1.1 \times 10^{27} / \lambda^2(\mu\text{m})$ is called the *critical plasma density*. Eq. (1.40) proves that a laser pulse can propagate in a plasma as long as it is *underdense* (i.e., if $n_e < n_c$ or equivalently $\omega > \omega_p$). Instead, a laser pulse cannot propagate in an *overdense* plasma. In this case, indeed, the plasma displays a mirror-like behavior and only a small portion of the laser penetrates in the plasma. However, since the resulting wavevector would be imaginary, the laser pulse amplitude, proportional to $\exp(ikz)$, would be exponentially dumped.

1.1.3 Ponderomotive Force and Non-Linear Effects

Ponderomotive Force

In order to further understand the nature of laser-plasma physics, we now consider the non-relativistic interaction between one electron and a linearly polarized laser pulse, following the approach of [Macchi \(2013\)](#). Thus, the laser electric field will be described by:

$$\mathbf{E}(\mathbf{r}, t) = \mathbf{E}_{env}(\mathbf{r}, t) \cos(\mathbf{k} \cdot \mathbf{r} - \omega t), \quad (1.41)$$

where $\mathbf{E}_{env}(\mathbf{r}, t)$ represents a slowly varying envelope compared to the period $T = 2\pi/\omega$. Furthermore, the spatial variation of the envelope across an oscillation is assumed to be small with respect to the laser wavelength. Hence, from Eq. (1.41) we can write

$$\mathbf{E}(\mathbf{r}, t) \approx \mathbf{E}(\mathbf{r}_c, t) + \underbrace{((\mathbf{r} - \mathbf{r}_c) \cdot \nabla)}_{\delta \mathbf{r}} \mathbf{E}(\mathbf{r}_c, t), \quad (1.42)$$

where \mathbf{r}_c represents the electron initial position. We also assume to describe the electron dynamics as the superposition of a slow motion (\mathbf{r}_s) and a fast oscillating term (\mathbf{r}_o):

$$\mathbf{r}(t) = \mathbf{r}_s(t) + \mathbf{r}_o(t). \quad (1.43)$$

From Eqs. (1.41), (1.42) and (1.43), assuming the electron speed $v_e \ll c$, it is possible to write the following Newton's equation for the zero-order motion

$$\frac{d^2 \mathbf{r}_s}{dt^2} = -\frac{e}{m_e} \mathbf{E}_{env}(\mathbf{r}_c, t) \cos(\mathbf{k} \cdot \mathbf{r}_c - \omega t) \quad (1.44)$$

Eq. (1.44) shows that the slow motion represents an oscillation around the electron initial position \mathbf{r}_c at a velocity

$$\dot{\mathbf{r}}_s = -\mathbf{v}_{e,max} \sin(\mathbf{k} \cdot \mathbf{r}_c - \omega t) = -\frac{e \mathbf{E}_{env}}{m_e \omega^2} \sin(\mathbf{k} \cdot \mathbf{r}_c - \omega t). \quad (1.45)$$

The speed $v_{e,max}$ represents the maximum speed that an electron can achieve thanks to the effect of the laser electric field. Once $v_{e,max}$ reaches values comparable to the speed of light, the relativistic effects must be taken into account and our description is no longer valid. Considering now the $\mathbf{v} \times \mathbf{B}$ term in Newton's equation (i.e., following a perturbative approach) we can write

$$\frac{d^2(\mathbf{r}_o + \mathbf{r}_s)}{dt^2} = -\frac{e}{m_e} \left[\mathbf{E}(\mathbf{r}_c) + (\delta\mathbf{r} \cdot \nabla)\mathbf{E}(\mathbf{r}_c) + \frac{\dot{\mathbf{r}}}{c} \times \mathbf{B} \right]. \quad (1.46)$$

From Eqs. (1.44), (1.46) and averaging over a period T we can obtain

$$m_e \frac{d^2 \langle \mathbf{r}_o \rangle}{dt^2} = -\nabla U_p, \quad (1.47)$$

where the brackets stand for the time average over T and U_p is called *ponderomotive potential* and it is defined as

$$U_p(\mathbf{r}, t) = \frac{e^2}{4m_e \omega^2} E_{env}^2. \quad (1.48)$$

Consequently, the right term of Eq. (1.47) is called *ponderomotive force*:

$$\mathbf{F}_p(\mathbf{r}, t) = -\nabla U_p = -\frac{e^2}{4m_e \omega^2} \nabla E_{env}^2 \quad (1.49)$$

From the definition of ponderomotive force (i.e, Eq. (1.49)) we understand that the electron is pushed towards regions of space of lower laser intensity. Furthermore, since the ponderomotive force is inversely proportional to the electron mass, we notice that for a heavier particle (e.g., a proton) this force would be significantly less effective. A more detailed analysis (Mora and Antonsen, 1997), which accounts for relativistic effects, allows us to write the ponderomotive force as

$$\mathbf{F}_p(\mathbf{r}, t) = -\frac{m_e e^2}{2 \langle \gamma \rangle} \nabla \langle A_{env}^2 \rangle, \quad (1.50)$$

where γ is the Lorentz factor, defined as $\gamma = 1/\sqrt{1 - \beta^2}$ with $\beta = v_e/c$ and \mathbf{A}_{env} is the envelope of the vector potential, frequently used to describe the electromagnetic field. A common way to distinguish between the classic and relativistic

motion of an electron in an electromagnetic field comes through the maximum *normalized vector potential*:

$$a_0 = \frac{e |\mathbf{E}_{env}|}{m_e c \omega} = \frac{e |\mathbf{A}_{env}|}{m_e c} \approx 0.85 \sqrt{I_0 (\times 10^{18} \text{W} \cdot \text{cm}^{-2})} \lambda (\mu\text{m}). \quad (1.51)$$

When $a_0 < 1$ ($a_0 > 1$) the electron has a classical (relativistic) behavior. As previously mentioned, the Salle Jaune laser system at LOA can deliver pulses with intensities exceeding 10^{19}W/cm^2 , hence allowing the electrons to reach the relativistic regime.

For completeness, we wish to conclude this section by mentioning that in a laser field described by the vector potential $\mathbf{A}(\mathbf{r}, t)$ the electron transverse momentum is $\mathbf{p}_\perp \approx \mathbf{A}(e/c)$ (Macchi, 2013). This relation holds true for non-plane wave configurations where the intensity does not vary significantly over the wavelength λ . Assuming $\mathbf{p} \approx \mathbf{p}_\perp$, it is now possible to estimate the maximum kinetic energy gained by an electron via the ponderomotive force:

$$m_e (\gamma - 1) c^2 \approx m_e c^2 \left(\sqrt{1 + a_0^2} - 1 \right), \quad (1.52)$$

Self-Focusing

While considering the propagation of a laser pulse in plasma, it is now necessary to treat some fundamental non-linear effects that high-intensity lasers experience, such as the so-called *self-focusing*. This phenomenon allows the laser to remain focused (or guided) for distances that can exceed the Rayleigh length. In order to properly understand this effect, we first consider the plasma refractive index. Assuming, for simplicity, the weakly relativistic regime (i.e., $a_0^2 \ll 1$) it is possible to write (Esarey et al., 1996, Mori, 1997)

$$\begin{aligned} n(r, z) &= \sqrt{1 - \frac{\omega_p^2 \tilde{n}_e(r, z)}{\omega^2 \gamma n_e}} \\ &\approx 1 - \frac{1}{2} \left(\frac{\omega_p}{\omega} \right)^2 \left(1 - \frac{a_0^2(r, z)}{2} + \frac{\delta n_e(r, z)}{n_e} \right), \end{aligned} \quad (1.53)$$

where $\tilde{n}_e(r, z)$ and $\delta n_e(r, z) = \tilde{n}_e(r, z) - n_e$ are the local plasma density and the density variation due to the ponderomotive force. In Eq. (1.53) it is possible to distinguish two different contributions to self-focusing. The term $1 - a_0^2/2$ is related to what is called *relativistic self-focusing*, while $\delta n_e(r, z)/n_e$ is purely linked to the *ponderomotive self-focusing*. Both contributions allow for the refractive index

to be higher on-axis (i.e., $\delta n/\delta r < 0$), yielding a focusing effect on the laser. Consequently, the self-focusing produces an increase in the laser intensity, which in turn causes an increment of both the ponderomotive and relativistic terms, enhancing the self-focusing itself. Furthermore, the relativistic term has been proven to become predominant to the ponderomotive one (Hafizi et al., 2000). However, in order for the laser to reach the relativistic self-focusing, it needs to exceed a certain power threshold (Esarey et al., 2009) called *critical power* and defined as

$$P_c(GW) \approx 17 \left(\frac{\omega}{\omega_p} \right)^2. \quad (1.54)$$

For a laser power $P \lesssim P_c$ the laser diffracts and for $P \gtrsim P_c$ the pulse is self-focused. The presence of higher-order non-linearities usually prevents the laser to be indefinitely focused (Sprangle et al., 1987, Hafizi et al., 2000). Furthermore, it is possible to write the following equation describing the evolution of the spot-size and taking into account the self-focusing (Esarey et al., 2009) assuming once again $a_0^2 \ll 1$

$$\frac{w^2(z)}{w_0^2} = 1 + \left(1 - \frac{P}{P_c} \right) \left(\frac{z}{Z_R} \right)^2. \quad (1.55)$$

From Eq. (1.55) it is possible to deduce that self-focusing can counteract the laser natural diffraction, allowing the pulse to be *relativistically guided* (or self-guided) for distances larger than Z_R . In Fig. 1.5 we show an example of a relativistically guided pulse (blue curve) compared to the vacuum laser diffraction (green curve). The former has been obtained thanks to a Particle-In-Cell simulation (see Section 2.1.2) using the code FBPIC, while the latter has been plotted using Eq. (1.17). Here, we notice that the laser spot-size experiences an oscillation around $w_0 = 3 \mu\text{m}$ along a distance $L_{sf} \approx 10 \times Z_R = 300 \mu\text{m}$. This represents an important result for laser-plasma accelerators, since guiding allows for a laser pulse to propagate for long distances preserving a high intensity. Lastly, it is worth mentioning that in the experiments presented in this thesis, we consider densities $\gtrsim 10^{19} \text{ cm}^{-3}$. This yields a critical power $P_c \lesssim 2 \text{ TW}$, which is easily reached with the laser systems discussed in this thesis, thus making self-focusing of relevance for this work.

Self-Modulation

Another crucial phenomenon a laser pulse can experience while propagating in a plasma is *self-modulation*. This non-linear effect is often associated with a particular acceleration regime called *self-modulated laser wakefield acceleration* (Krall et al., 1993). Here, we just intend to outline the main features related to the

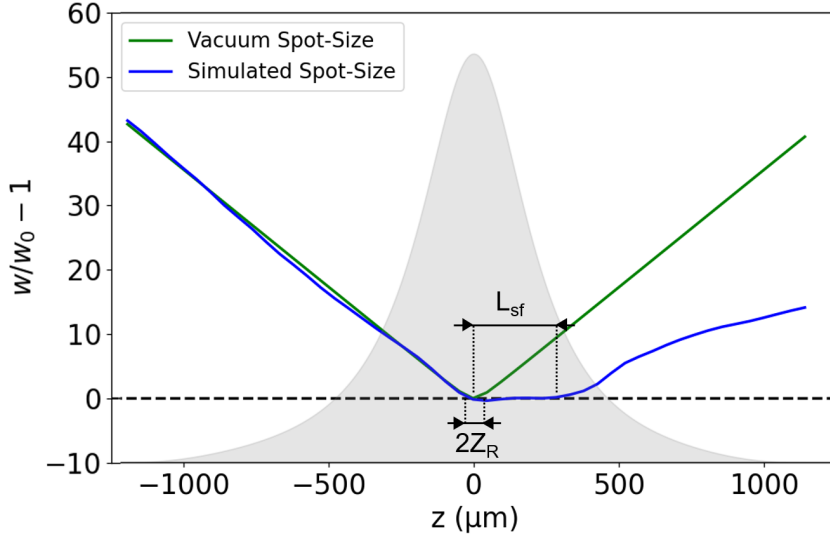


Figure 1.5: Numerical example of relativistic self-focusing obtained using the code FBPIC (Lehe et al., 2016). The blue and green curves represent the laser spot-size propagating in plasma and in vacuum respectively. The gray-shaded area is the normalized plasma density profile. For visual purposes, we plot $w/w_0 - 1$, and the horizontal dotted line represents the condition $w = w_0$. The laser is initially defined in vacuum at $z \approx -1200 \mu\text{m}$ and it is focused at $z = 0$, where $n_e = 3.6 \times 10^{19} \text{ cm}^{-3}$. The laser parameters are $\tau_0 = 30 \text{ fs}$, $\lambda = 0.8 \mu\text{m}$ and $a_0 = 3.8$.

self-modulation of a laser pulse, without addressing the acceleration mechanism.

With reference to the previous section about self-focusing, a laser pulse with $P > P_c$ can be relativistically guided for distances longer than Z_R . However, considering now a long laser pulse (i.e., $L = c\tau_0 > \lambda_p$), different instabilities (e.g., stimulated Raman scattering) can affect its propagation. One major phenomenon that can play such a role is the envelope self-modulation. As we will describe in Section 1.2.1, a laser pulse can excite a plasma wave thanks to its ponderomotive force. This in turn, can produce periodic focusing and defocusing regions in the plasma (Esarey et al., 1990), severely modulating the envelope of a long laser pulse at the plasma wavelength λ_p (Esarey et al., 1996). It is possible to assume the laser-induced plasma modulation as

$$\delta n_e(r, \zeta) = \delta n_{e,0}(r) \cos(k_p \zeta) \quad (1.56)$$

in the limit $L \gg \lambda_p$. Here, $\delta n_{e,0}$ is the ponderomotive-induced radial plasma

density profile and $\zeta = z - v_g t$. Hence, the refractive index defined by Eq. (1.53) is modified, resulting in an axially periodic density channel, where $\partial n_e / \partial r > 0$ ($\partial n_e / \partial r < 0$) the laser envelope focuses (defocuses). This results in a laser envelope to be modulated at λ_p and it could lead to the formation of a train of *beamlets* of length $\approx \lambda_p / 2$, which can remain self-guided for several Z_R . Similarly to what we have concluded about self-focusing, also self-modulation is of relevance to this work. Indeed, if we consider a 30 fs-laser pulse, it is easy to show that $L = c\tau_0 \approx 10 \mu\text{m}$ and $\lambda_p < 10 \mu\text{m}$ for $n_e > 10^{19} \text{cm}^{-3}$. Hence, in this thesis, we easily satisfy both conditions for self-modulation, namely $L > \lambda_p$ and $P > P_c$.

1.2 Particle Acceleration in a Plasma Wave

1.2.1 Linear Regime

As we have briefly mentioned, a high-intensity laser pulse propagating in an underdense plasma can excite waves in its wake. Here, we show this result using the cold-fluid description of plasmas (Pucella and Segre, 2009). The continuity and Navier-Stokes equations for a collisionless non-relativistic (i.e., $a_0 \ll 1$) plasma are

$$\frac{\partial n_e}{\partial t} + \nabla \cdot (n_e \mathbf{v}_e) = 0 \quad (1.57)$$

$$\frac{\partial \mathbf{v}_e}{\partial t} + (\mathbf{v}_e \cdot \nabla) \mathbf{v}_e = -\frac{e}{m_e} (\mathbf{E} + \mathbf{v}_e \times \mathbf{B}). \quad (1.58)$$

Here \mathbf{v}_e is the electron average velocity (\mathbf{u} in Eq. (1.32)). We will introduce the following ansatz:

$$\mathbf{E} = \mathbf{E}_{las} - \nabla \Phi \quad (1.59)$$

$$\mathbf{E}_{las} = -\frac{\partial \mathbf{A}}{\partial t}, \quad (1.60)$$

where \mathbf{E}_{las} is the electric field of a linearly-polarized laser and $\nabla \Phi$ is assumed to be the plasma wave electric field. Averaging Eq. (1.58) over a laser period and linearizing yields

$$\frac{\partial \langle \mathbf{v}_e \rangle}{\partial t} = \frac{e}{m_e} \nabla \Phi - \frac{c^2}{2} \nabla \langle a^2 \rangle, \quad (1.61)$$

where it is possible to recognize the ponderomotive force contribution (i.e., $-\nabla \langle a_0^2 \rangle$). Considering now Poisson's equation under the Coulomb gauge we can write

$$\nabla^2 \Phi = \frac{e(n_e - n_0)}{\epsilon_0} = \frac{en_0}{\epsilon_0} \left(\frac{\delta n}{n_0} \right) \quad (1.62)$$

Here, n_0 is the unperturbed electron density and we also assume $n_e = n_0 + \delta n$. Thus, Eq. (1.57) becomes

$$\frac{\partial \delta n}{\partial t} + n_0 \nabla \cdot \langle \mathbf{v}_e \rangle = 0 \quad (1.63)$$

after linearizing and considering a small density perturbation (i.e., $\delta n \ll n_0$). From Eq. (1.61), (1.62) and (1.63) we can obtain

$$\left(\frac{\partial^2}{\partial t^2} + \omega_p^2 \right) \frac{\delta n}{n_0} = \frac{c^2}{2} \nabla^2 \langle a^2 \rangle. \quad (1.64)$$

This is the expression of a forced harmonic oscillator with an angular frequency ω_p . As expected, on the right-hand side of Eq. (1.64) we see that the oscillation is possible thanks to the ponderomotive force. We also notice that when the laser envelope and the oscillator described in Eq. (1.64) are resonant the excitation will be the most intense.

Considering now Eq. (1.62) and introducing the change of variables $(z, t) \rightarrow (\zeta = z - v_g t, \tau)$, Eq. (1.64) becomes

$$\left(\frac{\partial^2}{\partial \tau^2} + v_g^2 \frac{\partial^2}{\partial \zeta^2} - 2v_g \frac{\partial^2}{\partial \tau \partial \zeta} + \omega_p^2 \right) \phi = \frac{\omega_p^2}{2} \langle a^2 \rangle, \quad (1.65)$$

where we have defined the normalized scalar potential $\phi = e\Phi/(m_e c^2)$. Under the quasi-static approximation (Gorbunov and Kirsanov, 1987), where we assume that the laser envelope does not significantly evolve on the time scale necessary to transit a plasma electron (i.e., $\partial/\partial t \ll v_g \partial/\partial \zeta$), we can write

$$\left(\frac{\partial^2}{\partial \zeta^2} + k_p^2 \right) \phi = \frac{k_p^2}{2} \langle a^2 \rangle, \quad (1.66)$$

and the normalized scalar potential becomes

$$\phi(r, \zeta) = -\frac{k_p}{4} \int_{\zeta}^{+\infty} a^2(r, \zeta') \sin(k_p(\zeta - \zeta')) d\zeta'. \quad (1.67)$$

Assuming a laser beam with both a transverse and longitudinal exponential profile, as defined in Eq. (1.23), we can write

$$\phi(r, \zeta) = -\sqrt{\pi} a_0^2 \frac{k_p l_0}{4} e^{-k_p^2 l_0^2 / 4} e^{-2r^2/w_0^2} \sin(k_p \zeta), \quad (1.68)$$

where $r = \sqrt{x^2 + y^2}$ is the radial coordinate. Hence, the radial (E_r) and longitudi-

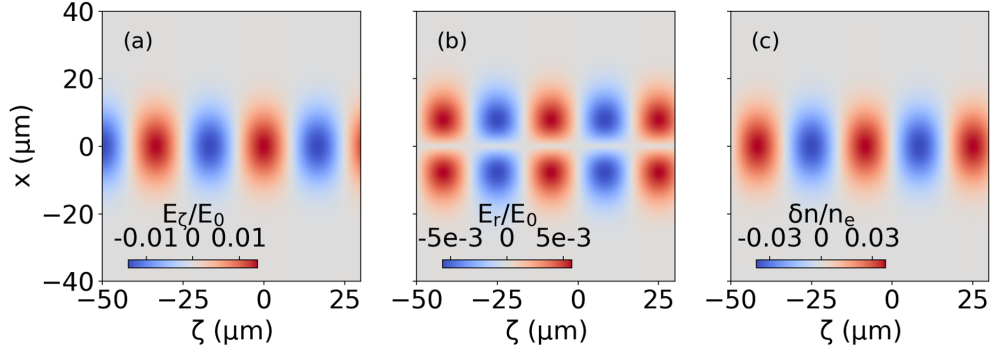


Figure 1.6: Linear regime quantities: (a) Normalized longitudinal wakefield E_z/E_0 , (b) normalized radial wakefield E_r/E_0 and (c) normalized plasma density oscillation $\delta n/n_0$.

nal (E_z) components of the electric field are

$$E_r(r, \zeta) = -\frac{\partial \phi}{\partial r} = -E_0 \sqrt{\pi} a_0^2 \frac{r l_0}{w_0^2} e^{-k_p^2 l_0^2/4} e^{-2r^2/w_0^2} \sin(k_p \zeta) \quad (1.69)$$

$$E_z(r, \zeta) = -\frac{\partial \phi}{\partial \zeta} = E_0 \sqrt{\pi} a_0^2 \frac{k_p l_0}{4} e^{-k_p^2 l_0^2/4} e^{-2r^2/w_0^2} \cos(k_p \zeta), \quad (1.70)$$

with $E_0 = m_e c \omega_p / e$, which in practical units is (Dawson, 1959)

$$E_0 (\text{GV.m}^{-1}) \approx 96 \sqrt{n_e (\times 10^{18} \text{cm}^{-3})}. \quad (1.71)$$

On the other hand, the plasma density perturbation reads

$$\begin{aligned} \frac{\delta n}{n_0} &= -\frac{1}{k_p^2} \frac{\partial^2 \phi}{\partial \zeta^2} \\ &= \frac{E_0}{k_p} \sqrt{\pi} a_0^2 \frac{l_0}{4} e^{-k_p^2 l_0^2/4} e^{-2r^2/w_0^2} \sin(k_p \zeta) \left[1 + \frac{8}{k_p^2 w_0^2} \left(1 - \frac{2r^2}{w_0^2} \right) \right]. \end{aligned} \quad (1.72)$$

In Fig. 1.6 we can see three plots showing the normalized electric field (i.e., E_z/E_0 , E_r/E_0) and the plasma oscillation $\delta n/n_0$ obtained using Eqs. (1.69), (1.70) and (1.72). Here, we have considered a 30-fs Gaussian pulse with $\lambda = 0.8 \mu\text{m}$, a beam waist $w_0 \approx 15.7 \mu\text{m}$ and $a_0 = 0.2$, propagating in a plasma with $n_0 = 10^{18} \text{cm}^{-3}$. The blue regions (red regions) in Fig. 1.6(a) are accelerating (decelerating) for an electron beam. Similarly, the blue regions (red regions) in Fig. 1.6(b) represent focusing (defocusing) areas for an electron beam.

1.2.2 Non-Linear Regime and Wave-Breaking

When $a_0 > 1$ the linear description of a plasma wave is no longer valid, and we enter what is called a *non-linear regime*. In this case, it is possible to show that Eqs. (1.57) and (1.57) read (Kruer, 2019, Gibbon, 2005)

$$\frac{\partial \delta n}{\partial t} + n_0 \frac{c}{\gamma} \nabla \cdot \mathbf{u}_e = 0 \quad (1.73)$$

$$\frac{1}{c} \frac{\partial \mathbf{u}_e}{\partial t} = \frac{1}{c} \frac{\partial \mathbf{a}}{\partial t} + \frac{1}{c} \nabla \phi - \frac{1}{\gamma} \mathbf{u}_e \times \nabla \times \mathbf{a}, \quad (1.74)$$

where $\mathbf{u}_e = \gamma \mathbf{v}_e / c$ is the normalized electron velocity and $\mathbf{a} = e\mathbf{A} / (m_e c)$ is the normalized vector potential. Here, we also define the relativistic gamma as $\gamma = \sqrt{1 + a^2 + u_{e,z}^2}$. Under the quasi-static approximation, from Eqs. (1.62), (1.73) and (1.74) it is possible to yield (Osterhoff, 2009)

$$\frac{\partial^2 \phi}{\partial \zeta^2} = \frac{k_p^2}{2} \left(\frac{1 + a^2}{(1 + \phi)^2} - 1 \right). \quad (1.75)$$

Here, we notice that for small values of ϕ and for $a_0 \ll 1$ we find Eq. (1.66). To better understand the difference between the linear and non-linear regime, in Fig. 1.7 we plot the wakefield quantities for $a_0 \approx 2$ obtained through an FBPIC simulation. Here, we notice that the plasma wave is no longer sinusoidal and that the normalized longitudinal wakefield E_z / E_0 displays a sawtooth-like profile. Furthermore, between each plasma density oscillation, the wakefield is almost linear. If we consider to inject⁵ an electron at the rear of one plasma wave (e.g., at $\zeta \approx -35 \mu\text{m}$ in Fig. 1.7), it can experience the accelerating field over significant distances and reach relativistic energies. However, once injected and accelerated to a velocity exceeding the wakefield phase velocity v_p , this particle can reach a region where the electric field is decelerating (e.g., at $\zeta \approx -28 \mu\text{m}$ in Fig. 1.7), experiencing a *dephasing* (Esarey et al., 2009, Katsouleas, 1986) with respect to the wakefield.

Under these conditions (i.e., when $a_0 > 1$), the laser can excite plasma waves with large amplitudes, causing the the steepening of the density profile (i.e., $\delta n / n_0 - 1$) we see in Fig. 1.7. Moreover, the plasma electrons can reach velocities that exceed v_p , experiencing a process called *longitudinal wavebreaking*. Making use of Akhiezer-Polovin equations (Akhiezer and Polovin, 1956), it is possible to estimate the maximum electric field amplitude before wavebreaking for a cold-relativistic plasma: $E_{wb} = \sqrt{2} E_0 (\gamma_p - 1)^{1/2}$, where $\gamma_p^2 = 1 / (1 - (v_p / c)^2)$.

⁵The so-called *injection conditions* that allow for an electron to be trapped in a plasma period will be discussed in the following.

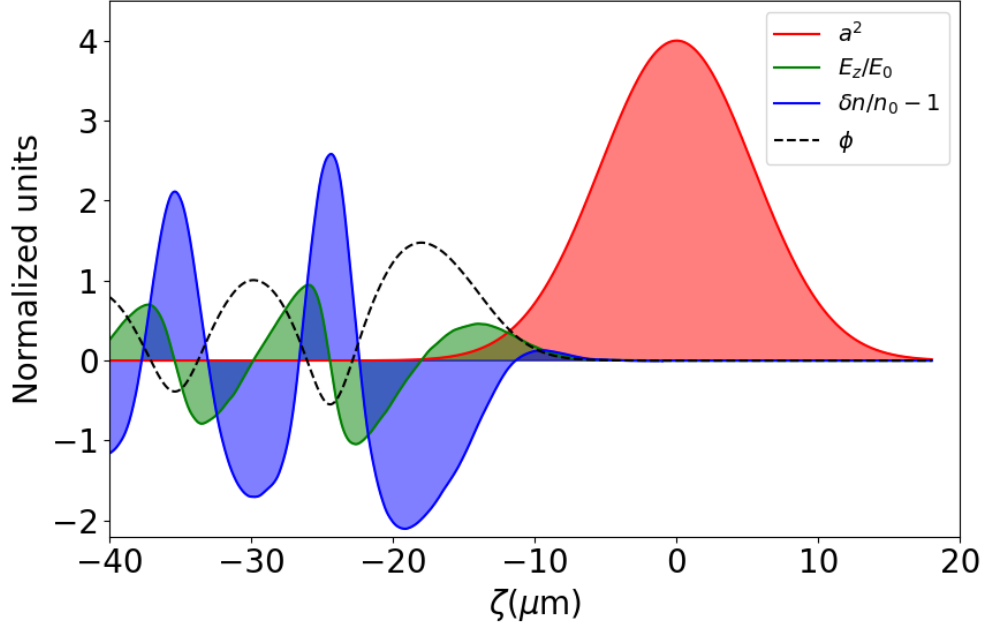


Figure 1.7: FBPIC non-linear wakefield quantities obtained with a 30-fs laser for $a_0 \approx 2$ and with a plasma density $n_0 = 1.2 \times 10^{19} \text{ cm}^{-3}$. Here, a is the normalized laser amplitude, ϕ and E_z/E_0 are the normalized wakefield potential and electric field. We plot the normalized plasma density as $\delta n/n_0 - 1$ for visual purposes.

A more detailed analysis that considers a warm plasma description can be found in [Schroeder et al. \(2005\)](#), while a warm-relativistic study is presented in [Katsouleas and Mori \(1988\)](#).

1.2.3 Electron Injection and Acceleration

We now discuss the conditions that allow plasma electrons to be injected in a plasma period and subsequently be accelerated. With reference to the quantities of the previous section (i.e., the example of Fig. 1.7), we introduce a 1D description of the so-called *self-injection*, under the quasi-static approximation. A more detailed 3D description can be found in [Kostyukov et al. \(2004\)](#). Hence, we can write the following Hamiltonian for an electron in a wakefield ([Faure, 2016](#), [Esirkepov et al., 2006](#))

$$H = \sqrt{1 + u_{\perp}^2 + u_z^2} - \phi(\zeta) - \beta_p u_z, \quad (1.76)$$

where $\beta_p = v_p/c$, v_p represents the plasma wave velocity and $u_{\perp,z} = p_{\perp,z}/(m_e c)$ is the normalized electron momenta. Here, z is the electron longitudinal coordinate in the wakefield frame. Introducing the normalized canonical momentum $\mathbf{U} = \mathbf{u} - \mathbf{a}$, we can write

$$H = \sqrt{1 + (U_{\perp} + a)^2 + U_z^2} - \phi(\zeta) - \beta_p u_z, \quad (1.77)$$

with $U_{\perp} = u_{\perp} - a$ and $U_z = u_z$. From Hamilton's equations it is possible to show that the transverse canonical momentum is conserved (i.e., it is a constant of motion):

$$\frac{\partial U_{\perp}}{\partial t} = -\frac{\partial H}{\partial r} = 0 \Rightarrow u_{\perp}(\zeta) - a(\zeta) = \text{const.} \quad (1.78)$$

From Eq. (1.77) it is also possible to find a second constant of motion. Since this Hamiltonian does not explicitly depend on time, but only on ζ , the energy of the system is conserved. Hence, considering an electron with initial energy H_0 it is possible to yield

$$u_z = \beta_p \gamma_p^2 (H_0 + \phi) \pm \gamma_p \sqrt{\gamma_p^2 (H_0 + \phi)^2 - \gamma_{\perp}^2}, \quad (1.79)$$

with $\gamma_{\perp}^2 = 1 + u_{\perp}^2$. Using Eq. (1.79) we are able to plot different trajectories in phase space for different initial conditions, as shown in Fig. 1.8. For instance, considering electrons at rest in front of the laser pulse (i.e., $\zeta_i = +\infty$) with $u_z(\zeta_i) = u_{\perp}(\zeta_i) = 0$, we yield $H_0 = 1$. Furthermore, from Eq. (1.78) we find $u_{\perp}(\zeta) = a(\zeta)$. Hence, Eq. (1.79) becomes

$$u_{fluid} = \beta_p \gamma_p^2 (1 + \phi) \pm \gamma_p \sqrt{\gamma_p^2 (1 + \phi)^2 - (1 + a^2(\zeta))}, \quad (1.80)$$

which represents the trajectories of plasma background electrons (black lines in Fig. 1.8). These electrons are not injected and oscillate in the plasma wakefield. The red line of Fig. 1.8, instead, represents the separatrix, namely the trajectory that allows to distinguish between trapped and untrapped electrons. In order to yield this trajectory, we first consider an electron moving with a velocity $v_z = v_p$ (i.e., $u_z(\zeta_{min}) = \beta_p \gamma_p$) and located at a minimum of the potential (ϕ_{min}). The conservation of canonical momentum allows us to write $u_{\perp}(\zeta_{min}) = a(\zeta_{min})$, hence the Hamiltonian's separatrix reads

$$H_{sep} = \frac{\sqrt{1 + a^2(\zeta_{min})}}{\gamma_p} - \phi_{min}. \quad (1.81)$$

The blue trajectories in Fig. 1.8 refer to the injected electrons. In this case, it is possible to show that for these particles the necessary and sufficient condition for trapping is $H_i \leq H_{sep}$, where H_i is the injected electron's Hamiltonian. Con-

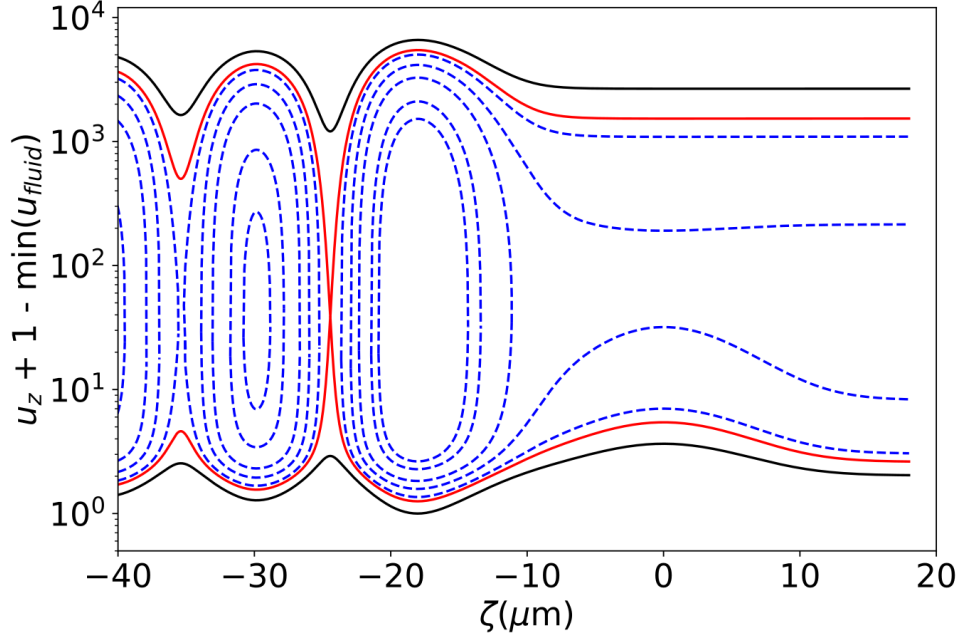


Figure 1.8: Trajectories in phase space obtained using Eq. (1.79) and the numerical example of Fig. 1.7. The black line represents the orbit of non-injected electrons, the red one the separatrix and the blue dashed lines the trapped orbits.

Considering a trapped electron behind the laser pulse at position ζ_i and moving at $v_z(\zeta_i) = v_p$ the electric field potential is $\phi(\zeta_i) = \phi_i \geq \phi_{min}$. Moreover, from Eq. (1.76) we can obtain

$$H_i = (1 + \beta_p^2 \gamma_p^2)^{1/2} - \phi_i - \beta_p^2 \gamma_p = \frac{1}{\gamma_p} - \phi_i. \quad (1.82)$$

This allows us to conclude that for an injected electron $H_i \leq H_{sep}$ since $\phi_i \geq \phi_{min}$.

Once we have introduced the fundamental trajectories, it is possible to define the trapping threshold in a plasma wave. Hence, we consider an electron in front of the laser pulse. This particle will be injected if $u_z(+\infty) > u_z^{sep}(+\infty)$, which means that the electron's initial momentum needs to exceed the initial separatrix momentum $u_z^{sep}(+\infty)$. According to Eq. (1.79) the initial separatrix momentum reads

$$u_z^{sep}(+\infty) = \beta_p \gamma_p^2 H_{sep} - \gamma_p \sqrt{\gamma_p^2 H_{sep}^2 - 1}, \quad (1.83)$$

and consequently an electron with an energy $E > E_{trap}$ will be injected and

accelerated in the wakefield, where

$$E_{trap} = m_e c^2 \left(\sqrt{1 + (u_z^{sep}(+\infty))^2} - 1 \right). \quad (1.84)$$

From Eq. (1.84) it is clear that the trapping is easier for high-amplitude plasma waves and/or for small values of γ_p (i.e., small plasma phase velocities). Furthermore, as $\phi_{min} \rightarrow -1$, E_{trap} tends to zero: this is the start of wave-breaking. Indeed, in this case the plasma wave becomes so steep that all electrons initially at rest are injected. As $\phi_{min} = -1$ the longitudinal wakefield reaches the cold wave-breaking limit (i.e., $E_{wb} = \sqrt{2}E_0(\gamma_p - 1)^{1/2}$), where we recall that $E_0 = m_e c \omega_p / e$.

Bubble Regime and Transverse Self-Injection As we have previously discussed, when a highly-intense laser (i.e., $a_0 > 1$) propagates through an underdense plasma it generates steep plasma waves and the resulting wakefield can easily exceed intensities up to ~ 100 GV/m. If an electron finds itself trapped in one accelerating region of the laser pulse, it can quickly gain energy, reaching relativistic velocities. Under appropriate conditions (i.e., $k_p w_0 \approx 2\sqrt{a_0}$ and $c\tau_0 \approx 0.26\lambda_p$ (Lu et al., 2007)) a superintense laser is *resonant* with the plasma period. In this case, the ponderomotive force is able to almost completely expel the electrons from the region just behind the laser pulse, generating a self-guiding ion cavity or a *bubble* (Pukhov and Meyer-ter Vehn, 2002, Lu et al., 2006, 2007, Xie et al., 2007). This structure is generated thanks to the particular trajectories followed by the electrons: once they have been expelled by the laser ponderomotive force, they cross their paths behind the laser due to the positive ions restoring force, creating an enclosed cavity. In Fig.1.9(a) it is possible to observe an FBPIC simulation of the bubble (or blowout) regime, while in Fig.1.9(b) we show a schematic view of the ion cavity of Fig.1.9(a). Here, we can see that this cavity is surrounded by an electron sheath of radius $r_b \approx 2\sqrt{a_0}/k_p$ (Lu et al., 2007) and also the corresponding longitudinal electric field E_z . Similarly to our previous discussion, if we consider an electron bunch trapped inside this structure as shown in Fig.1.9(b) (i.e., in the accelerating phase of E_z) it can be efficiently accelerated. As soon as the electrons overcome the center of the bubble, they find themselves in the decelerating phase of the wakefield. Therefore, considering a perfectly spherical bubble in cylindrical coordinates (r, θ, ζ) under the quasi-static approximation we can write the following expressions for the electric field and the relative forces (Lu et al., 2006, Xie et al., 2007)

$$\phi = -\frac{k_p^2}{8}(\zeta^2 + r^2) \quad (1.85)$$

$$E_r = E_0 \frac{k_p}{4} r \quad \text{and} \quad \mathbf{F}_r = -\frac{m_e \omega_p^2}{2} r \mathbf{e}_r \quad (1.86)$$

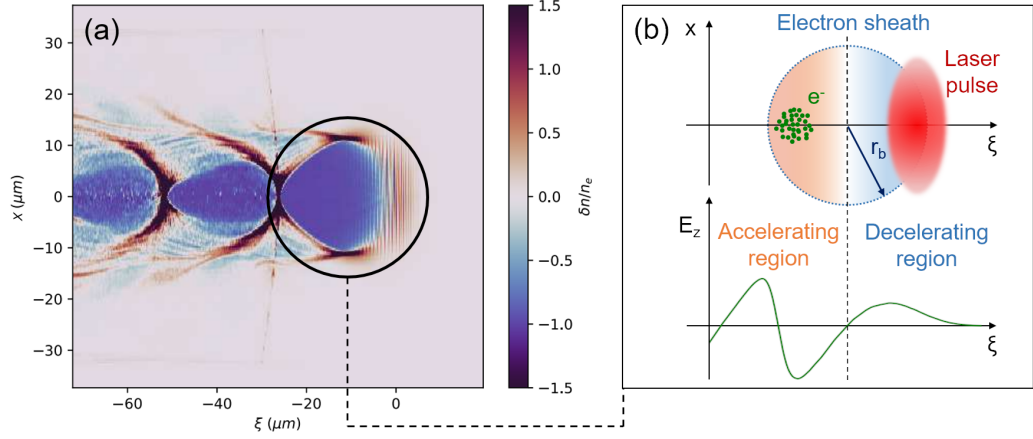


Figure 1.9: (a) FBPIC simulation of the bubble regime. The laser pulse is propagating from left to right. Here, the color map represents the normalized plasma density variation $\delta n/n_e$ and $\xi = z - v_g t$. *Figure from Oubrierie (2022)*. (b) Schematic representation of the electron sheath and trapped electrons (green dots) on the top of the image and the longitudinal electric field E_z on the bottom.

$$E_z = E_0 \frac{k_p}{2} \zeta \quad \text{and} \quad \mathbf{F}_z = -\frac{m_e \omega_p^2}{2} \zeta \mathbf{e}_z. \quad (1.87)$$

From Eq. (1.86) we can notice that the transverse force is independent of ζ , linearly dependent on r and always focusing. This means that the trapped electron bunch is always confined during the whole acceleration process. Lastly, considering Eqs. (1.87), (1.71) and $\zeta = 4\sqrt{a_0}/k_p$ (i.e., the bubble diameter), we can obtain an expression to estimate the peak longitudinal electric field for this regime

$$E_z (\text{GV.m}^{-1}) \approx 96 \sqrt{a_0 n_e (10^{18} \text{cm}^{-3})}. \quad (1.88)$$

By exploiting the notions we have introduced concerning the injection conditions and under the bubble regime, we can now examine one specific kind of self-injection called *transverse self-injection*. In Section 1.2.3 we have shown that in order to trap an electron in a plasma period it must have a sufficiently high energy. Analogously, we can say that one electron can be injected if its velocity exceeds the plasma phase velocity. If we now consider an electron at the rear of a bubble (i.e., on a plasma density peak) with a velocity higher than the bubble velocity, we can say that it satisfies the basic condition for self-injection. Hence, in order for this electron to be trapped, the plasma wave must experience what we have called wavebreaking. With reference to Fig. 1.8, this phenomenon happens when the separatrix and the fluid orbit overlap (Katsouleas and Mori, 1988, Bulanov et al., 1997). To better understand this injection mechanism, we recall that the electrons

in front of the laser pulse are radially expelled thanks to the ponderomotive force. Subsequently, these particles cross their trajectories as shown in Fig. 1.9(a) behind the laser pulse, due to the action of the ion restoring force. This in turn allows for the generation of the bubble-like structure. Therefore, if an electron finds itself behind the ion cavity and the plasma wave experiences wavebreaking, the electron can be trapped inside the bubble. This trapping mechanism is called *transverse self-injection* (Modena et al., 1995, Gordon et al., 1998). Fig.1.10 provides more insights concerning the kind of trajectories an electron needs to follow for it to be injected: the trapping condition depends on the electron's initial transverse position (Kostyukov et al., 2010). Namely, we notice that if an electron finds itself in front of the laser pulse at $|x| \gtrsim r_b$, it is not able to acquire enough energy to be injected and it simply slides to the side of the bubble. On the other hand, if $|x| \lesssim r_b$ the electron usually does not gain enough energy to be injected and it coasts the cavity sheath. Finally, for $|x| \approx r_b$ the electron is able to slide along the electron sheath and reach the rear of the bubble, feeling the wakefield pulling it toward the center of the cavity. Here, the particle can be injected due to wavebreaking and be accelerated. However, following this kind of trajectory is often not enough for

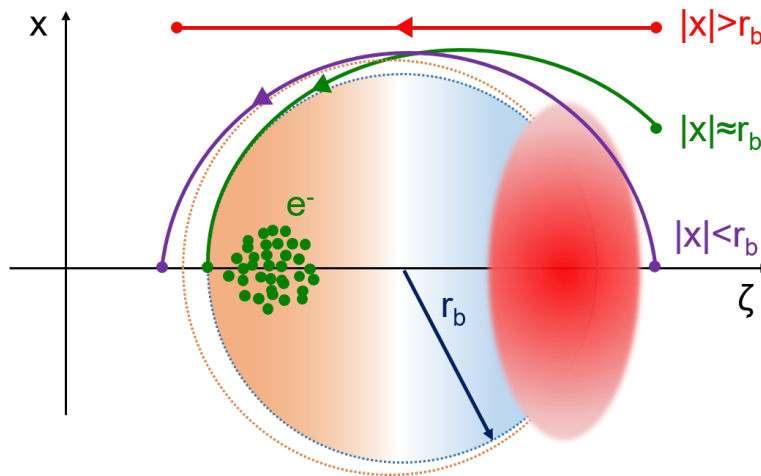


Figure 1.10: Schematics of the transverse injection for different electron transverse positions. For $|x| \gtrsim r_b$ and $|x| \lesssim r_b$ it is not possible for the electrons to be injected. For $|x| \approx r_b$ the electrons can be injected because of wavebreaking. The rapid expansion of the cavity (orange circle) facilitates the whole injection process.

electrons to be injected. Indeed, they typically do not exceed the plasma phase velocity: they momentarily enter the bubble without being actually injected. One way to facilitate the wavebreaking, and thus the transverse self-injection, is via a sudden expansion of the ion cavity (Kalmykov et al., 2009, Kostyukov et al., 2010), as shown in Fig. 1.10. Indeed, such an increase in the bubble size translates into a

deceleration of the plasma wave: an electron finding itself at the rear of the cavity can now be more easily trapped. On the other hand, the electrons that are already inside the cavity remain a longer time in the accelerating phase of the wakefield and reach velocities that allow them to be effectively injected and accelerated. This sort of expansion is possible thanks to the strong self-focusing of the laser (Malka et al., 2002). Since the bubble diameter is around $4\sqrt{a_0}/k_p$ (Lu et al., 2007), a rise of a_0 translates into an increase of the cavity dimension. This injection technique suffers from a lack of stability and usually allows to produce electron beams with large energy spreads, owing to the injection that can occur during the entire propagation of the laser. However, examples of quasi-monoenergetic beams can be found in Mangles et al. (2004), Faure et al. (2004), Geddes et al. (2004).

Longitudinal Self-Injection While examining the possible electron trajectories in the previous section, we concluded that for $|x| < r_b$ the ponderomotive force pushes the electrons too far from the electron sheath. This, in turn, prevents the electrons from being injected. However, if the laser is not tightly focused, namely presenting a Full-Width at Half Maximum diameter $d \approx 20 \mu\text{m}$ (with $a_0 \approx 1.4$) even the electrons at $|x| < r_b$ can be injected, as shown in Fig. 1.11(a). Here, the electron traverses the laser pulse and, after gaining some energy in the cavity, it is injected. This trapping technique is called *longitudinal self-injection* (Corde et al., 2013b) and it allows to produce few-pC stable electron beams with low divergence and high energy dispersion. This kind of injection is usually more complicated to realize compared to the transverse counterpart. This is due to the fact that a longitudinally injected electron experiences a decelerating force before being trapped at the rear of the bubble. Furthermore, the longitudinal injection typically occurs at the beginning of the propagation (*first injection*) when the laser focuses, a_0 increases and the bubble expands. Lastly, longitudinal self-injection can be followed by transverse self-injection, as shown in Fig. 1.11(b).

Ionization Injection Another injection technique of relevance for this work is the so-called *ionization injection* (Chen et al., 2012, Pak et al., 2010, McGuffey et al., 2010). As we have treated in Section 1.1.2, a high-Z gas like nitrogen is not always completely ionized after being traversed by a laser pulse. Indeed, while the L-shell electrons are easily freed by the laser leading edge, the K-shell electrons are freed at much higher intensities (i.e., close to the laser intensity peak). The two possible mechanisms that can describe the inner shell ionization are tunnel and barrier suppression ionization. In order to properly describe these two mechanisms⁶, we

⁶The barrier suppression ionization mechanism, indeed, can be considered as a special case of tunnel ionization.

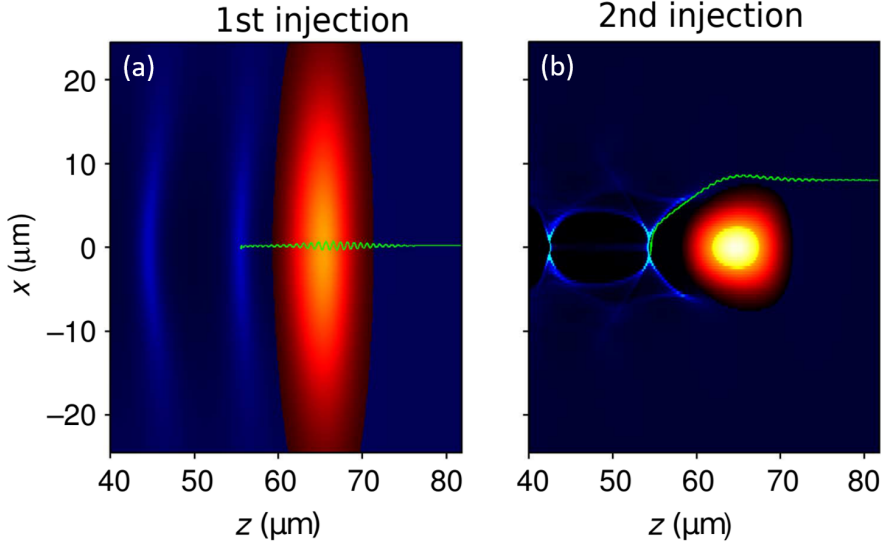


Figure 1.11: PIC simulation displaying the (a) longitudinal and (b) transverse self-injection mechanism. The red and blue colormaps relate to the laser intensity and plasma density. The green lines represent the electron trajectories. *Figure from Corde et al. (2013b).*

can make use of the Ammosov-Delone-Krainov (ADK) model (Ammosov et al., 1986). According to (Bauer and Mulser, 1999) this model is in agreement with the numerical solutions of Schrödinger equation if the laser electric field is smaller than the critical electric field

$$E_c(\text{GV.m}^{-1}) = 514(\sqrt{2} - 1) \left| \frac{P_{ion}}{27.2} \right|^{3/2}, \quad (1.89)$$

where P_{ion} is the unperturbed ionization potential energy of the electron in consideration, as in Eq. (1.25). For laser electric fields exceeding this critical value, the main ionization mechanism is the barrier suppression one. It is possible to estimate the maximum laser electric field as $E_{max} = m_e c \omega a_0 / e \approx 2.0 \times 10^4 \text{ GV.m}^{-1}$, considering $a_0 \approx 5$ that can be reached with the Salle Jaune laser system. From Eq. (1.89) we get $E_c = 2.6 \times 10^4 \text{ GV.m}^{-1}$ considering the 7th nitrogen electron (i.e., $P_{ion} = 667.1 \text{ eV}$). Since $E_{max} \lesssim E_c$, in the presence of self-focusing the normalized vector potential could exceed the maximum value $a_0 \approx 5$ and cause the laser electric field to surpass the critical value E_c . This, in turn, would favor barrier suppression over tunnel ionization.

The ADK model allows to write the ionization probability rate as (Chen et al.,

2013):

$$W = \omega_a \left(\frac{3n^{*3}E}{\pi Z^3 E_a} \right)^{1/2} \frac{Z^2}{2n^{*2}} \left(\frac{2e}{n^*} \right) \exp \left[-\frac{2E_a}{3E} \left(\frac{Z}{n^{*3}} \right) \right] \times \quad (1.90)$$

$$\times \frac{(2l+1)(l+|m|)!}{2\pi n^{*2}|m|!(l-|m|)!} \left(\frac{2E_a Z^3}{En^{*3}} \right)^{2n^*-|m|-1},$$

where $\omega_a \approx 4.13 \times 10^{16} \text{ s}^{-1}$ is the atomic unit frequency, Z the atomic number, l and m the the electron's orbital and magnetic quantum number, $n^* = Z\sqrt{P_{ion}/P_H}$ is the effective principal quantum number, with $P_H = 13.6 \text{ eV}$ being the hydrogen ionization potential. Finally, we define $E_a = \alpha^4 m_e c^2 / (r_e e)$, where α and r_e are the fine-structure constant and the classical electron radius respectively.

Thanks to this model, it is possible to study the ionization of one nitrogen atom, considering a Gaussian laser pulse with $\lambda = 0.8 \mu\text{m}$, $\tau_0 = 30 \text{ fs}$ and $I_0 = 10^{19} \text{ W.cm}^{-2}$ (i.e., $a_0 \approx 2.2$). In Fig. 1.12 we show the ionization rates of one nitrogen atom obtained in these conditions. Here, we notice that the first five levels of ionization occur at low laser intensity (i.e., $\sim 10^{16} - 10^{17} \text{ W.cm}^{-2}$), while the last two require higher intensities (i.e., $> 10^{18} \text{ W.cm}^{-2}$). The outer shell electrons

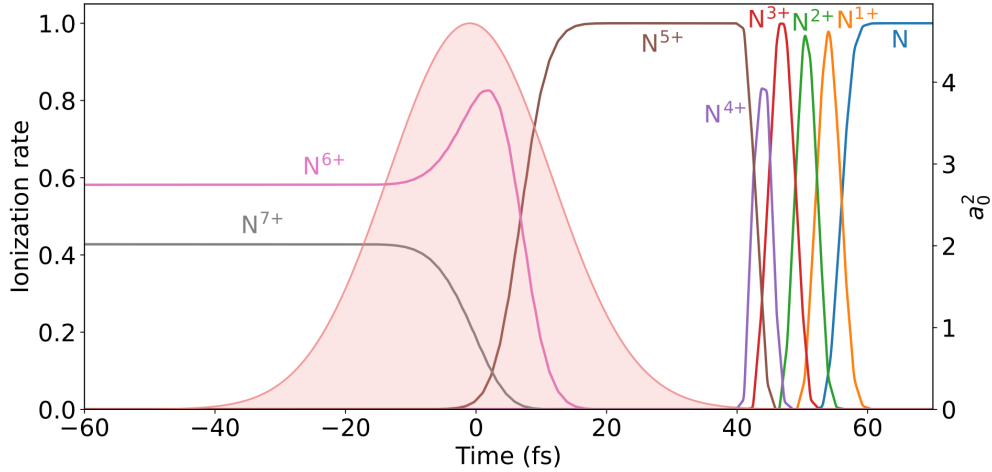


Figure 1.12: Nitrogen ionization rate (colored curves) for a laser (red area) with $a_0 \approx 2.2$ that propagates toward the right.

are strongly pushed by means of the ponderomotive force (Eq. (1.49)), creating the surrounding plasma (Fig. 1.13). On the other hand, some inner shell electrons can be ionized close to the optical axis and they are not subjected to strong electric field gradients. Thus, these particles can be longitudinally injected (Pak et al., 2010,

McGuffey et al., 2010, Pollock et al., 2011), following the trajectories shown in Fig. 1.13. Ionization injection is a stable and reliable technique that also allows

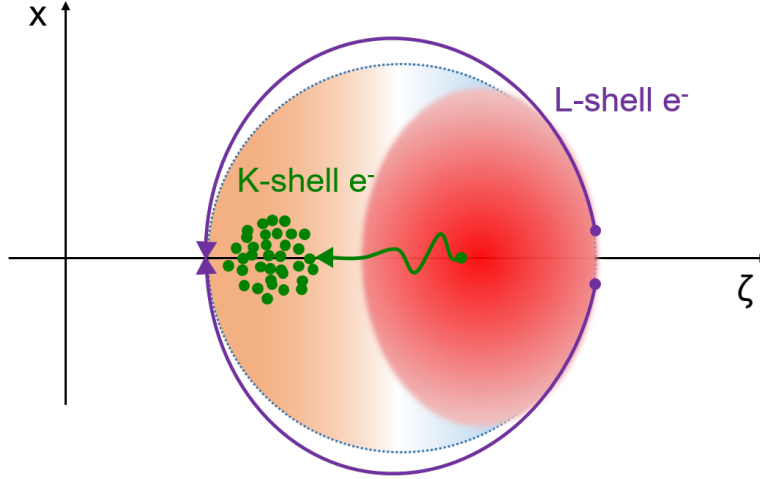


Figure 1.13: Schematic representation of the ionization injection mechanism for electrons born in front of the laser pulse (purple curves) and in the middle (green curve).

to reach charges of the order of the nanocoulomb (Guillaume et al., 2015, Doepp et al., 2016) and recently exceeding ten nanocoulombs (Feng et al., 2023). Similar to what we mentioned regarding transverse injection, this technique generally leads to the production of large energy spreads due to continuous trapping that can occur throughout the entire laser propagation in plasma.

Density Transition Injection As we have previously discussed, the lower the plasma wave phase velocity, the easier the electrons can be injected. One possible way to control the plasma wave phase velocity is via engineering the plasma density. Indeed, by introducing a downward density ramp it is possible to decrease the phase velocity and trigger the injection (Bulanov et al., 1998, Suk et al., 2001, Brantov et al., 2008). In order to describe this process, we consider a gentle density gradient (i.e., $\frac{1}{n_0} \frac{\partial n_e}{\partial z} \ll k_p$) and $a_0 \ll 1$. Hence, under these hypotheses and the quasistatic approximation the plasma wave equation reads

$$\left(\frac{\partial^2}{\partial \zeta^2} + k_p^2 \right) \phi = \frac{k_p^2}{2} \langle a^2 \rangle, \quad (1.91)$$

which is the equation we previously introduced to describe the linear regime, i.e., Eq. (1.66). Assuming a laser pulse with the transverse and longitudinal profile

defined in Eq. (1.23), we were able to solve Eq. (1.66) and find Eq. (1.68):

$$\phi(r, \zeta) = -\sqrt{\pi} a_0^2 \frac{k_p l_0}{4} e^{-k_p^2 l_0^2 / 4} e^{-2r^2 / w_0^2} \sin(k_p \zeta). \quad (1.92)$$

Dropping the dependency on r for simplicity (i.e., $r = 0$), Eq. (1.92) becomes

$$\phi(\zeta) = -\sqrt{\pi} a_0^2 \frac{k_p l_0}{4} e^{-k_p^2 l_0^2 / 4} \sin \varphi(\zeta), \quad (1.93)$$

where we have defined the wakefield phase as $\varphi = k_p \zeta = k_p(z - v_g t)$. Hence, we can yield the oscillation frequency and wavevector as follows:

$$\omega(z) = -\partial \varphi / \partial t = k_p v_g = \omega_p(z), \quad (1.94)$$

$$k(z, t) = \partial \varphi / \partial z = k_p + \partial k_p / \partial z (z - v_g t) \quad (1.95)$$

and the phase velocity $v_p(z, t) = \omega_p(z) / k(z, t)$ reads

$$v_p(z, t) = \frac{v_g}{1 + (z - v_g t) \frac{1}{k_p} \frac{\partial k_p}{\partial z}}. \quad (1.96)$$

Thus, from Eq. (1.95) we conclude that behind the laser pulse (i.e., $z - v_g t < 0$) and in a downward density gradient (i.e., $\partial k_p / \partial z < 0$) the wavevector increases. This, in turn, causes the plasma wave phase velocity to decrease, allowing for the electrons to be injected. The density transition injection has been proven to be an efficient method for trapping electrons, allowing to produce stable beams with $\sim 10\%$ energy spreads (Geddes et al., 2008, Schmid et al., 2010a). Some research groups managed to generate beams at a few-hundreds keV (Geddes et al., 2008, He et al., 2013), while other experiments successfully controlled the injection via a shock in the gas flow (Schmid et al., 2010a, Buck et al., 2013) or through a laser-induced perturbation (Faure et al., 2010), resulting in a tunable beam energy (Buck et al., 2013, Brijesh et al., 2012).

Direct Laser Acceleration Thus far, we have highlighted the central role of the wakefield in the energy gain of the electrons. Under proper conditions, however, it is possible to observe that the laser can participate in the acceleration process, via a mechanism called *Direct Laser Acceleration* (DLA). To present a simple yet comprehensive overview of this process, we rely on the description provided by Arefiev et al. (2016). Other notable works on DLA include those by Pukhov et al. (1999) and Shaw et al. (2014, 2016).

When considering a laser pulse with a characteristic length $L = c\tau_0 \gg \lambda_p$

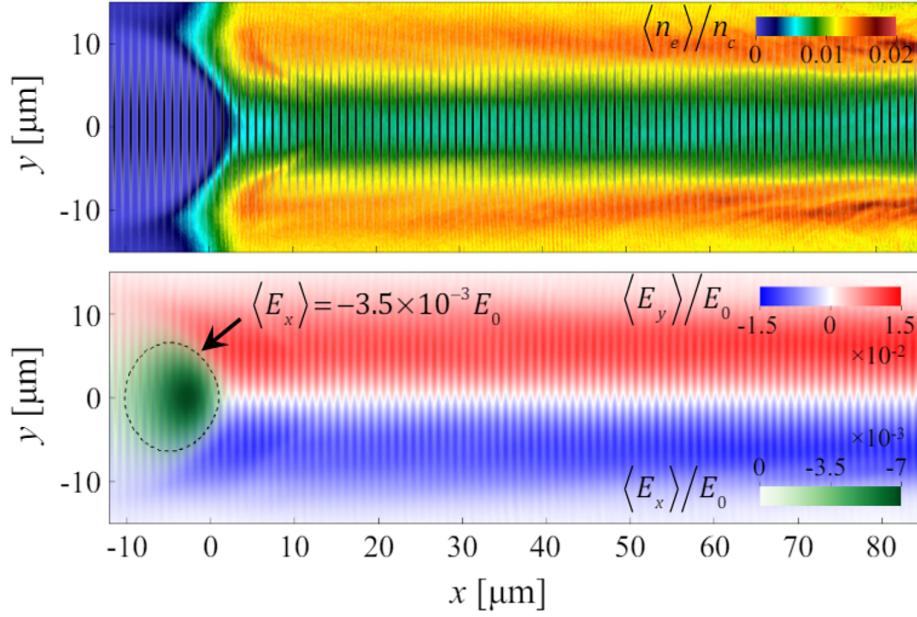


Figure 1.14: 2D EPOCH (Arber et al., 2015) simulation. Here the laser pulse with $a_0 = 8.5$ interacts with a plasma density plateau at $n_e = 10^{19} \text{ cm}^{-3}$ and it fills the whole window. (top) Normalized plasma density profile $\langle n_e \rangle / n_c$. The modulations in the plasma density are related to the laser period. (bottom) Normalized longitudinal and transverse electric fields $\langle E_x \rangle$ and $\langle E_y \rangle$. The quantities have been averaged over ten laser periods. *Figure from Arefiev et al. (2016).*

interacting with a plasma, we observe the formation of a steady-state channel, as depicted in Fig. 1.14. The figure shows a 2D Particle-In-Cell simulation of a relatively long laser pulse (i.e., $\tau_0 \gtrsim 100 \text{ fs}$) with $a_0 = 8.5$ propagating in a constant plasma density plateau at $n_e = 10^{19} \text{ cm}^{-3}$. Specifically, the laser is polarized along the y -direction and propagates toward positive x . The top panel of Fig. 1.14 illustrates the normalized plasma density profile averaged over ten plasma periods (i.e., $\langle n_e \rangle / n_c$). Hence, we notice that as the pulse enters the plasma, its ponderomotive force expels some of the electrons in the transverse direction producing a channel. The ion charge present in the structure generates a counterbalancing force that prevents the channel from being completely emptied of electrons. Moreover, electrons are continuously injected through the opening of the channel (i.e., at $x \approx 0$) thanks to the presence of a quasi-static longitudinal field. In the bottom panel of Fig. 1.14 we can see the averaged longitudinal and transverse fields, $\langle E_x \rangle$ and $\langle E_y \rangle$ respectively. Before discussing the dynamics of the electrons inside the channel, we briefly present the dynamics of one electron in vacuum interacting with a plane wave whose amplitude gradually increases from

zero to a_0 . Specifically, we assume the particle to be initially at rest. Hence, the electron's dynamics is governed by the following equations

$$\frac{d\mathbf{p}}{dt} = -e \mathbf{E} - \frac{e}{\gamma m_e c} (\mathbf{p} \times \mathbf{B}), \quad (1.97)$$

$$\frac{d\mathbf{r}}{dt} = \frac{c}{\gamma m_e c} \mathbf{p}, \quad (1.98)$$

where \mathbf{r} and \mathbf{p} are the particle position and momentum respectively, while $\gamma = \sqrt{1 + p^2/m_e^2 c^2}$ is its relativistic factor. Here, \mathbf{E} and \mathbf{B} are the electric and magnetic fields of that wave and we can write

$$\mathbf{E} = -\frac{m_e c}{e} \frac{\partial \mathbf{a}}{\partial t}, \quad (1.99)$$

$$\mathbf{B} = \frac{m_e c^2}{e} \nabla \times \mathbf{a}, \quad (1.100)$$

where we recall that \mathbf{a} is the normalized vector potential. Furthermore, we assume the laser electric field to be linearly polarized along the y -axis, hence we can write $a = a_0 F(\xi) \sin(\xi)$, where

$$\xi = \frac{2\pi}{\lambda}(x - ct) \quad (1.101)$$

is a normalized phase and $F(\xi)$ is a slowly varying function from zero to unity. Finally, we can write the following analytical solutions of Eqs. (1.97) and (1.98)

$$p_x/m_e c = a^2/2, \quad (1.102)$$

$$p_y/m_e c = a. \quad (1.103)$$

As mentioned in Section 1.1.3, when $a_0 \geq 1$ the electron exhibits a relativistic behavior. Specifically, the momentum oscillations induced by the laser become relativistic and Lorentz force convective term (i.e., $e \mathbf{p} \times \mathbf{B}$) becomes important, leading to a longitudinal motion. Indeed, from Eqs. (1.102) and (1.103) we notice that for $a_0 \gg 1$ we have $p_x \gg p_y$. Under these assumptions, the electron can achieve a maximum γ -factor

$$\gamma_{vac} = 1 + a_0^2/2, \quad (1.104)$$

Fig. 1.15 displays an electron trajectory interacting with a plane wave, with the colormap indicating the laser amplitude. In this representation, the electron, denoted by a red dot, is observed to slip behind the laser, moving towards the left side of the image. Specifically, at $\xi = -12$, the electron's transverse velocity and the laser electric field exhibit opposite phases, leading to electron acceleration. As

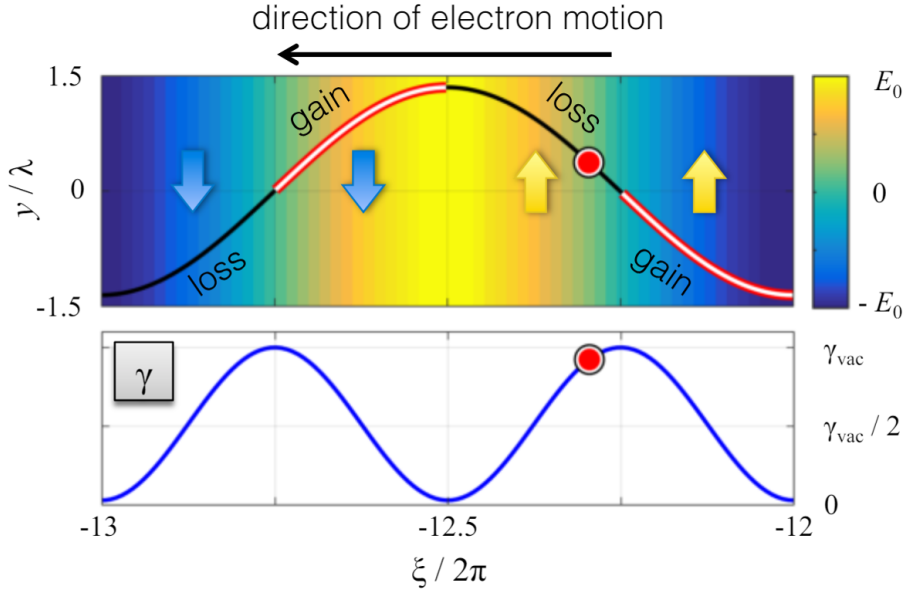


Figure 1.15: (top) Electron trajectory and (bottom) γ as functions of ξ . Here, $a_0 = 8.5$. The colormap refers to the laser amplitude, while the arrows indicate the electron transverse velocity direction. *Figure from Arefiev et al. (2016).*

the electron continues to slip, it enters a region where the electric field is positive (i.e., $\xi = -12.25$). Here, due to the electron's positive transverse momentum, it begins to decelerate until reaching $\xi = -12.5$, where it starts to gain energy again. Consequently, it is inferred that the electron gains and loses energy twice during each laser cycle, resulting in no net energy gain. This behavior is shown in the bottom panel of Fig. 1.15, which presents the variation of the Lorentz factor (γ) with respect to ξ . Therefore, it is straightforward to deduce that one possible way to ensure energy gain comes from decreasing the dephasing between the electron and the wave, allowing the particle velocity to remain anti-parallel to the laser electric field. Alternatively, it is also possible to show that a change in the oscillations of the transverse velocity can also induce a net energy gain after a laser cycle.

Before discussing the case of an electron inside the channel in the presence of a longitudinal quasi-static electric field, we first define the dephasing between the electron and the laser as

$$R = -\frac{1}{\omega} \frac{d\xi}{d\tau}, \quad (1.105)$$

where $d\tau = dt/\gamma$ is the proper time. Considering Eq. (1.101) we can write

$$R = \gamma - p_x/m_e c. \quad (1.106)$$

From Eqs. (1.97) and (1.98) it is possible to prove that $\gamma - p_x/m_e c$ is a constant

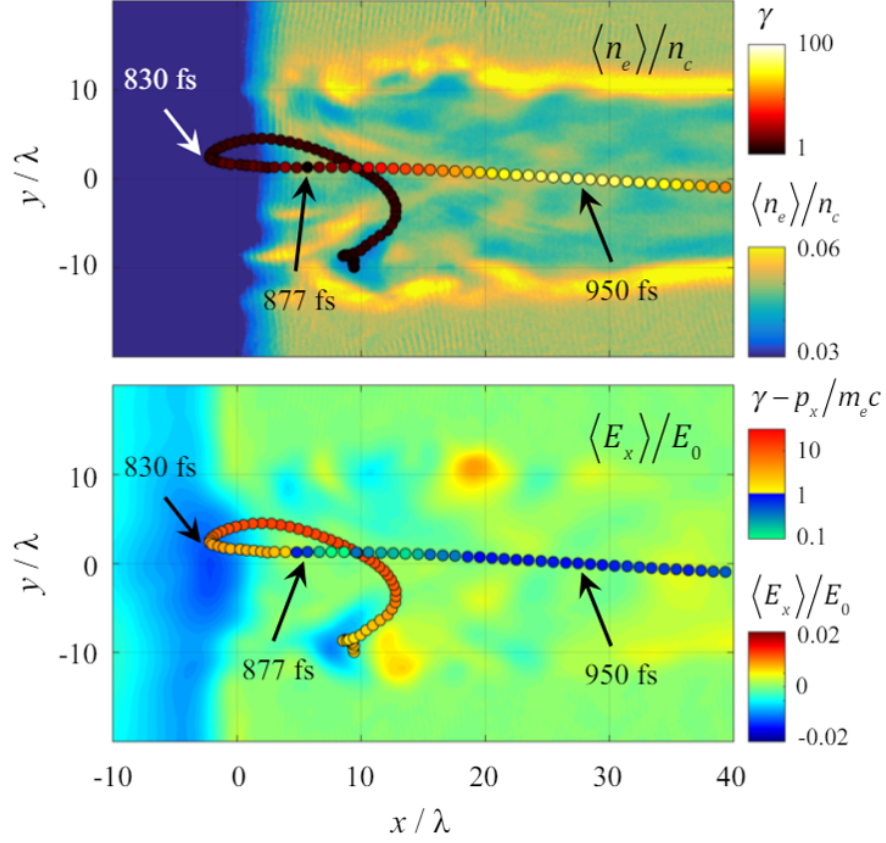


Figure 1.16: Trajectory of one accelerated particle. (top) Trajectory colored after the electron γ -factor. (bottom) Trajectory colored after the value of the longitudinal electric field $\langle E_x \rangle$ on the electron. The density and field colormaps are averaged over ten laser periods. *Figure from Arefiev et al. (2016).*

of motion. In the presence of a longitudinal quasi-static field $E_* < 0$ it is possible to show that the dephasing is reduced at a rate (Robinson et al., 2013)

$$\frac{dR}{d\xi} = \frac{e E_*}{m_e c}, \quad (1.107)$$

independently of the laser amplitude. Now, the electron can be accelerated beyond the vacuum limit and its maximum γ -factor becomes (Robinson et al., 2013)

$$\gamma_{max} \approx R^{-1} \gamma_{vac}, \quad \text{with } R < 1. \quad (1.108)$$

However, to maximize the effectiveness of dephasing reduction, it is essential for it to occur when the longitudinal momentum is at its minimum. If we assume, for example, that the longitudinal momentum is instantaneously increased by Δp_x , assuming $\Delta p_x \ll p_{x,y}$, from Eq. (1.106) we yield

$$R \approx 1 - \Delta p_x / p_x. \quad (1.109)$$

This aspect can also be observed in Fig. 1.16, where we present the results of a PIC simulation considering $n_e = 5 \times 10^{19} \text{ cm}^{-3}$ and $a_0 = 8.5$. Specifically, on both panels, we see the trajectory of one electron. In the top panel, the trajectory is colored following the particle γ -factor, while in the bottom panel the coloring refers to the dephasing $R = \gamma - p_x / m_e c$. We notice that the longitudinal field $\langle E_x \rangle / E_0$ yields a decrease of the dephasing when γ reaches its minimum at $t = 877 \text{ fs}$ (i.e., at $x \approx 0$).

1.2.4 Limitations of Laser-Plasma Accelerators

For completeness, in this section we briefly discuss the main mechanisms that can limit electron acceleration, representing an actual obstacle for common laser-plasma accelerators, where one aims at reaching the highest possible energy. However, in the context of this work, where we intend to produce the highest possible average current at low bunch energy (i.e., $< 10 \text{ MeV}$), the phenomena we present might be useful to reach our goals.

Laser Diffraction A laser pulse focused at the entrance of the plasma target will defocus along its propagation, causing its intensity to become too low to drive an accelerating wakefield. The laser diffraction length is defined as $L_{diff} = 2Z_R$, where we recall the definition of the Rayleigh length $Z_R = \pi w_0^2 / \lambda$. If we assume the laser to be transversely matched (i.e., $w_0 \sim \lambda_p$), we can write

$$L_{diff} \sim 2\pi \frac{\omega}{\omega_p} \lambda_p. \quad (1.110)$$

For distances $L > L_{diff}$ the laser intensity drastically decreases, making the laser less efficient in driving the wakefield. Furthermore, we notice that the laser diffraction is more intense with the plasma density, since $L_{diff} \propto n_e^{-1}$. Self-focusing can potentially limit this effect, otherwise one could employ a preformed plasma channel or waveguide to keep the laser focused (Oubrierie et al., 2022).

Laser Energy Depletion As we have previously stated, a decrease in the laser intensity entails a less efficient generation of the wakefield. Hence, a significant loss in laser energy could also limit the maximum energy gain (Bulanov et al., 1992, Shadwick et al., 2009). For a linearly polarized pulse, the pump depletion length L_{depl} can be estimated as (Esarey et al., 2009)

$$L_{depl} = \left(\frac{\omega}{\omega_p}\right)^2 \lambda_p \times \begin{cases} 2/a_0^2 & \text{for } a_0 \leq 1 \\ 1 & \text{for } a_0 \gg 1. \end{cases} \quad (1.111)$$

Lu et al. (2007), instead, estimates the depletion length of a linearly polarized laser as

$$L_{depl} = \left(\frac{\omega}{\omega_p}\right)^2 \frac{\omega_p \tau_0}{k_p} \quad \text{for } a_0 > 2. \quad (1.112)$$

Electron Dephasing As briefly mentioned in Section 1.2.2, when an electron is injected in a plasma period, it is quickly accelerated to the point of exceeding the plasma wave velocity. This means that the electrons can cross regions inside the cavity where the wakefield is zero, moving towards the decelerating phase of the wave and start losing energy. The characteristic length over which we can observe this phenomenon is called dephasing length (L_{deph}). Esarey et al. (2009) estimates the dephasing length for the linear and non-linear acceleration regimes:

$$L_{deph} = \left(\frac{\omega}{\omega_p}\right)^2 \lambda_p \times \begin{cases} 1 & \text{for } a_0 \leq 1 \\ 4\sqrt{a_0}/3 & \text{for } a_0 \gg 1. \end{cases} \quad (1.113)$$

1.3 State of the Art

In view of increasing the average current of laser-plasma accelerators, here, we briefly mention some known results about nanocoulomb-class electron beams. For instance, Götzfried et al. (2020) was able to produce ~ 340 pC electron beams with energies up to 216 MeV. This was achieved using a 2 J, 27 fs class laser and by employing the *shock-front injection* (Suk et al., 2004, Schmid et al., 2010b). This technique relies on the generation of a controlled shock in a supersonic gas flow, producing a sharp density downramp. The rapid drop in plasma density causes the ion cavity to suddenly expand and reduce its velocity at the rear. This allows for a localized injection of electrons in a trapping region of the accelerating structure. Other studies employing techniques as the *self-truncated ionization injection* (Couperus Cabadağ et al., 2017) have also demonstrated their potential in producing hundreds-pC quasi-monoenergetic electron beams. Nonetheless, in this

work, we aim at producing the highest possible average current with energies below ~ 10 MeV. Despite the improved charge that one can obtain via shock injection or similar techniques, the trapping of electrons in the ion cavities yields beam energies exceeding this threshold, owing to the intense electric field inside the accelerating structure. This, in turn, virtually makes any trapping mechanism incompatible with the objectives of this thesis. Other works (Guillaume et al., 2015, Feng et al., 2023) were able to experimentally prove the production of highly charged, low energy electron beams using pure argon and nitrogen. Specifically, Feng et al. (2023) was able to obtain up to around 15 nC using a 1.2 J, 45 fs laser pulse and with nitrogen plasma densities exceeding 10^{19} cm^{-3} . The vast majority of the charge is below 10 MeV and *energy conversion efficiency*, defined as the ratio of total electron energy to the laser energy is $\eta = 12.5\%$. In both studies, the electron beam acceleration process is attributed to the injection in several ion cavities, resulting in quasi-Maxwellian energy spectra. Lastly, Yang et al. (2017) numerically produced electron beams with charges between 4 nC and 10 nC, accelerated to just a few-MeVs. This was achieved using pure helium ionized to $1 - 2 \times 10^{19} \text{ cm}^{-3}$ and a laser normalized vector potential $a_0 \in [1, 3]$, findings which were corroborated by experimental results. In this case, the numerical study proves that most of the charge produced is not injected, as also discussed by Behm et al. (2019).

1.4 Conclusion

In this first chapter, we have provided a comprehensive overview of the physics of laser-plasma accelerators, with the support of the results present in the literature to date. Specifically, we have outlined the main injection and acceleration regimes and also presented the challenges that still hinder the development of an actual laser-plasma accelerator. Finally, with careful attention to the objectives of this thesis, we have concluded this chapter discussing some works in the literature devoted to the increase of the electron beam charge. Notably, Feng et al. (2023) demonstrated how to produce a ~ 15 nC, few-MeV beam with a $\sim 12.5\%$ conversion efficiency, redefining the state of the art of high-current laser-plasma accelerators. The experimental conditions allowing for the achievement of such a high charge are of great interest for this thesis, as it will be further investigated in Chapter 4 and 5. Here, we will present the main findings of this thesis, making use of the rudiments and notions introduced in this chapter. Nonetheless, before delving into our contributions, we wish to discuss the methods employed for our study in the upcoming chapter.

Chapter 2

Methods

In this chapter, we explore the numerical and experimental tools utilized in this work. We begin by providing a concise overview of the *Fourier-Bessel Particle-in-Cell* (FBPIC) code, which plays a crucial role in our investigation of the laser-plasma interaction. Subsequently, we present the Salle Jaune laser system at LOA, detailing its configuration and capabilities. Finally, we conclude by discussing the diagnostics employed for the experimental studies.

Contents

2.1 Numerical Simulations of Laser-Plasma Accelerators . . .	44
2.1.1 Particle-In-Cell Method	44
2.1.2 FBPIC: Fourier-Bessel Particle-In-Cell	48
2.2 Salle Jaune Laser System	49
2.3 Diagnostics	51
2.3.1 Electron Spectrometer	51
2.3.2 Beam Profile Monitor	52
2.3.3 Phasics SID4 Camera	53
2.3.4 Focal Spot Camera	54
2.3.5 Dosimetry Stack	55
2.4 Conclusion	57

2.1 Numerical Simulations of Laser-Plasma Accelerators

2.1.1 Particle-In-Cell Method

As we have briefly mentioned in Section 1.1.1, the kinetic model offers the most general description of plasmas. At the basis of this theory lies the *Vlasov equation* (Vlasov, 1968)

$$\frac{\partial f_a}{\partial t} + \mathbf{v} \cdot \nabla_{\mathbf{r}} f_a + q_a(\mathbf{E} + \mathbf{v} \times \mathbf{B}/c) \cdot \nabla_{\mathbf{p}} f_a = 0, \quad (2.1)$$

where $f_a = f_a(\mathbf{r}, \mathbf{p}, t)$ is the distribution function of the particle species a . This function provides the particle density at the point (\mathbf{r}, \mathbf{p}) in phase space at the time t . Here, we consider a classical and collisionless plasma. Hence, thanks to Vlasov equation we can retrieve the first and second-order moment of the density distribution

$$n_a(\mathbf{r}, t) = \int f_a(\mathbf{r}, \mathbf{v}, t) d\mathbf{v}, \quad (2.2)$$

$$\mathbf{u}_a(\mathbf{r}, t) = \frac{1}{n_a(\mathbf{r}, t)} \int \mathbf{v} f_a(\mathbf{r}, \mathbf{v}, t) d\mathbf{v}, \quad (2.3)$$

which represent the total particle density (n_a) and the mean velocity (\mathbf{u}_a) respectively. From Eq. (2.2) and Eq. (2.3) we can obtain the charge density ϱ and the current density \mathbf{J} , necessary to yield the electromagnetic field via Maxwell's equations

$$\varrho(\mathbf{r}, t) = \sum_a q_a n_a(\mathbf{r}, t), \quad (2.4)$$

$$\mathbf{J}(\mathbf{r}, t) = \sum_a q_a n_a(\mathbf{r}, t) \mathbf{u}_a(\mathbf{r}, t) \quad (2.5)$$

The resulting system of equations¹ has very few analytical solutions. The most common way to find solutions lies in efficient numerical methods offered by the Particle-In-Cell (PIC) approach (Dawson, 1983, Birdsall and Langdon, 2004). Nevertheless, solving this system of equations can still be extremely demanding, mainly due to the phase space dimension. In some instances, it is possible to reduce the computational effort, for example, by assuming the plasma ions to be fixed, since their mass is much larger than that of the electrons. Alternatively, it is possible to keep a complete kinetic description for one species and consider a simplified model for the others. However, when dealing with laser-plasma

¹Usually referred to as Vlasov-Maxwell system.

acceleration simulations, it is still necessary to solve the full kinetic equations in order to obtain detailed information such as the energy spectra.

The PIC method to solve the Vlasov equation consists in assuming the following discretization of the distribution function (Macchi, 2013)

$$f(\mathbf{r}, \mathbf{p}, t) = A \sum_{l=0}^{N_p-1} g[\mathbf{r} - \mathbf{r}_l(t)] \delta^3[\mathbf{p} - \mathbf{p}_l(t)], \quad (2.6)$$

where N_p is the number of *macroparticles*, $\mathbf{r}_l(t)$ and $\mathbf{p}_l(t)$ are the position and momentum of the l macroparticle and A is a normalization constant. The problem is thus reduced to $2N_p$ equations of motion, describing the dynamics of N_p macroparticles. Furthermore, one macroparticle regroups multiple particles having similar coordinates in the phase space. In Eq. (2.6) we define $\delta^3(\mathbf{p}) = \delta(p_x)\delta(p_y)\delta(p_z)$, where $\delta(p)$ is the Dirac function and $g(\mathbf{r})$ is an even function with properties similar to δ^3 , describing the charge profile distribution associated to a particle. From Eqs. (2.4), (2.5) and (2.6) we can write

$$\varrho(\mathbf{r}, t) = A \sum_{a,l} q_a g[\mathbf{r} - \mathbf{r}_{a,l}(t)], \quad (2.7)$$

$$\mathbf{J}(\mathbf{r}, t) = A \sum_{a,l} q_a \mathbf{v}_l g[\mathbf{r} - \mathbf{r}_{a,l}(t)]. \quad (2.8)$$

The PIC method requires both ϱ , \mathbf{J} and the electromagnetic field to be discretized on a spatial grid. Thus, the position of the particle on the grid and its charge distribution determine the contribution to the total current in the grid cells overlapping with the particle and the average force on the particle. Fig. 2.1 shows the simple case of a triangular-shape $g(\mathbf{r})$ function, extending over twice the grid spacing. Here, the particle overlaps 3^D cells, where D is the dimensionality of the problem. Hereby, we will present a simple description of the PIC method in the 1D case, following the approach of Macchi (2013). Further details can be found in Birdsall and Langdon (2004) and Gibbon (2005, 2012), where the PIC method is extensively described. Here, we will assume time in units of ω^{-1} , space in units of c/ω , momenta in units of $m_e c$, fields in units of $m_e \omega c/e$ and densities normalized to the critical density $n_c = m_e \omega^2 / 4\pi e^2$. Assuming x as the only spatial coordinate, normalized Maxwell's equations for the transverse fields read

$$\frac{\partial E_y}{\partial t} = -J_y - \frac{\partial B_z}{\partial x}, \quad \frac{\partial B_z}{\partial t} = -\frac{\partial E_y}{\partial x}, \quad (2.9)$$

$$\frac{\partial E_z}{\partial t} = -J_z + \frac{\partial B_y}{\partial x}, \quad \frac{\partial B_y}{\partial t} = \frac{\partial E_z}{\partial x}. \quad (2.10)$$

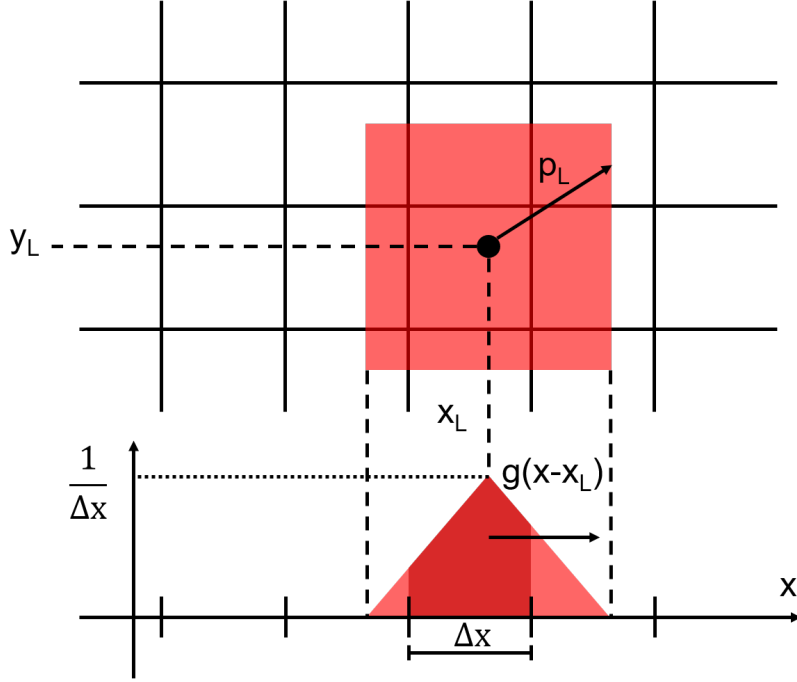


Figure 2.1: Depiction of a particle moving across the grid in the PIC approach. Here, the particle is described by a normalized triangular density profile g , whose width spans over twice the grid spacing.

To integrate these equations we introduce $F_{\pm} = E_y \pm B_z$ and $G_{\pm} = E_z \pm B_y$, which satisfy

$$\left(\frac{\partial}{\partial t} \pm \frac{\partial}{\partial x} \right) F_{\pm} = -J_y, \quad \left(\frac{\partial}{\partial t} \pm \frac{\partial}{\partial x} \right) G_{\mp} = -J_z. \quad (2.11)$$

F_{\pm} and G_{\mp} define waves propagating from left to right and right to left respectively. Hence, we can integrate Eq. (2.11) using the following second-order-accurate scheme

$$F_{\pm}(x \pm \Delta x, t + \Delta t) = F_{\pm}(x, t) - J_y(x \pm \Delta x/2, t + \Delta t/2)\Delta t, \quad (2.12)$$

$$G_{\pm}(x \mp \Delta x, t + \Delta t) = G_{\pm}(x, t) - J_z(x \mp \Delta x/2, t + \Delta t/2)\Delta t, \quad (2.13)$$

where the spatial resolution is taken equal to the timestep, i.e. $\Delta x = \Delta t$. From Eqs. (2.12) and (2.13) we notice that the transverse current is entangled in space and time with the transverse fields. Indeed, if F_{\pm} and G_{\pm} are defined at the cell boundaries (i.e., at $x_i = i\Delta x$, with $i = 0, 1, \dots, N-1$) and at timesteps $t_n = n\Delta t$, with $n = 0, 1, \dots$, then J_y and J_z are defined at the cell centers $x_i = (i + 1/2)\Delta x$

for $t_n = (n + 1/2)\Delta t$.

Concerning the longitudinal field E_x , we can solve the 1D Poisson's equation $\partial_x E_x = \rho$:

$$\begin{aligned} E_x(x, t) &= E(x - \Delta x, t) + \int_{x-\Delta x}^x \rho(x', t) dx' \\ &= E(x - \Delta x, t) + \rho(x - \Delta x/2, t)\Delta x + O(\Delta x^2). \end{aligned} \quad (2.14)$$

Therefore, the charge density must be defined at cell centers.

Considering the triangular shape presented in Fig. 2.1 for the 1D case, each particle overlaps three cells. Moreover, its weights are given by the area of the shaded regions in the bottom frame of Fig. 2.1 divided by the cell length Δx . The weighting factors are a function of $x_l - x_i$, where x_l is the position of the particle and x_i is the position of the parent cell (i.e., such that $|x_l - x_i| < \Delta x/2$). For this specific case, we can introduce

$$S_{-1} = \frac{1}{2} \left(u - \frac{1}{2} \right)^2, \quad S_0 = \left(\frac{3}{4} - u^2 \right), \quad S_{+1} = \frac{1}{2} \left(u + \frac{1}{2} \right)^2, \quad (2.15)$$

where $u = (x_l - x_i)/\Delta x$. Using Eq. (2.15) we can write the electric field on the l th particle as

$$\bar{\mathbf{E}}_l = \sum_{j=-1}^{j=+1} S_j(u) \mathbf{E}_{i+j}, \quad (2.16)$$

where \mathbf{E}_j is the field on the $(i + j)$ th cell, with $i + j = i - 1, i, i + 1$.

Once we have discussed a scheme to advance the fields in time, we now introduce an algorithm called *Boris pusher*, which will allow us to advance the particle momenta. We assume to know the particle momentum \mathbf{p} at the timestep $n - 1/2$ and the electromagnetic fields at the timestep n (we drop the particle index for simplicity). We first perform a ‘‘half-boost’’ by the electric field

$$\mathbf{p}^{(-)} = \mathbf{p}^{(n-1/2)} + \frac{q}{m} \bar{\mathbf{E}}^{(n)} \frac{\Delta t}{2}, \quad (2.17)$$

then, we rotate the momentum through the magnetic field in two steps

$$\mathbf{p}^{(0)} = \mathbf{p}^{(-)} + \mathbf{p}^{(-)} \times \mathbf{t}, \quad \mathbf{p}^{(+)} = \mathbf{p}^{(-)} + \mathbf{p}^{(0)} \times \mathbf{s}, \quad (2.18)$$

where we have defined

$$\gamma^{(n)} = \sqrt{1 + (\mathbf{p}^{(-)}/mc)^2}, \quad \mathbf{t} = \frac{q\bar{\mathbf{B}}^{(n)}}{m\gamma^{(n)}c}, \quad \mathbf{s} = \frac{2\mathbf{t}}{1 + t^2}. \quad (2.19)$$

The momentum is completely updated performing another half-boost of the electric field:

$$\mathbf{p}^{(n+1/2)} = \mathbf{p}^{(+)} + \frac{q}{m} \bar{\mathbf{E}}^{(n)} \frac{\Delta t}{2} \quad (2.20)$$

Finally, the particle position is advanced using the *leapfrog scheme*, which requires the coordinates to be defined at integer timesteps:

$$\hat{\mathbf{x}}^{(n+1)} = \hat{\mathbf{x}}^{(n)} + \mathbf{v}^{(n+1)} \Delta t, \quad \mathbf{v}^{(n+1/2)} = \frac{\mathbf{p}^{(n+1/2)}}{m\gamma^{(n)}} \quad (2.21)$$

Both the Boris pusher and the leapfrog scheme are second-order accurate.

2.1.2 FBPIC: Fourier-Bessel Particle-In-Cell

FBPIC (Fourier-Bessel Particle-In-Cell) is a fully parallelizable PIC code for relativistic plasma physics, particularly suitable for laser and plasma wakefield acceleration. FBPIC uses a spectral cylindrical representation of the fields (Lehe et al., 2016), making it fast and accurate for quasi-cylindrical systems. Hence,

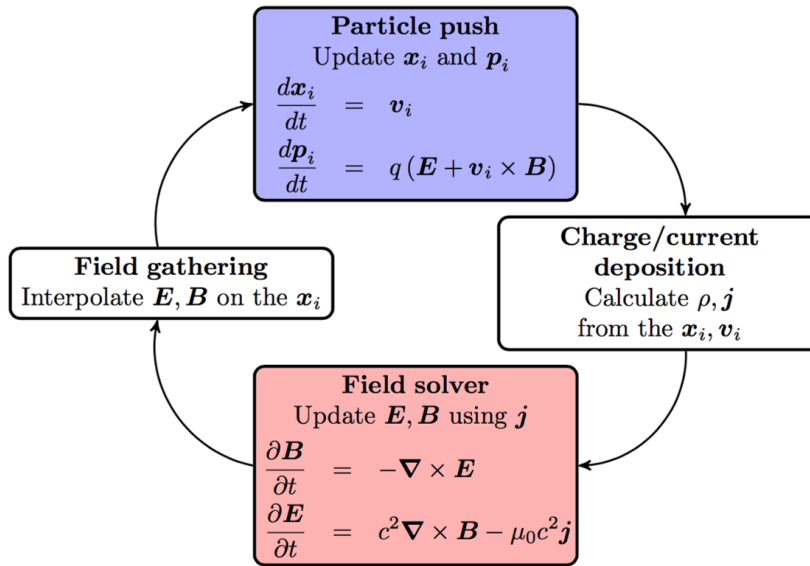


Figure 2.2: FBPIC cycle. First, the electromagnetic field is gathered from the grid, then the particles are pushed. Secondly, the resulting charge and current are deposited on the grid. Finally, the electromagnetic field is updated. *Figure from [fbpic.github.io](https://github.com/fbpic).*

instead of using a 3D Cartesian grid, which is computationally expensive, the

code employs a set of 2D radial grids. Each radial grid represents an azimuthal mode (Lifschitz et al., 2009), labeled by the integer m . The grid with $m = 0$ represents the fields that are independent of θ . In the case of laser wakefield acceleration, the grid for $m = 0$ ideally corresponds to the wakefield. On the other hand, for $m = 1$ the grid represents the fields that vary proportionally to $\cos \theta$ and $\sin \theta$. Considering, once again, the case of laser wakefield acceleration, the grid for $m = 1$ would be linked to the linearly polarized laser field, expressed in cylindrical coordinates (i.e., E_r and E_θ). When considering $m > 1$, the grid is related to the part of the fields that vary proportionally to $\cos m\theta$ and $\sin m\theta$. The user can choose the number of modes in the code, however, a sufficient number of modes is required to properly resolve non-linear effects, such as self-injection. Usually, it is recommended to choose $m = 3$.

Regarding the discretization of the spatial and time derivatives in Maxwell's equations, PIC codes usually employ the *finite-difference* method. However, this could lead to the appearance of many numerical artifacts, such as the numerical growth of emittance for relativistic beams (Lehe et al., 2013). FBPIC, instead, solves the fields in spectral space, where Maxwell's equation can be analytically solved in time and the derivatives are better evaluated (Lehe et al., 2016). Hence, at each timestep, the code transforms the fields to the spectral space, updates them and transforms them back to the real space. Furthermore, FBPIC's field solver has no Courant limit (Birdsall and Langdon, 2004) and thus the timestep can be chosen freely.

One last FBPIC's features worth mentioning concerns the presence of an ionization module. Indeed, the code employs the ADK model to properly account for gas ionization, which, as discussed in Section 1.2.3, can play a relevant role while dealing with laser wakefield acceleration.

2.2 Salle Jaune Laser System

As shown in Fig. 2.3, the Salle Jaune at LOA is divided into two separate rooms: the first floor hosts the actual laser system, while the ground floor is dedicated to the experimental activities. The environment is controlled in humidity and temperature to ensure the laser stability. In Fig. 2.3 we present the laser system architecture that is based on the *Chirped Pulse Amplification* (CPA) (Strickland and Mourou, 1985). This technique consists of the laser pulse amplification after a temporal stretch, followed by a temporal compression. This allows to reach high laser intensities avoiding any damage to the amplifying medium or optics in the laser path. The laser system starts with a Ti:Sapphire mode-locked oscillator delivering pulses of 4 nJ and 9 fs at 88 Hz. Their spectrum is centered around 808 nm with a Full Width

at Half Maximum (FWHM) of ~ 100 nm. These pulses are then stretched to 20 ps and amplified to 2 mJ and their frequency drops to 10 Hz. Before passing through a *Cross-Polarized Wave* (XPW) filter, allowing for a high temporal contrast between the laser peak intensity and the noise level, they are compressed to 20 fs. Using an Öffner system, the pulses are stretched up to 600 ps and a Dazzler acousto-optic modulator (Verluise et al., 2000) allows to control their spectral phase. This is done to pre-compensate the spectral compression experienced by the pulses while passing through the five amplification stages. All amplifiers are composed by a Ti:Sapphire crystal pumped with a 532 nm Nd:Yag laser, allowing for the pulses to reach 7 J. The size of each amplifier crystal progressively increases to keep the laser fluence below the damage threshold (i.e., ~ 100 mJ/cm²). At this stage, the laser frequency is 1 Hz and afocal systems are employed to change the beam size. The resulting laser exiting the fifth amplification stage is then split into two separate beams using a beam splitter. These pulses are subsequently sent to attenuation and delay lines composed of optical densities and *half-waveplates*. Hence, we can control their energy and synchronization. The resulting beams are 100 mm and 30 mm in diameter with a duration of ~ 30 fs. They deliver 1.6 J and 0.1 J on target (i.e., in the experimental chamber) respectively. In the following, we will refer to the first pulse as the *driver beam*, while the second is the *probe beam*. The former is responsible for the plasma generation and the whole laser-plasma interaction, while the latter is used to probe the plasma density.

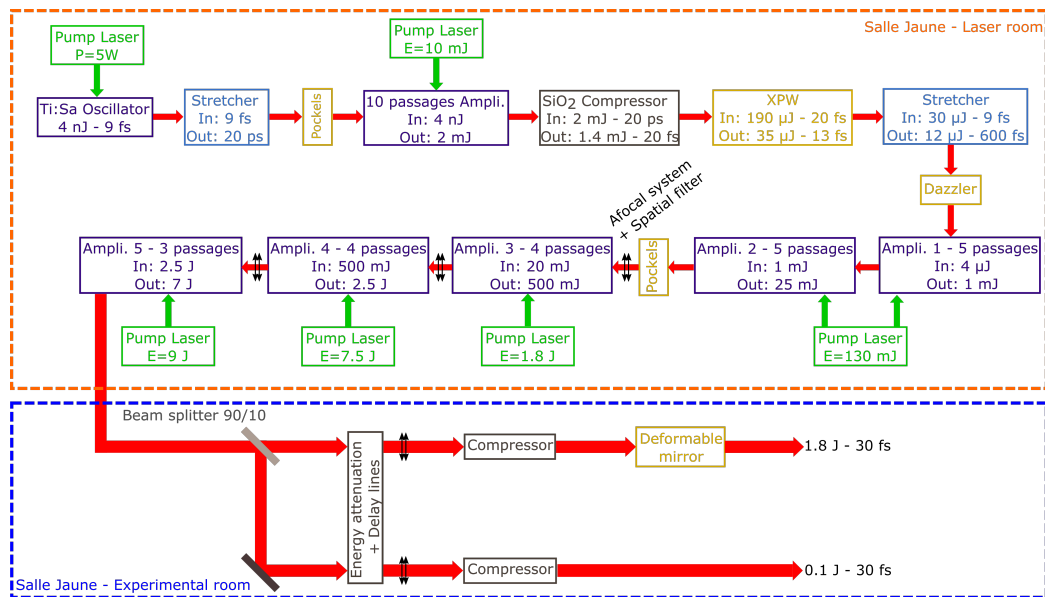


Figure 2.3: Salle Jaune laser system architecture. *Figure adapted from Kabacinski (2022).*

2.3 Diagnostics

2.3.1 Electron Spectrometer

The spectrometer is a diagnostic allowing to measure the electron beam's energy. As will be discussed in further detail in Chapter 4, the electrons we obtained are highly divergent and they present wide energy spreads, making the spectrometry a challenging task. The spectrometry technique we employed is based on the simple scheme presented in Fig. 2.4(a). Here, this diagnostic is composed

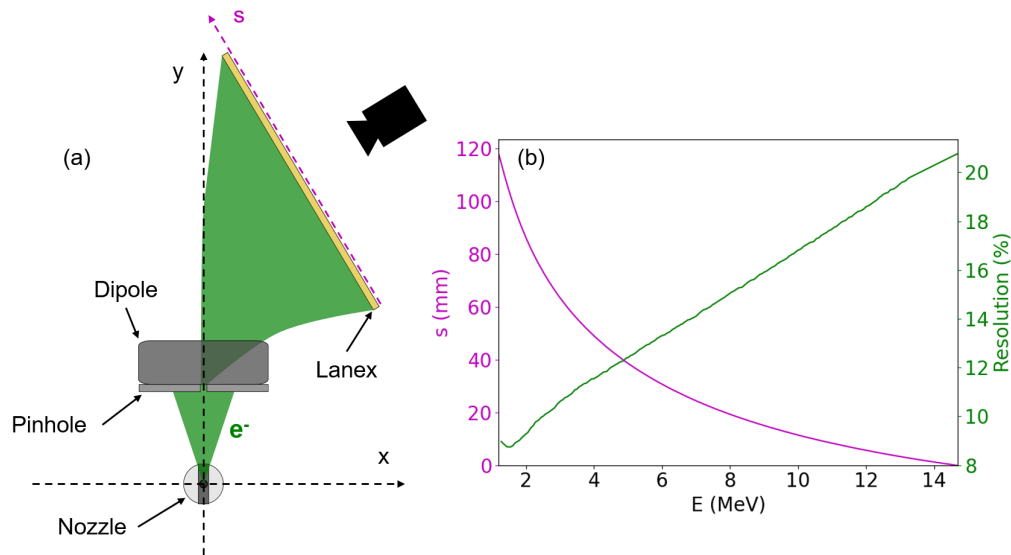


Figure 2.4: (a) Electron spectrometer composed by a magnetic dipole that deviates the electrons on a Lanex Regular Carestream screen. Each electron interacts with the screen on a different position, depending on its energy. The light produced is then collected by a CCD camera. (b) Spectrometer calibration employed for the experiments discussed in Chapter 4. Here, we show the position of each electron s on the Lanex screen and the corresponding resolution as functions of the electrons' energy E .

of a permanent magnetic dipole, a scintillating Lanex Regular Carestream screen and a CCD camera, allowing to record shot-to-shot images of the energy spectra. The development of magnetic dipoles is part of this work and it will be discussed in further detail in Chapter 3. The dipole allows to deviate the electrons on the scintillating screen and the emitted light is then collected on a CCD camera, with an exposure time of 100 ms. The relative electron position on the Lanex screen (i.e., the s coordinate in Fig. 2.4(a)) depends on its energy (E), thus allowing to

reconstruct the original beam energy. In Fig. 2.4(b) we show the spectrometer calibration used for the experiments discussed in Chapter 4, where the dipole has been positioned at 6 cm from the gas nozzle. Here, we have employed a Lanex screen of 120 mm in length, allowing to detect electrons with energies between 1.2 MeV and 14.7 MeV. In Fig. 2.4(b) the green curve represents the resolution of the spectrometer, defined as $R(\%) = \Delta E/E$, where ΔE is the energy uncertainty of each spectral component, which has been calculated considering the beam divergence imposed by the 2mm-diameter pinhole at the front of the dipole (i.e., ~ 1.2 msr).

2.3.2 Beam Profile Monitor

The Beam Profile Monitor (BPM), along with the energy spectrometer, represents one of the main diagnostics of this thesis. Specifically, the BPM has been employed to estimate the beam charge and divergence. Both the BPM and the spectrometer have been motorized, allowing to easily position the former or the latter when necessary. In Fig. 2.5(a) we show a schematic representation of the BPM, which simply consists of 75 mm diameter Lanex screen that can be moved close to the electron source via a 10 cm motorized stage. The light produced by

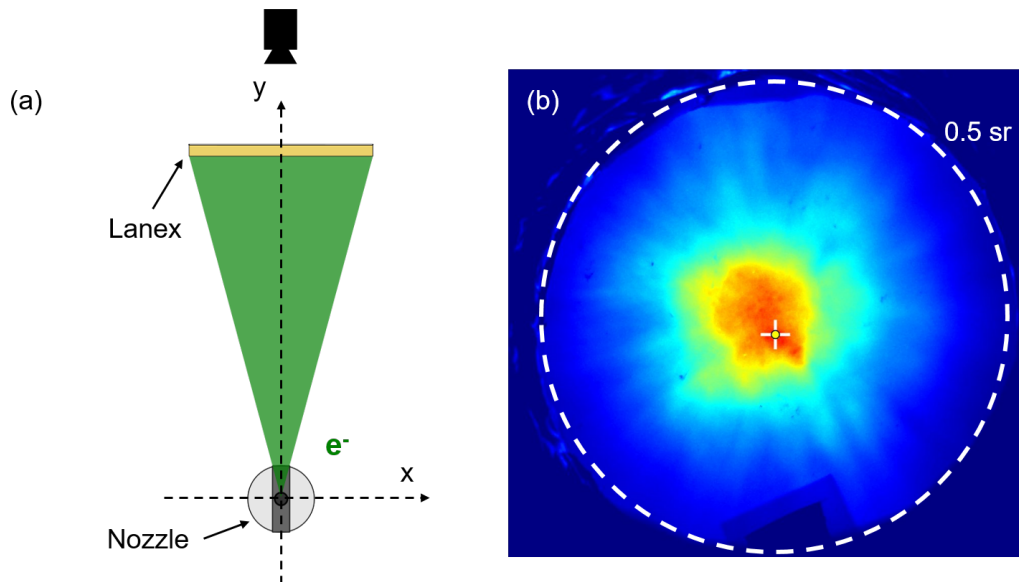


Figure 2.5: (a) Schematic view of the motorized Beam Profile Monitor. (b) Colorized image acquired with a 16-bit CCD Andor Solis camera of the BPM Lanex screen. From this image, we are able to determine the beam charge inside a given solid angle (dashed circle) and divergence.

the scintillator is subsequently collected with a 16-bit CCD Andor Solis camera. In Fig. 2.5(b) it is possible to observe an example of the images acquired by the CCD camera with an exposure time of 100 ms. Assuming an energy spectrum, we retrieve the beam charge in a given solid angle (i.e., dashed circle in Fig. 2.5(b)) using a calibrated tritium capsule (Kuruz et al., 2018). Furthermore, knowing the distance between the scintillating screen and the gas nozzle, it is also possible to deduce the beam dimension. In the experiment of Chapter 4, the BPM Lanex screen was positioned at 130 mm or 80 mm from the electron source, corresponding to a solid angle of around 0.25 sr and 0.5 sr respectively.

2.3.3 Phasics SID4 Camera

A transverse laser pulse propagating through a plasma (or neutral gas) undergoes a phase shift depending on the density, owing to the local refractive index. Specifically, the integral of the refractive index along the laser path is encoded into the beam phase. The Phasics SID4 Camera (Primot and Sogno, 1995) is a wave-front sensor allowing to measure the phase and retrieve the integral of the refractive index. Assuming cylindrical symmetry and thanks to an Abel inversion (Bracewell, 2000) it is then possible to deduce the medium density. In this thesis, this operation has been carried out using the code Neutrino (Flacco, 2013).

In order to understand the Abel inversion performed with Neutrino, let us consider the example presented in Fig. 2.6. Here, we consider a plasma traversed by a probe laser that undergoes a phase shift. We assume that the plasma has been generated by a superintense laser beam propagating along the R axis. We define $\phi(r)$ as the dephasing function, where ($r = \sqrt{x^2 + y^2}$), and we assume $\phi(r)$ to be symmetrical with respect to the R axis. Moreover, it can be shown that (Oubrierie, 2022)

$$\phi(r) = \frac{n(r) - 1}{\lambda} \sqrt{2}r = \frac{\sqrt{1 - n_e(r)/n_c} - 1}{\lambda} \sqrt{2}r, \quad (2.22)$$

Here, λ is the laser wavelength and $n(r)$ is the plasma refractive index as presented in Eq. (1.40). Thus, the camera in Fig. 2.6 will collect the following integral of the dephasing function

$$N(y) = \int_{-\infty}^{+\infty} \phi(\sqrt{x^2 + y^2}) dx. \quad (2.23)$$

Knowing that $n(r)$ is an even function and considering that $dx = r dr / \sqrt{r^2 - y^2}$, from Eq. (2.23) we can write the Abel transform of $\phi(r)$

$$N(y) = 2 \int_{|y|}^{+\infty} \phi(r) \frac{r dr}{\sqrt{r^2 - y^2}}. \quad (2.24)$$

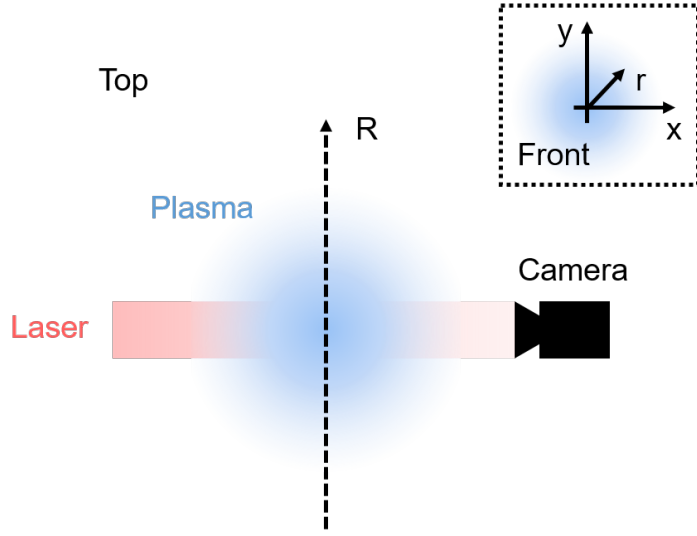


Figure 2.6: Schematic depiction of the Phasics SID4 Camera: a laser pulse undergoes a phase shift traversing a plasma. The camera detects the dephasing that allows to reconstruct the density profile.

Here, we understand the importance of a proper choice in the symmetry axis, since it defines the extremes of integration. Furthermore, it is possible to compute the inverse Abel transform of Eq. (2.24), which reads

$$\phi(r) = -\frac{1}{\pi} \int_r^{+\infty} \frac{dN(y)}{dy} \frac{dy}{\sqrt{y^2 - r^2}}. \quad (2.25)$$

Hence, measuring $N(y)$ with the camera and performing the operation in Eq. (2.25) allows us to finally retrieve the plasma density profile.

In Fig. 2.7 we show an example of density reconstruction employing the technique we have discussed above. This figure has been obtained through the ionization of a nitrogen supersonic gas jet. The plasma is produced at $\sim 500 \mu\text{m}$ from the nozzle exit, whose diameter measures 0.4 mm. Fig. 2.7(a) represents the dephasing Θ and Fig. 2.7(b) illustrates the corresponding density map n_e . Here, we also show the inversion axis R that allows to perform the Abel inversion with Neutrino.

2.3.4 Focal Spot Camera

In order to properly align the laser pulse and control for eventual aberrations on the focal spot, we have employed a 1-inch diameter pick-up mirror to deflect the

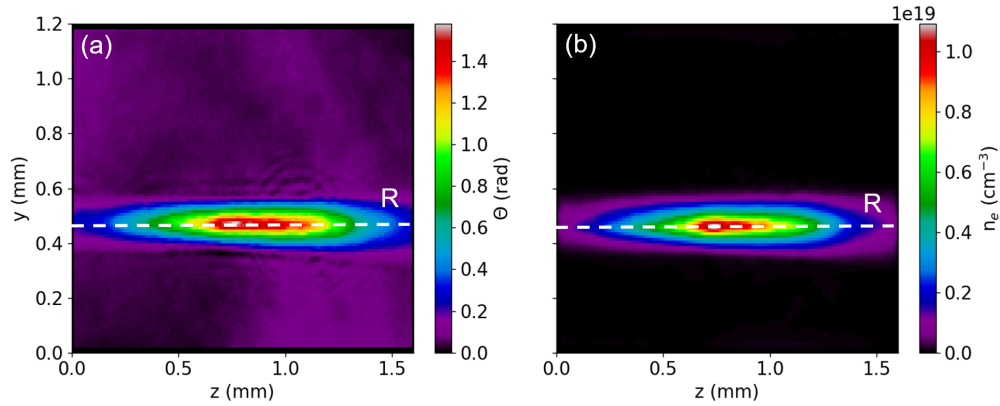


Figure 2.7: Example of density reconstruction. Here, we retrieve the plasma density profile produced with a supersonic nozzle. (a) Dephasing map obtained with the Phasics SID4 Camera. (b) Density map derived with Neutrino. In both images we show the inversion axis R .

laser on a 8-bit Allied Vision CCD camera, as shown in Fig. 2.8(a). In this case, the laser pulse energy is reduced to avoid damaging both the pick-up mirror and the camera. Here, it is also possible to observe the achromatic 20x/0.4 microscope objective installed on the camera to properly observe the laser focal spot. In Fig. 2.8(b) and (c) we show two images obtained with the scheme in Fig. 2.8(a) and using a $f/4$ and $f/8$ off-axis parabola respectively. These images allow to estimate the laser FWHM diameter d and the normalized vector potential a_0 and the energy within the laser central peak.

2.3.5 Dosimetry Stack

In order to gauge the doses of the electron beams we produced in this work, we have employed a dosimeter stack, as represented in Fig. 2.9. Here, we illustrate an exploded view of the stack, composed of bricks in aluminum and Teflon of different thicknesses. In Fig. 2.9 the values represent the width of each brick in millimeters. Between each brick, we interpose a GAFchromic EBT3 film (Ashland, 2024), for a total of eleven sheets. The stack is placed inside the vacuum chamber at 6 cm from the electron source, as highlighted by the inset of Fig. 2.9. Therefore, as the electron beam passes through the stack, it imparts a specific dose onto each film, causing them to darken. The intensity of this darkening correlates with the dose received, with higher doses resulting in a more pronounced blackening effect, as depicted in Fig. 2.10(a). In this figure, we showcase the first four radiochromic films from the stack, irradiated during one experimental campaign. Naturally, the sheets

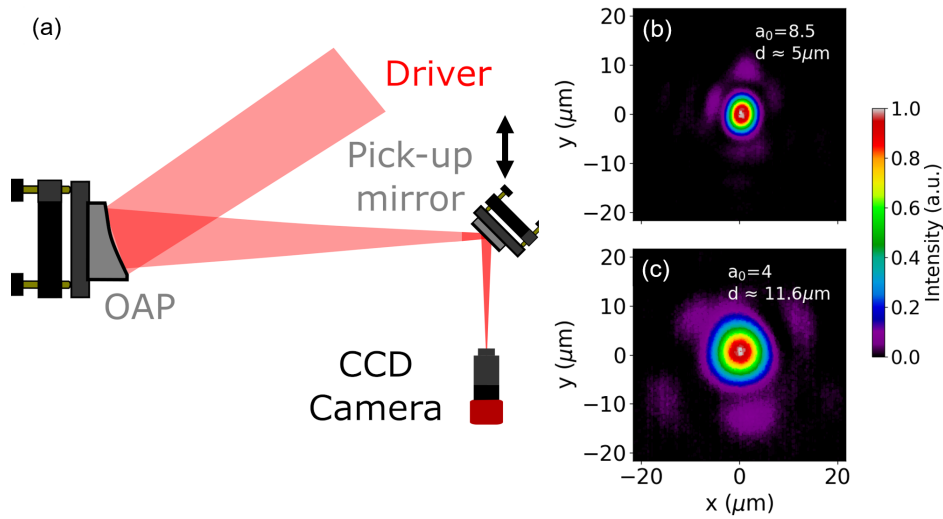


Figure 2.8: (a) Focal spot camera scheme. Here, it is possible to observe the pick-up mirror, that deflects the laser pulse on a 8-bit CCD camera. This allows to control and correct for eventual aberrations and to estimate the laser FWHM diameter d , a_0 and energy within the laser central peak. (b-c) Images recorded with the CCD camera with a $f/4$ and $f/8$ off-axis parabola.

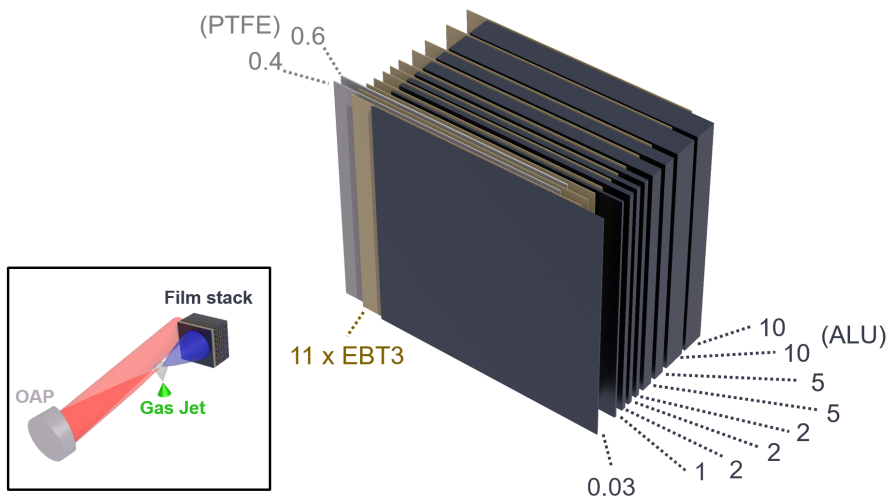


Figure 2.9: Exploded view of the dosimetry stack, composed by eleven GAFchromic EBT3 films. We separate each film with bricks in aluminum or Teflon of different thicknesses. The values on the image refer to the width of each brick in millimeters. (Inset) The stack was placed at 6 cm from the electron source in the experimental chamber.

closer to the electron source (i.e., at shallower depths within the stack) received higher doses. Further insights about these results can be found in Chapter 4. To determine the dose on each film, it is necessary to perform a proper calibration of these dosimeters. In the context of this thesis, the calibration is carried out by homogeneously irradiating eight EBT3 sheets with a conventional accelerator. By allowing a beam of light to traverse each sheet, the exiting beam will be damped by a factor 10^{-OD} , where OD is the optical density of each film. Consequently, we can associate an optical density to a specific dose and deduce a calibration curve of these dosimeters, as displayed in Fig. 2.10(b). Using this curve, it is subsequently possible to estimate the dose distribution on each film composing the dosimetry stack.

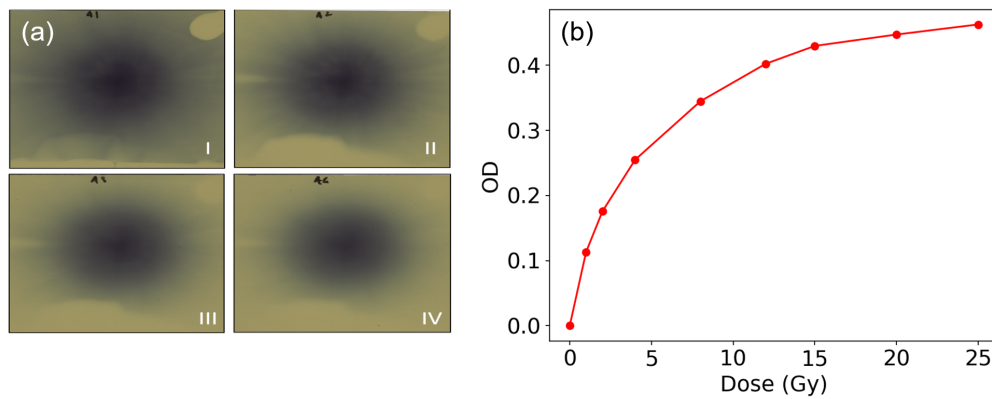


Figure 2.10: (a) First four GAFchromic EBT3 films from the dosimetry stack, as indicated by the Roman numerals. (b) Calibration curve of the radiochromic films used in this thesis.

2.4 Conclusion

In this chapter, we explored the primary tools used for conducting the research activities outlined in this thesis. We began by discussing the main features of FBPIC, the code utilized for the Particle-In-Cell simulations presented in Chapter 5. Subsequently, we provided an overview of the laser systems employed for the experimental campaigns. We then delved into the diagnostics, focusing particularly on the electron spectrometer. Throughout this chapter, we highlighted the importance of this diagnostic and the challenges associated with measuring electron beams with divergences exceeding hundreds-mrad. Furthermore, while discussing the technique employed for energy measurement, we emphasized the necessity of

a magnetic dipole specifically developed for the energy range of interest. In the following chapter, we will address the development of these devices, along with the development of gas targets, which are essential components of the experiments conducted in this work.

Chapter 3

Development of Gas Targets and Magnetic Dipoles

In this chapter, we explore the development of crucial components for the experimental campaign. First, we briefly introduce the notion of supersonic nozzles, which are widely used for the generation of laser-plasma accelerated electron beams. Subsequently, we illustrate an example of *Computational Fluid Dynamics* (CFD) simulations performed for the development of these devices. The second part of this chapter, instead, is devoted to the development of permanent magnetic dipoles. As we discussed in Chapter 2, where we detailed the diagnostics employed in this thesis, the main component of the electron spectrometer is the magnetic dipole, deflecting the electrons on a scintillator. Lastly, we conclude this chapter proposing a novel device that represents an advancement over current spectrometry techniques.

Contents

3.1	Development of Gas Targets	60
3.1.1	Fundamentals of Supersonic Nozzles	60
3.1.2	Computational Fluid Dynamics of Supersonic Nozzles	62
3.2	Development of Magnetic Dipoles	65
3.2.1	Magnetic dipole for few-MeV electrons	65
3.2.2	Spectrometer for few-MeV Highly-Divergent Electrons	66
3.3	Conclusion	69

3.1 Development of Gas Targets

In this section, we wish to present the supersonic nozzles developed for the experimental activities conducted in this thesis. These devices are commonly used for the production of laser-plasma accelerated electrons through the generation of high plasma density gradients (Semushin and Malka, 2001, Schmid and Veisz, 2012). As outlined earlier, our research aims at producing highly charged and low energetic electron beams. Hence, to meet these requirements, we attempted to develop supersonic gas jets able to reach densities exceeding $10^{19} - 10^{20} \text{ cm}^{-3}$. Such high densities have been proven promising for the production of beam charges above 10 nC (Feng et al., 2023). Moreover, we also put our efforts into developing sub-millimetric nozzles, to limit the amount of gas injected in the experimental chamber while reaching high plasma densities. Effective control over gas injection is crucial for applications demanding high repetition rates. Nonetheless, producing sub-millimetric nozzles represents a real technological challenge. Thanks to a technique called *Femtosecond Laser-assisted Selective Etching* (FLSE) (Tomkus et al., 2018) it has been possible to produce such gas jets in collaboration with the *Center for Physical Sciences and Technology* (FTMC) in Lithuania.

3.1.1 Fundamentals of Supersonic Nozzles

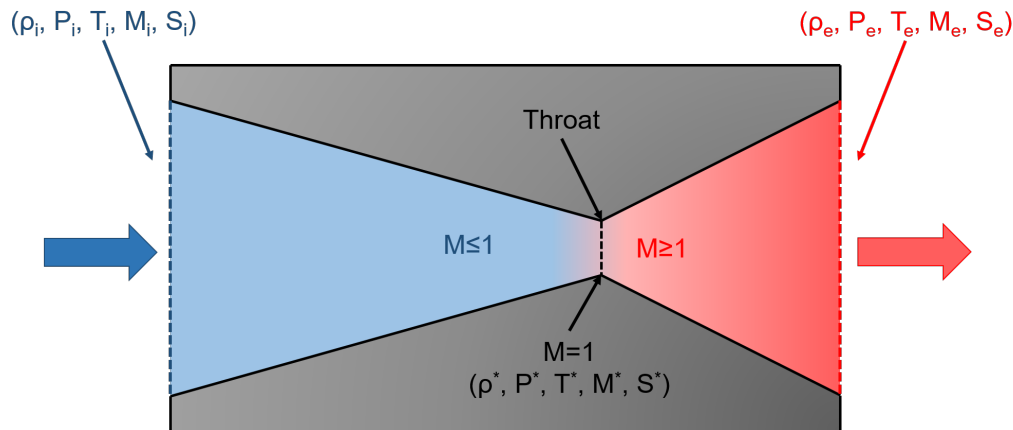


Figure 3.1: Schematic representation of a supersonic nozzle. Here, the fluid moves from left to right, following the arrows' direction.

A supersonic nozzle consists of a convergent-divergent tube, as shown in Fig. 3.1. To provide a simple description, we suppose that a homogeneous, isotropic and perfect gas propagates in the arrows' direction. Hence, it is possible to fully

describe its state using the temperature T (K), the pressure P (Pa), the density ρ (kg cm^{-3}) and the Mach number $M = v/a$ as variables. Here, v is the fluid velocity and

$$a = \sqrt{\kappa RT} = \sqrt{c_p(\kappa - 1)T} \quad (3.1)$$

represents the sound velocity of a perfect gas. In Eq. (3.1), R (J/kg K) is the specific gas constant, while $\kappa = c_p/c_v$ represents the heat capacity ratio (or adiabatic index). This ratio ranges between 1.3 and 1.6, depending on the type of gas. For pure nitrogen, for instance, $\kappa \sim 1.4$. Lastly, we assume the flow to be adiabatic and isentropic, allowing us to write the following differential equations describing the 1D gas flow in a supersonic nozzle (Zucker and Biblarz, 2019)

$$\frac{d\rho}{\rho} = -\frac{dv}{v} - \frac{dS}{S}, \quad \text{Mass continuity} \quad (3.2)$$

$$SdP = -(S\rho v)dv, \quad \text{Momentum continuity} \quad (3.3)$$

$$\frac{dP}{d\rho} = a^2. \quad \text{Isentropic transformation} \quad (3.4)$$

Here, S represents the nozzle cross-section in a generic position along the fluid propagation. Combining now Eqs. (3.3) and (3.4) reads

$$\frac{d\rho}{\rho} = -M^2 \frac{dv}{v}. \quad (3.5)$$

Hence, from Eq. (3.5) we conclude that for $M \ll 1$ the flow is almost incompressible: a relative variation of the velocity is much bigger than the variation of the density. Instead, for significant Mach numbers (i.e., $M \gtrsim 0.3$) the flow is considered compressible and when $M = 1$ the flow is said to be sonic (or critical). This condition is reached at the *throat* of the nozzle, as shown in Fig. 3.1. Now, from Eqs. (3.2) and (3.5) we can write

$$\frac{dS}{S} = (M^2 - 1) \frac{dM}{M} \quad (3.6)$$

and notice that for a subsonic flow (i.e., $M < 1$) the flow velocity increases with a decreasing cross-section. For a supersonic flow (i.e., $M > 1$), instead, an increase in the cross-section yields an increase in the gas velocity. Therefore, Eq. (3.6) describes the fundamental effect that causes a continuous gas acceleration throughout the supersonic nozzle of Fig. 3.1. Coherently with Fig. 3.1, we now identify the flow state at the entrance, throat and exit of the nozzle as (ρ_i, P_i, T_i, M_i) , (ρ^*, P^*, T^*, M^*) and (ρ_e, P_e, T_e, M_e) respectively. Moreover, the cross-sections at these positions are accordingly defined as S_i , S^* and S_e . Therefore, it is

possible to write the following equations that describe the flow evolution, under the assumptions previously discussed (Schmid et al., 2010b)

$$\frac{S_e}{S^*} = \frac{1}{M_e} \left(1 + \frac{\kappa - 1}{\kappa + 1} (M_e^2 - 1) \right)^{\frac{\kappa + 1}{2(\kappa - 1)}}. \quad (3.7)$$

Eq. (3.7) underlines the importance of the ratio S_e/S^* : changing its value allows to regulate the exit Mach number M_e , as shown in Fig. 3.2. Here, we show the exit Mach number as a function of the ratio S_e/S^* for pure nitrogen ($\kappa = 1.4$) and for monoatomic gases ($\kappa = 5/3$) for comparison.

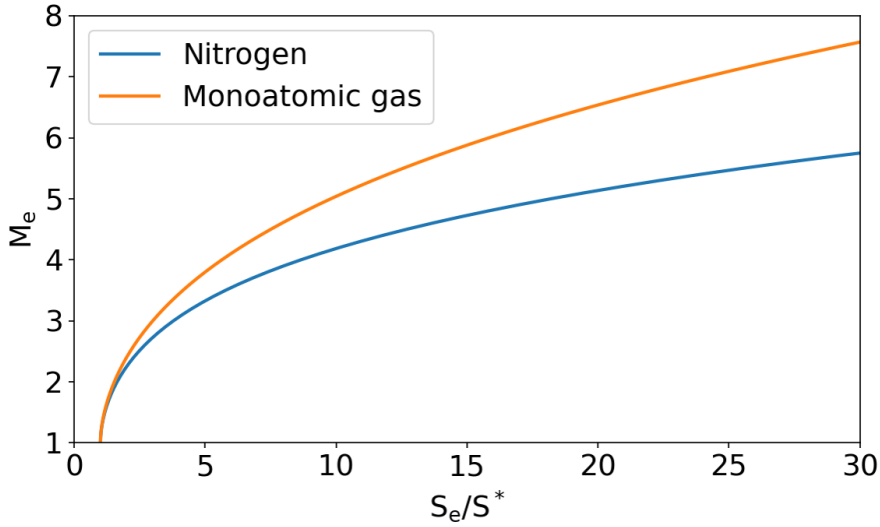


Figure 3.2: Exit Mach number (M_e) as a function of the ratio S_e/S^* for nitrogen and monoatomic gases.

3.1.2 Computational Fluid Dynamics of Supersonic Nozzles

In order to develop gas targets, we performed 2D simulations with ANSYS Fluent. This software allows to solve Navier-Stokes equations and thus to predict the gas flow parameter. In this section, we focus on the development of the nozzle in Fig. 3.3 that we employed for the experiment presented in Chapter 4.

Coherent with the experiment presented in this work, we have employed pure nitrogen for the numerical simulations. In Fig. 3.4 we present an example of the results we obtained with ANSYS Fluent. Here, we have simulated a cylindrically

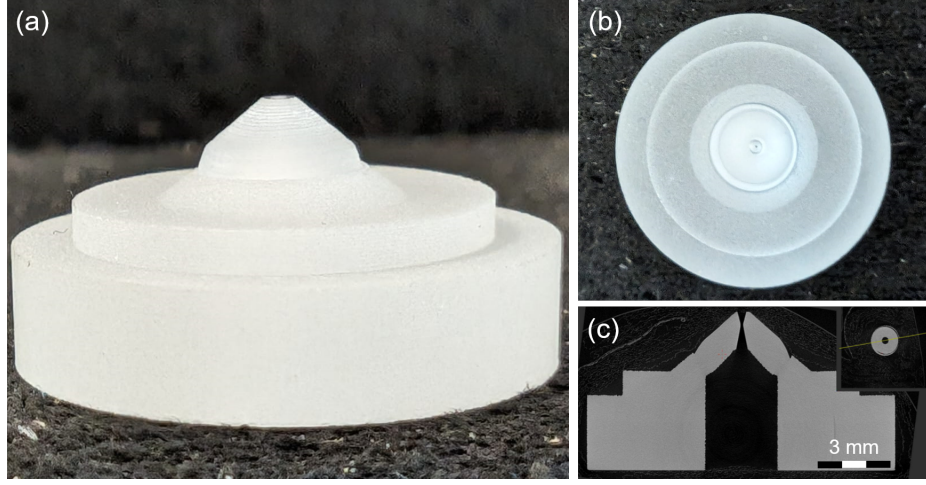


Figure 3.3: (a) Side and (b) top view of the glass nozzle we developed. (c) Example of glass nozzle tomography. Here, we can observe the inner structure at the middle plane.

symmetric nozzle in conditions similar to the experimental configuration. Nitrogen flows across the solenoid valve with an inlet pressure $P = 70$ bar and it is injected in a 3 mm diameter reservoir at the nozzle entrance. Subsequently, it reaches the nozzle throat that measures 0.1 mm in diameter and the flow reaches a Mach number $M \approx 1$. The gas crosses the exit diameter of 0.4 mm and it expands in vacuum (i.e., $P = 0$ bar), where we estimate $M \approx 4$, which is in agreement with Eq. (3.7).

In Fig. 3.5 we present the numerical estimation of plasma density profiles along the radius r defined in Fig. 3.5. Each profile is at a different height from the nozzle exit and they have been deduced from nitrogen density profiles, assuming a complete L-shell ionization. Specifically, for a given nitrogen density ρ_{N_2} we write

$$n_e(\text{cm}^{-3}) = \frac{D_{ion} N_A \rho_{N_2}(\text{kg/m}^3)}{M_{N_2}(\text{kg/kmol})} 10^{-3}, \quad (3.8)$$

where N_A is Avogadro's number, $M_{N_2} = 28$ kg/kmol is nitrogen's molecular mass and D_{ion} is nitrogen ionization degree. Since we are assuming a full L-shell ionization $D_{ion} = 10$. From Eq. (3.8) we yield

$$n_e(\text{cm}^{-3}) = 2.15 \times 10^{20} \rho_{N_2}(\text{kg/m}^3) \quad (3.9)$$

The peak values in Fig. 3.5 prove the potential of this design, allowing to exceed 10^{20} cm^{-3} with a sub-millimeter nozzle.

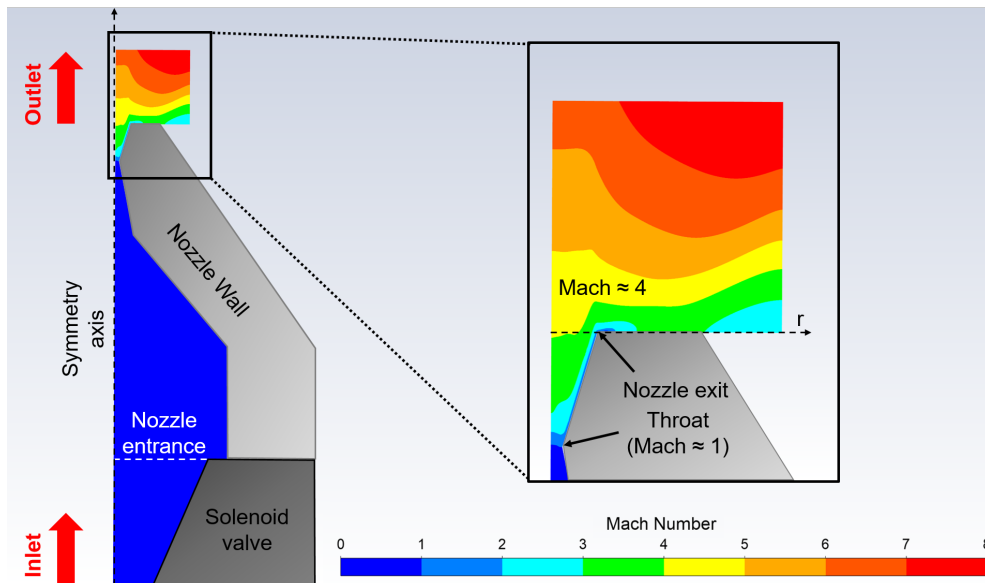


Figure 3.4: 2D-axisymmetric ANSYS Fluent simulation result. Here, the colormap represents the Mach number inside the supersonic nozzle. Further details about the simulation are provided in the text.

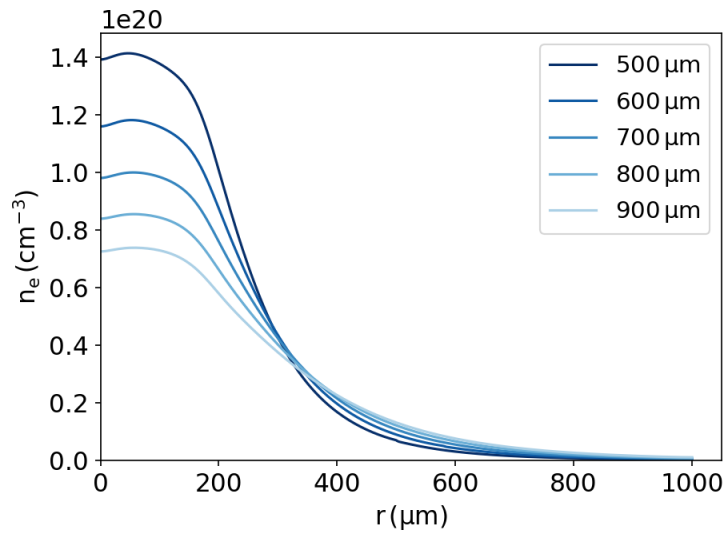


Figure 3.5: Estimated plasma density profiles along the radius r and at different heights from the nozzle exit.

3.2 Development of Magnetic Dipoles

3.2.1 Magnetic dipole for few-MeV electrons

The magnetic dipole is an essential component of the spectrometry technique we have presented in the previous chapter. Its magnetic field intensity needs to be carefully chosen in order to properly deflect the electrons of interest on the scintillating screen. Here, we wish to briefly present the device used for the experiment of Chapter 4. In Fig. 3.6(a) we show the actual dipole, where it is

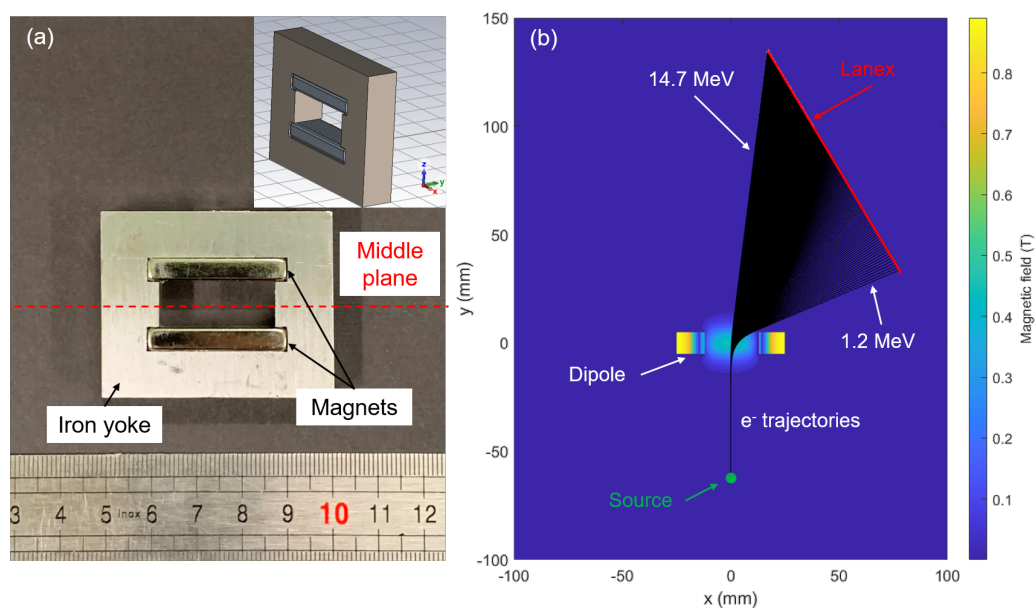


Figure 3.6: (a) The permanent dipole used for the experiments discussed in chapter 4. In the inset, we show a view of the magnetic study conducted with CST Studio Suite, necessary for the dipole development. (b) Particle tracking simulation performed using the dipole middle plane magnetic field map. In this simulation, we have initialized five hundred electrons at 6 cm from the dipole, with energies between 1.2 MeV and 14.7 MeV.

possible to distinguish the two NdFeB magnets kept at 1 cm distance thanks to the iron (Fe99) yoke. The whole device measures $10 \times 40 \times 50 \text{ mm}^3$ in volume, making it extremely light and compact and thus easy to operate with motorized stages during the experiments. The magnets present a remanence magnetic field $B_{rem} \sim 1.3 \text{ T}$, while we numerically estimate the yoke relative magnetic permeability to be $\mu_r \gtrsim 1000$. The dipole has been developed through an iterative numerical study using the CST Studio Suite (inset of Fig. 3.6(a)). This software allows to perform

magnetostatic simulations, solving Maxwell's equations through the finite volume method. Hence, it was then possible to retrieve the magnetic field map that was subsequently used to estimate the electrons' deflection on the Lanex screen and, thus, to validate the dipole design. This operation is carried out using Matlab scripts specifically developed for particle tracking, as shown, for instance, in Fig. 3.6(b). In this figure, it is possible to observe the magnetic field map obtained at the dipole middle plane via CST Studio Suite. Here, the maximum field strength is estimated to be ~ 0.45 T, which agrees with the actual dipole field measured at the same point using a Brockhaus Messtechnik 421 Gaussmeter (LakeShore, 2004). Furthermore, in Fig. 3.6(b) we display five hundred electrons' trajectories (black lines), with energy between 1.2 MeV and 14.7 MeV, initialized at 6 cm from the dipole entrance (i.e., as for the configuration presented in Section 2.3.1). Thanks to this simulation, it has been possible to retrieve the curves shown in Fig. 2.4(b) and thus determine the spectrometer calibration and resolution.

3.2.2 Spectrometer for few-MeV Highly-Divergent Electrons

The system we have described in the Section 3.2.1 presents some limitations. The relative position between the dipole and the scintillating screen is fundamental for the spectrometer calibration. Nonetheless, the system we previously described requires a manual adjustment of the Lanex screen, potentially leading to a large systematic error. Moreover, the dipole of Fig. 3.6(a) necessarily needs a pinhole at its entrance. The pinhole reduces the electron beam size, improving the overall spectrometer resolution and preventing the electrons' trajectories from mixing up. Indeed, in the presence of highly divergent beams, electrons with the same energy could find themselves at different positions at the dipole's entrance. This, in turn, would inevitably cause these electrons to land at different positions on the scintillator, as shown in Fig. 3.7. Here, we see two distinct cases, both representing the trajectories of two electrons (discontinuous lines) produced with a source at a given position from a Lanex screen. The electrons have energies $E_1 = E_2$ and they propagate under the effect of a magnetic field B_z , entering the page plane. The case displayed in Fig. 3.7(a) shows that if the electrons enter the magnetic field at two different positions, they are inevitably collected at two different positions s_1 and s_2 on the Lanex screen. As displayed in Fig. 3.7(b), a pinhole can easily mitigate this effect, ensuring a proper spectrum reconstruction: the electrons having the same energy enter the magnetic field at virtually the same position, allowing them to land at $s_1 \approx s_2$. However, while this configuration enhances spectrum reconstruction precision, it limits the ability to measure electron energies significantly displaced from the central axis. To overcome this limitation, horizontal and vertical motorization of the spectrometer becomes necessary, similar to what

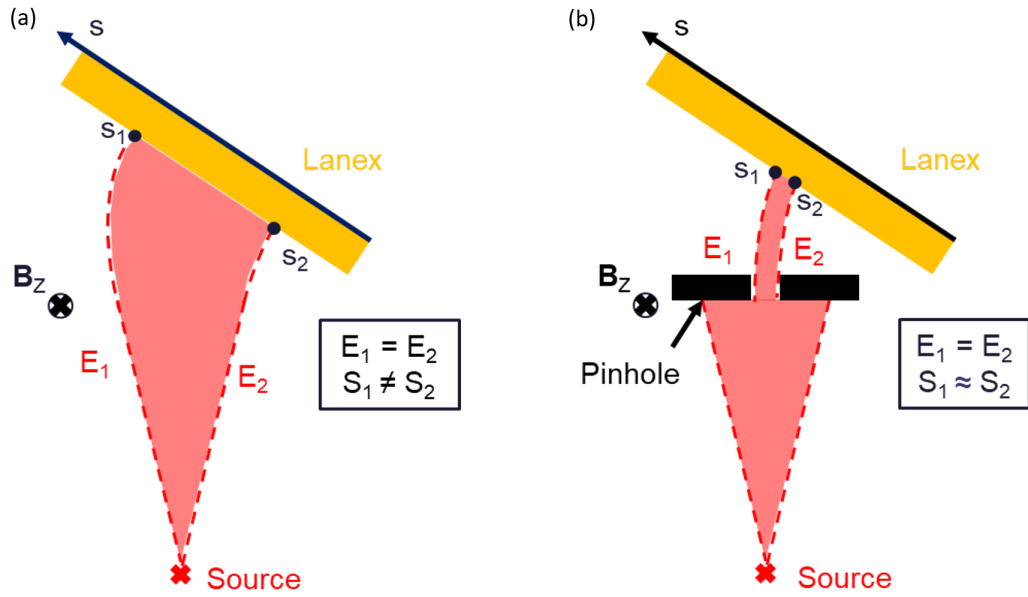


Figure 3.7: Schematic representations on the role of a pinhole. (a) Case without the pinhole. Here, two electrons with energies $E_1 = E_2$ interact with the Lanex at two different positions s_1 and s_2 . (b) Introducing a pinhole makes sure that the electrons enter the magnetic field at the same position. This allows them to land at $s_1 \approx s_2$ on the Lanex.

we discuss in Chapter 4.

We now intend to propose a new spectrometer that tackles the issues we just mentioned. Fig. 3.8(a) illustrates a picture of the prototype we have developed in collaboration with Vacuumschmelze. This spectrometer measures 28 cm in length and 17 cm in width and it consists of a magnetic dipole with an 11 cm air-gap. Each pole is composed of nine magnets with a remanence magnetic field $B_{rem} \sim 1.1$ T developed by Vacuumschmelze. From these pictures, it is also possible to notice that the dipole is open on one side. Here, two Lanex screens can be directly fixed on the dipole iron yoke. This allows to secure the relative position between the dipole and the scintillators, drastically reducing the error introduced by the manual adjustment of the two. Fig. 3.9(a) presents the magnetic field measured at the middle plane of the dipole, using the Brockhaus Messtechnik 421 Gaussmeter. Fig. 3.9(b) and (c) refer to the measured magnetic field along the axes x^* and y^* , defined in Fig. 3.9(a). Fig. 3.9(b) and (c) also present the magnetic field profiles obtained through a CST numerical study. Hence, we notice the good agreement between the measured and simulated magnetic fields. In order to illustrate the working principle of this system, in Fig. 3.10 we show the results obtained with

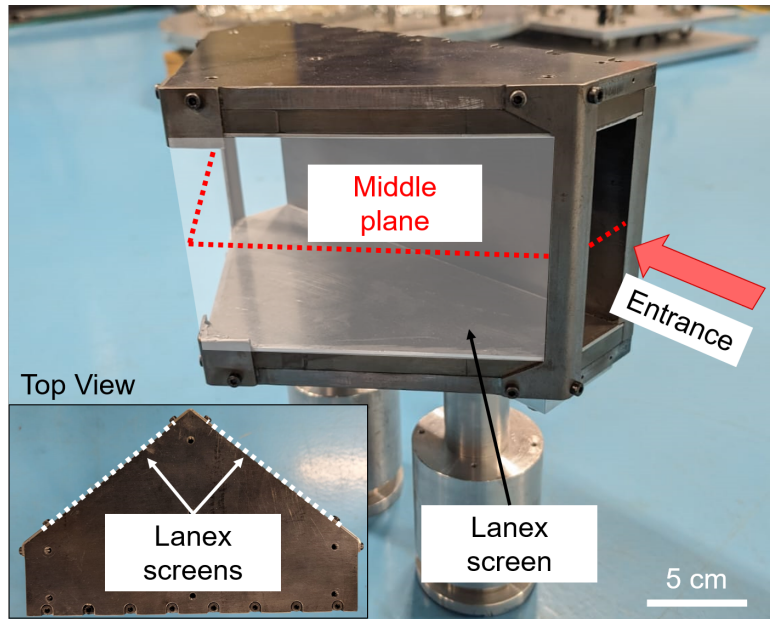


Figure 3.8: Novel electron spectrometer prototype. Here, we underline the dipole entrance and the position of the two Lanex screens. In the inset we present a top view of the system.

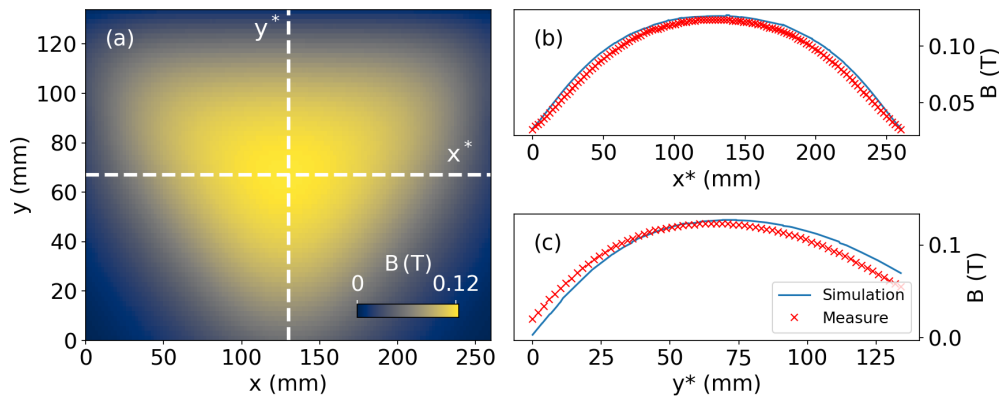


Figure 3.9: (a) Magnetic field map measured at the dipole middle plane. (b) Measured and simulated magnetic field profiles along the x^* and y^* axes.

a CST particle tracking simulation. Here, we consider an electron source at 2 cm from the dipole's entrance, where we assume a rectangular slit 0.2 mm wide and of 2 cm in height. Using a slit instead of a pinhole presents a clear advantage: a slit still hinders the electrons' trajectories mix-up while allowing to sample a bigger portion of the incoming beam. Specifically, this allows to measure eventual

energy dependencies on the beam divergence. In Fig. 3.10 it is possible to see the trajectories obtained with a 0.5 MeV electron beam and a maximum divergence of 400 mrad. Here, we notice that, despite their divergence, the electrons can easily propagate inside the dipole, until interacting with the Lanex screen. The inset of Fig. 3.10 shows a top view of the spectrometer. Here, we display the trajectories of electrons with energies between 0.5 MeV to 20 MeV. This demonstrates the wider energy range that this spectrometer allows to study compared to the previous system.

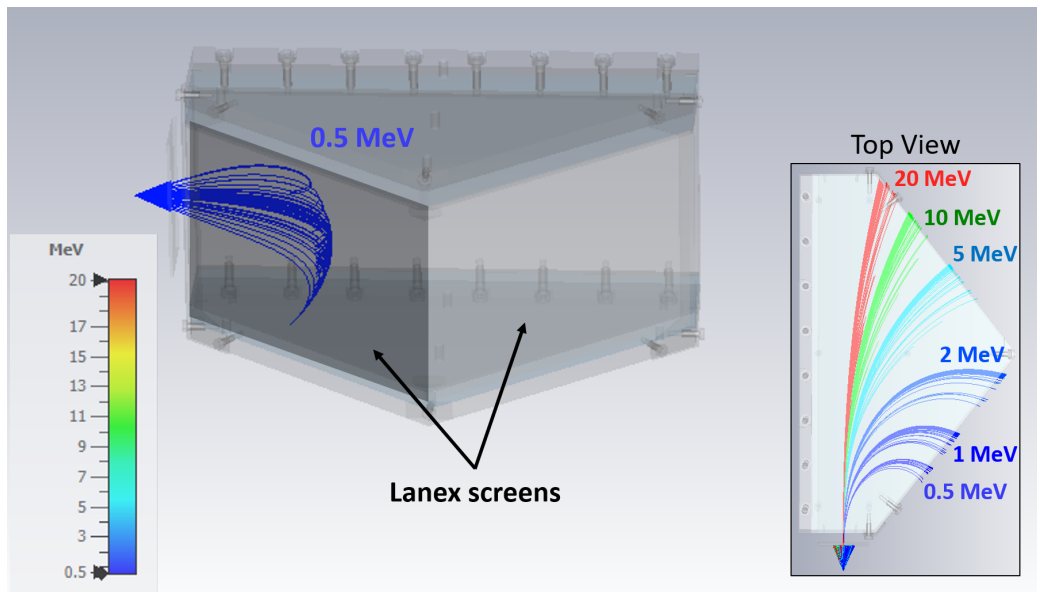


Figure 3.10: CST particle tracking results. (a) Results pertaining a 0.5 MeV, 400 mrad electron beam. (b) Results considering electrons between 0.5 MeV and 20 MeV with a maximum divergence of 400 mrad.

3.3 Conclusion

The chapter illustrates the development of tools necessary for our research. After a brief overview of the physics of supersonic nozzles, we outlined the steps for developing these devices, employing the commercial software ANSYS Fluent. Here, we showed the design of a sub-millimetric nozzle able to reach plasma densities above 10^{20} cm^{-3} , which are promising for the production of highly-charged electron beams. The gas jet has been realized in glass at the *Center for Physical Sciences and Technology* (FTMC) in Lithuania. Subsequently, we have explored the development of one magnetic dipole, an essential component for

electron spectrometry. Thus, we design a device able to deflect electrons with energies between 1.2 MeV to 14.7 MeV. In Chapter 4 we will illustrate how we employed both the gas target and the magnetic dipole to carry out the experiment. After presenting the limitations of the spectrometry technique employed in this work, we concluded this chapter by proposing a novel spectrometer, specifically developed to overcome these constraints. This device will be tested and used in future experiments involving few-MeV, highly divergent electron beams.

Chapter 4

Production of few-MeV Highly-Charged Beams

The chapter is devoted to the experimental campaign of this work, conducted in LOA's Salle Jaune, where we aimed at generating the highest possible charge at just a few-MeV. As previously discussed, the efficient generation of high charges paves the way to reaching high average beam currents. Thus, we begin by presenting the experimental setup, recalling the main diagnostics employed. Subsequently, we discuss in detail the results we obtained, with particular care to the charge-per-Joule, allowing us to easily gauge the efficiency in generating highly-charged electron beams. We conclude this chapter with a brief discussion on the potential of this electron source for few-MeV applications. A more in-depth interpretation of these results is presented in Chapter 5, where we use PIC simulations to describe the underlying physics.

Contents

4.1	Experimental Setup	72
4.2	Experimental Results	75
4.2.1	Laser and Gas Targets Characterization	75
4.2.2	Electron Beam Charge-per-Joule	78
4.2.3	Electron Beam Energy Spectrum and Divergence	81
4.2.4	Electron Beam Dose	85
4.3	Conclusion	87

4.1 Experimental Setup

In Fig. 4.1(a) we show a simplified setup of the experiment, where we illustrate the trajectory of both the driver and pump laser. Both beams are produced using the Ti:Sapphire Salle Jaune laser system, able to deliver 808 nm, 30 fs pulses, as illustrated in Section 2.2. We estimate the driver and probe beams to reach the experimental chamber with a maximum energy of 1.7 J and 0.1 J respectively. The driver initially has a 100 mm diameter and it is focused on the gas jet with a 120 mm diameter metallic Off-Axis Parabola (OAP). For this experiment, we have employed two distinct OAPs produced by Kirchheim Optics, with focal lengths of $f = 400$ mm and $f = 800$ mm, corresponding to $f/4$ and $f/8$ respectively. The OAP is motorized, allowing to perform a refined alignment while the chamber is under vacuum. The probe beam, instead, has a 30 mm diameter and it reaches the gas jet at the same time as the driver beam. In Fig. 4.1(a) we clearly notice that the probe beam reaches the gas jet perpendicularly to the driver's trajectory. Subsequently, it is collected with a Phasix SID4 Camera, allowing for plasma density measurements, as we discussed in Section 2.3.3. Fig. 4.1(a) also highlights the setup of one major diagnostics: the Beam Profile Monitor (BPM), presented in Section 2.3.2. Here, we simply recall that the BPM is composed of a ~ 75 mm diameter scintillator, motorized with a 100 mm stage, thus allowing us to easily position it to collect the produced electron beams within a specific solid angle. During the experiment presented in this chapter, we moved the BPM at 80 mm and 130 mm from the nozzle, corresponding to a solid angle of around 0.5 sr and 0.25 sr respectively. Fig. 4.1(b), instead, displays another relevant diagnostic: the electron spectrometer, illustrated in Section 2.2. This device is positioned at 60 mm from the source and we placed a 2 mm diameter pinhole in front of it to select a small sample of the electron beam. The electron spectrometer was horizontally motorized using a 150 mm stage, allowing us to move it on the laser axis and perform the energy measurements.

Fig. 4.2(a) depicts a picture of the actual experimental chamber, which measures 1020 mm in diameter and, when no gas is injected, the chamber is at a vacuum pressure of approximately 10^{-4} mbar. In Fig. 4.2(a) we only present the trajectory of the driver beam in red for visual purposes. Furthermore, in this picture we highlight two foldable aluminum pipes, holding the two Lanex screens used for the BPM and electron spectrometer. These pipes allow for the motorization of the two diagnostics, while suppressing any parasitic light that might be collected by the CCD cameras in Fig. 4.1. In Fig. 4.2(b) we present a close-up of the two main diagnostics. Specifically, in this picture the BPM is retracted, allowing for the electron spectrometer to be aligned with respect to the driver beam axis.

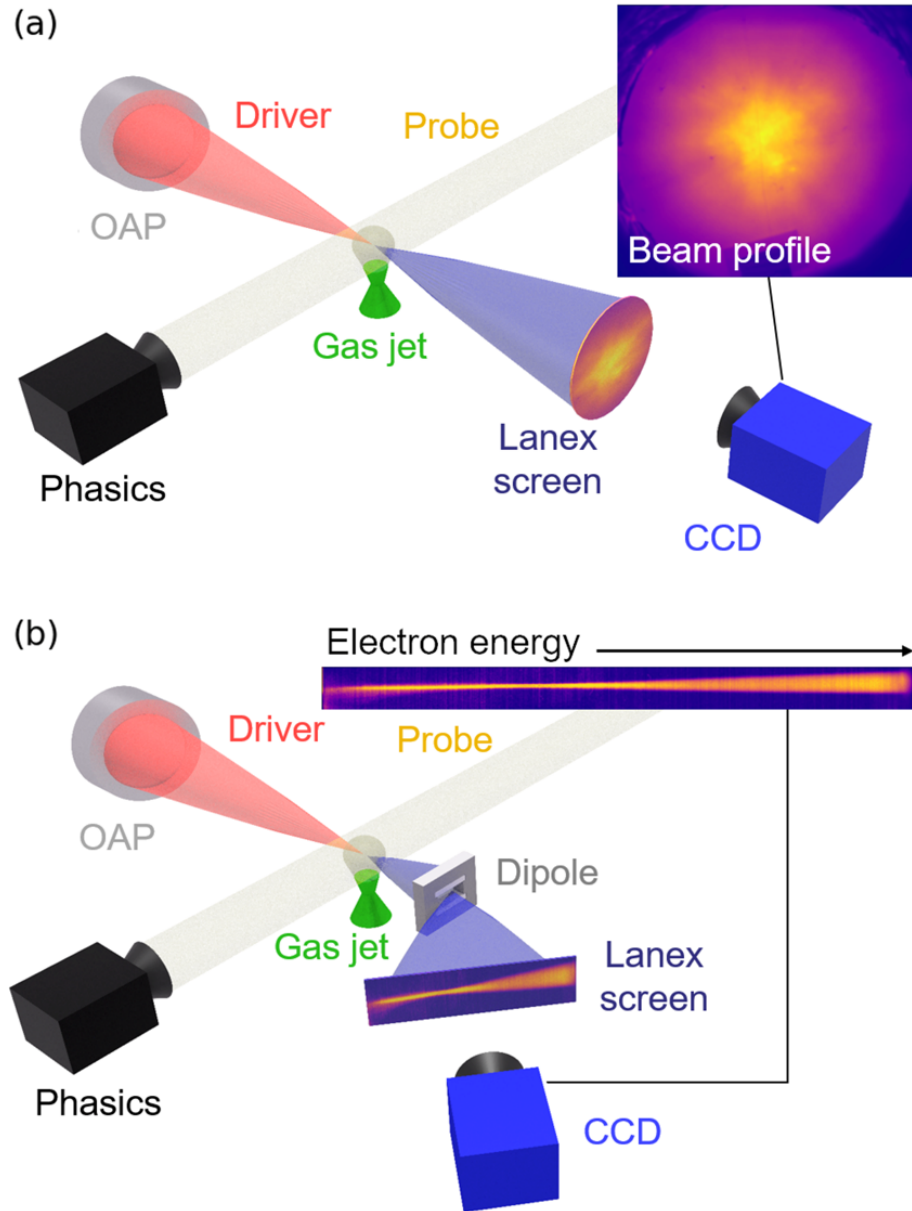


Figure 4.1: Simplified experimental setup, displaying the (a) beam profile monitor, allowing for beam charge and divergence measurements. (b) Setup for the electron spectrometer, which can be positioned on the laser axis using motorized stages, once the beam profile monitor has been removed. Here, we also notice the probe beam, used to perform plasma density or gas density measurements with a Phasics SID4 Camera.

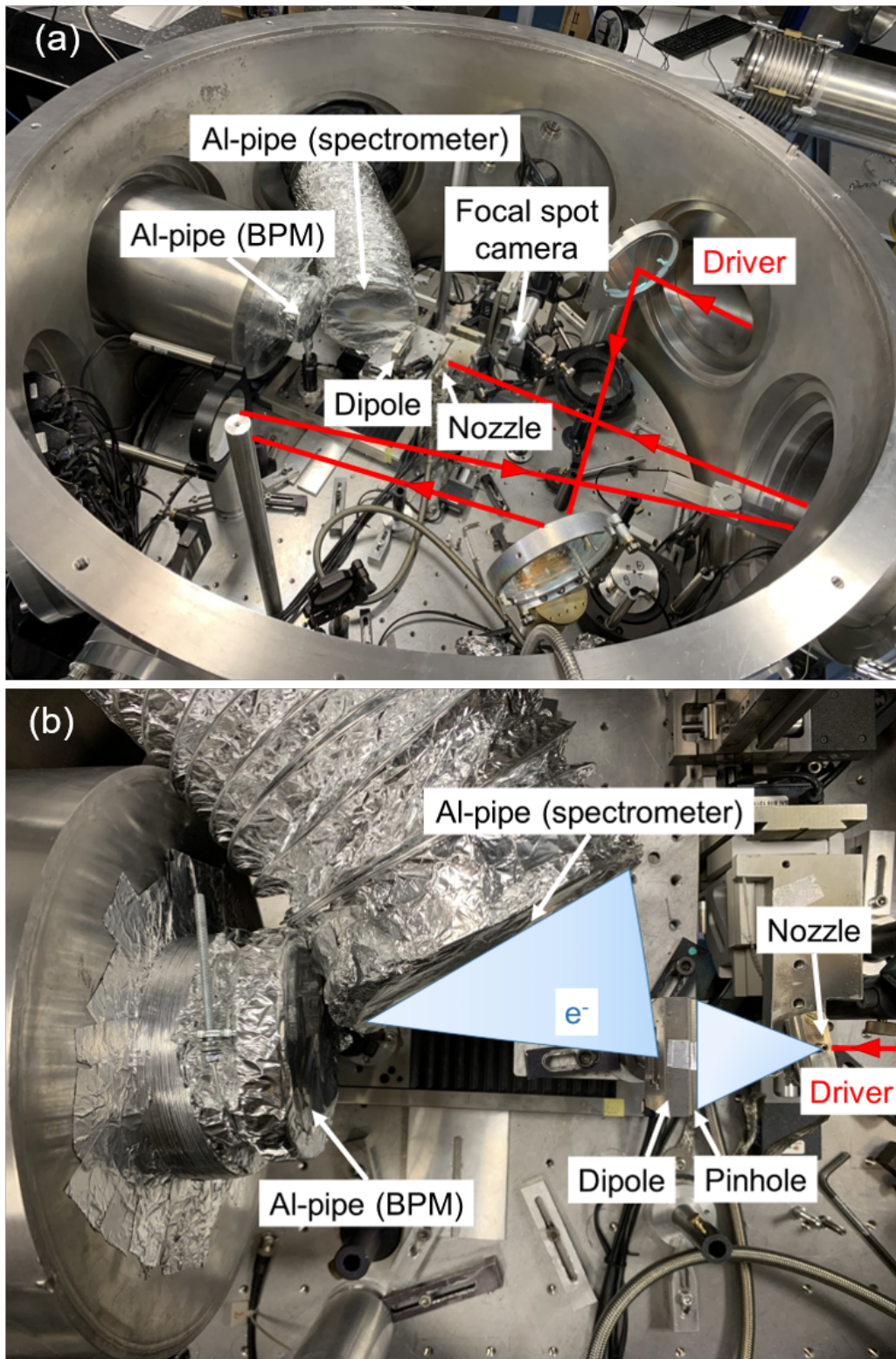


Figure 4.2: (a) Experimental chamber and main diagnostics. We only show the driver path for visual purposes. (b) Close-up of the BPM and electron spectrometer.

4.2 Experimental Results

4.2.1 Laser and Gas Targets Characterization

Before exploring the main results, we wish to briefly discuss the measurements concerning the laser and the gas target. This, in turn, will allow to better understand the configurations employed for the experimental campaign and also to identify the laser-plasma interaction regime under investigation.

Laser Characterization

Using the focal spot camera (see Section 2.3.4), we were able to obtain the image depicted in Fig. 4.3 after a background subtraction. Here, we show the laser at the focal spot, focused using the f/4 parabola. This image allows us to estimate the laser Full Width at Half Maximum (FWHM) diameter $d \approx 5 \mu\text{m}$ and also to evaluate the laser energy percentage within the first-zero radius spot, as underlined by the dashed circle in Fig. 4.3. This accounts for approximately 57% of the total energy. We now define the maximum effective laser energy as the energy within this radius spot, which amounts to around $E_L = 0.97 \pm 0.1 \text{ J}$. The error on the laser

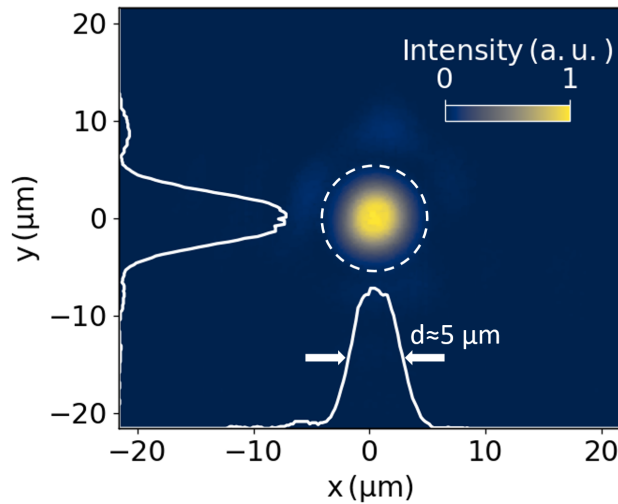


Figure 4.3: Laser focal spot obtained with the f/4 OAP. The white curves represent the profiles through the laser intensity peak and d is the FWHM diameter. The dashed circle delineates the region considered for calculating the energy within the central spot

energy is defined performing different background subtractions and estimating the corresponding Root-Mean-Square Error (RMSE). From the image in Fig. 4.3 we also estimate the laser peak intensity to be around $I_0 = 1.5 \times 10^{20} \text{ W cm}^{-2}$ and from Eq. (1.51) it is straightforward to yield the maximum normalized vector potential in vacuum, namely $a_0 \approx 8.5$. Similarly, with the $f/8$ OAP we estimate a FWHM diameter $d \approx 11.6 \mu\text{m}$, with a maximum energy $E_L = 1 \pm 0.1 \text{ J}$ inside the first-zero radius spot. Thus, we estimate a peak intensity $I_0 = 3.4 \times 10^{19} \text{ W cm}^{-2}$ and the corresponding normalized vector potential is $a_0 \approx 4$.

Gas Nozzles Characterization

Using the Phasics SID4 Camera we performed a gas target characterization at the nozzle backing pressures used for the electron beam generation. In Fig. 4.4(a) we show an example of plasma density measurement, using the 0.4 mm exit diameter glass nozzle we developed (see Section 3.1.2). This plasma density map was generated by ionizing pure nitrogen with a 10 mJ laser pulse that propagates from the left-hand side of Fig. 4.4(a), hence reproducing the experimental conditions we will discuss in the following. The laser axis is represented by the dashed white line, which is at $\sim 500 \mu\text{m}$ from the nozzle exit at $y = 0$. The nozzle is horizontally centered at $x = 0$. In this case, the backing pressure was set to 10 bar and it allowed us to reach a peak plasma density around $1.2 \pm 0.18 \times 10^{19} \text{ cm}^{-3}$, as shown in Fig. 4.4(b). Here, we illustrate the plasma density longitudinal profile corresponding to the laser axis in Fig. 4.4(a). The relative error bar defined in

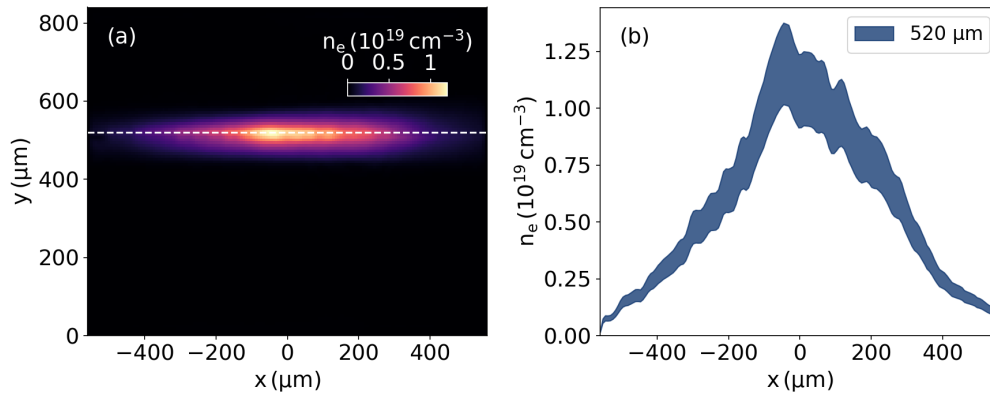


Figure 4.4: (a) Plasma density map obtained with the 0.4 mm exit diameter glass nozzle and a 10 bar backing pressure. The nozzle center is at $x = 0$ and its exit is at $y = 0$. (b) Plasma density profile measured across the white dashed line in (a), namely at $\sim 500 \mu\text{m}$ from the nozzle exit.

this figure was calculated from an estimated $\sim 15\%$ systematic error on the peak plasma density. With an 80 bar backing pressure, instead, we obtain the density map depicted in Fig. 4.5(a), obtained from the direct measurement of a pure nitrogen jet and assuming a total L-shell ionization. The light blue curve in Fig. 4.5(b) represents the density profile recorded at $\sim 500\ \mu\text{m}$ from the nozzle. To further validate this density measurement, we have performed a linear extrapolation from the curve obtained at 10 bar in Fig. 4.5(b). Since the backing pressure in this case is eight times that of the previous example, this extrapolation, represented by the dark blue curve in Fig. 4.5(b), was derived by scaling the 10 bar profile by a factor of eight. Thus, we notice the good agreement of the two curves and with this nozzle we estimate a peak plasma density of $9.6 \pm 1.9 \times 10^{19}\ \text{cm}^{-3}$. Performing a similar scaling, we estimate the plasma density at 30 bar, 60 bar, 70 bar and 80 bar to be $3.6 \pm 0.54 \times 10^{19}\ \text{cm}^{-3}$, $7.2 \pm 1.1 \times 10^{19}\ \text{cm}^{-3}$, $8.4 \pm 1.26 \times 10^{19}\ \text{cm}^{-3}$ and $9.5 \pm 1.45 \times 10^{19}\ \text{cm}^{-3}$ respectively.

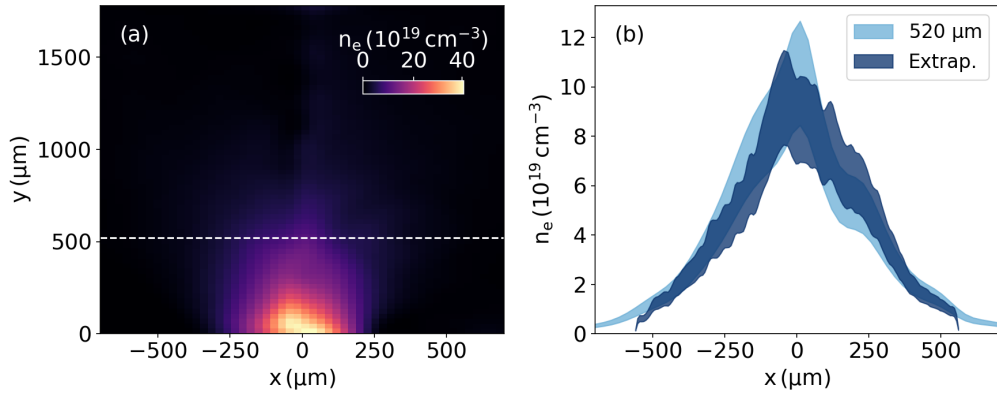


Figure 4.5: (a) Density map obtained with the 0.4 mm exit diameter nozzle at 80 bar. In this case, the density is retrieved assuming a full nitrogen L-shell ionization. (b) The light blue curve is the density profile measured across the white dashed line in (a), while the dark blue profile was extrapolated scaling the profile in Fig. 4.4(b) by a factor of eight.

Lastly, Fig. 4.6(a) depicts an example of density estimate with a 2 mm exit diameter metallic supersonic nozzle and a 60 bar backing pressure. This gas target was used along with the 0.4 mm nozzle for the experimental campaign, as it will be discussed later in the chapter. Similarly to the previous example, we deduce the plasma density from a direct measurement of a neutral nitrogen jet. During the experiment, we shot the driver laser at 1 mm and 2 mm from the nozzle exit. Thus, in Fig. 4.6(b) we present two density profiles for these two different vertical positions. Under these conditions, we estimate a peak plasma density of

$7.5 \pm 1.1 \times 10^{20} \text{cm}^{-3}$ and $3.8 \pm 0.52 \times 10^{20} \text{cm}^{-3}$ at 1 mm and 2 mm from the nozzle exit respectively. To get the plasma density at 80 bar, we simply scale these values by a factor of 1.3 and we obtain $10 \pm 1.5 \times 10^{20} \text{cm}^{-3}$ and $5.06 \pm 0.69 \times 10^{20} \text{cm}^{-3}$.

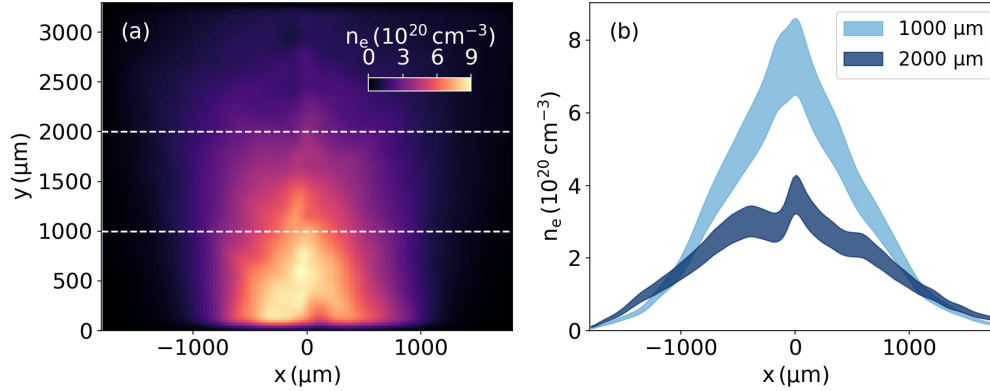


Figure 4.6: (a) Density map obtained with a 2 mm exit diameter metallic nozzle at 60 bar. (b) Density profiles measured across the white dashed lines in (a), namely at 1 mm and 2 mm from the nozzle exit.

4.2.2 Electron Beam Charge-per-Joule

During the experimental campaign, we examined different configurations, changing the laser energy, the plasma density and the OAP for two different nozzles. Our specific interest was to study how efficiently we could exploit the laser energy to produce beam charge in each configuration. As previously mentioned, we have introduced the charge-per-Joule metric to estimate the efficiency of each configuration. Compared to the conversion efficiency (η), defined as the ratio of the electron energy to the laser energy, the charge-per-Joule is easier to estimate, since it does not require the knowledge of the electron energy spectrum. Moreover, this parameter serves a practical purpose: by multiplying it by the laser average power, one can readily calculate the beam average current. In this section, we intend to present the main results pertaining the charge-per-Joule measurements. For completeness, we will also provide estimates of the conversion efficiency based on the energy spectra presented in the next section.

In Fig. 4.7(a) and (b) we illustrate the results obtained with the 0.4 mm and 2.0 mm nozzle respectively, with the f/4 OAP. For a proper interpretation of these curves, it is essential to note that the BPM was positioned at 130 mm from the

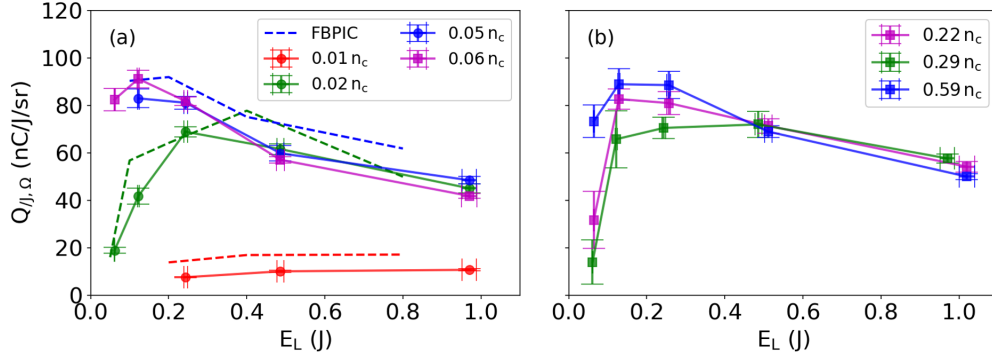


Figure 4.7: Charge-per-Joule in a given solid angle ($Q_{J,\Omega}$) produced with the f/4 OAP. (a) Results obtained with the 0.4 mm nozzle for three different plasma densities and a 0.25 sr aperture. The curve at $n_e = 0.06 n_c$ was obtained with a 0.5 sr solid angle and the dashed curves refer to an FBPIC simulation set. (b) Results obtained with the 2 mm nozzle for three different plasma densities and a 0.5 sr aperture.

smaller nozzle and at 80 mm from the bigger nozzle, except the magenta curve in Fig. 4.7(a), for which the BPM was at 80 mm from the nozzle. Thus, we performed the charge measurements with two collecting angles (i.e., 0.25 sr and 0.5 sr). In Fig. 4.7(a) and (b) we display the charge-per-Joule-per-solid-angle ($Q_{J,\Omega}$), allowing for a better comparison between the different configurations. In the following, we will simply refer to $Q_{J,\Omega}$ as the charge-per-Joule. Each continuous curve refers to a different plasma density expressed in terms of the critical plasma density $n_c \approx 1.7 \times 10^{21} \text{ cm}^{-3}$ for $\lambda = 800 \text{ nm}$. Furthermore, the curves are plotted as a function of the estimated laser energy within the laser central spot, while the error bars represent the RMSE on ten consecutive shots. In Fig. 4.7(a) we present a set of FBPIC results (dashed curves), allowing to reproduce the charges-per-Joule obtained under the experimental conditions within the systematic error (i.e., $\sim 16\%$). These simulations are discussed in further detail in Section 5.3. In Fig. 4.7(a) we notice that the charge-per-Joule at $n_e = 0.01 n_c$ from 7.5 nC/J/sr at $E_L = 0.24 \text{ J}$ increases to around 10 nC/J/sr for $E_L = 0.48 \text{ J}$. At higher plasma densities, instead, we observe a stronger dependency on the laser energy. Specifically, for $n_e = 0.02 n_c$ the charge-per-Joule increases with the laser energy, until reaching $E_L > 0.24 \text{ J}$, where it reaches a maximum of $\sim 69 \text{ nC/J/sr}$ and subsequently starts to decrease. Similarly, the curves for $n_e = 0.05 n_c$ and $n_e = 0.06 n_c$ tend to decrease with the laser energy. We presume this is due to the limited BPM collecting angle. For $E_L > 0.24 \text{ J}$, an increase in laser energy produces more divergent electrons that are not captured by the

BPM. Consequently, this results in a decrease in charge-per-Joule. Moreover, the curves at $n_e > 0.02 n_c$ superimpose for $E_L > 0.24$ J, underlying a charge-per-Joule saturation effect, as we will discuss in further detail in the next chapter. With the 0.4 mm nozzle we measure a maximum charge-per-Joule of 91 nC/J/sr at $E_L = 0.12$ J and $n_e = 0.06 n_c$, corresponding to a charge of ~ 5.5 nC. In these conditions, we estimate a conversion efficiency $\eta = 13.1\%$. The 2 mm nozzle (Fig. 4.7(b)) displays similar tendencies to those measured with the 0.4 mm nozzle. In Fig. 4.7(b), the curve at $n_e = 0.29 n_c$ was obtained on a different day than those at $n_e = 0.22 n_c$ and $n_e = 0.59 n_c$, which can explain the slight difference in values. With the bigger nozzle, we reach up to 89 nC/J/sr with $n_e = 0.59 n_c$ at $E_L = 0.13$ J (i.e., 5.7 nC), corresponding to the maximum conversion efficiency we measured, namely $\eta = 14.4\%$. At full laser energy, instead, we reach close to 55 nC/J/sr with the three different densities, corresponding to the maximum charge we were able to measure, namely ~ 28 nC and in this case $\eta = 9.2\%$.

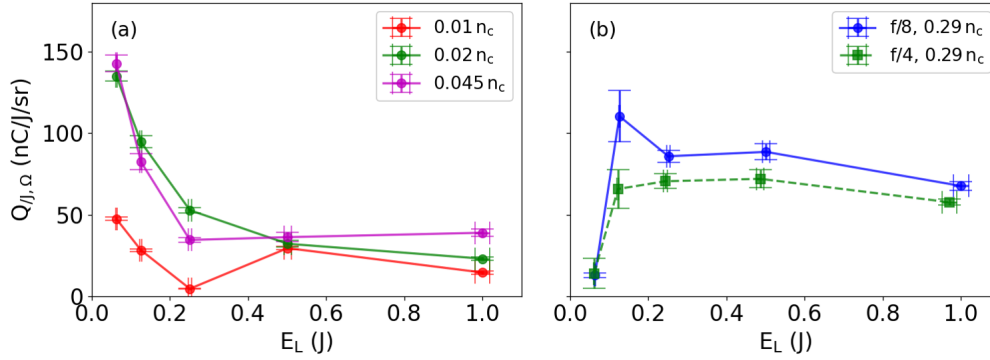


Figure 4.8: Charge-per-Joule in a given solid angle ($Q_{J,\Omega}$) produced with the f/8 OAP. (a) Results obtained with the 0.4 mm nozzle for three different plasma densities and a 0.25 sr aperture. (b) Results obtained with the 2 mm nozzle for $n_e = 0.29 n_c$. Here, we show the charge-per-Joule measure at $n_e = 0.29 n_c$ with the f/4 OAP for comparison in a 0.5 sr solid angle.

Fig. 4.8(a) and (b) illustrate the results obtained with the 0.4 mm and 2 mm nozzle respectively, using the f/8 OAP. Specifically, in Fig. 4.8(a) we notice that the curves at $n_e = 0.02 n_c$ and $n_e = 0.045 n_c$ superimpose, highlighting a saturation effect, similar to the f/4 OAP case. The curve at $n_e = 0.01 n_c$, instead, displays lower charges-per-Joule. Globally, in all three cases, we observe that increasing the laser energy leads to a decrease in the charge-per-Joule. For $n_e \geq 0.02 n_c$ and $E_L = 0.25$ J the charge-per-Joule reaches a plateau around 36 nC/J/sr. With the smaller nozzle and the f/8 OAP we measure a maximum charge-per-Joule 143 nC/J/sr (i.e., 2.3 nC) at $n_e = 0.045 n_c$ and $E_L = 0.06$ J, corresponding to

$\eta = 12.2\%$. At full laser energy and $n_e = 0.045 n_c$, instead, we measure 39 nC/J/sr (i.e., 9.7 nC) and $\eta = 3.4\%$. With the 2 mm nozzle and $f/8$ OAP (Fig. 4.8(b)) we measure charges-per-Joule similar to those obtained with the $f/4$ OAP (dashed curve). However, it is important to note that the data for the two parabolas was obtained on different days. From Fig. 4.8(b) we notice that using the bigger nozzle and the $f/8$ OAP we were able to reach a maximum charge-per-Joule of 110.5 nC/J/sr at $E_L = 0.12 \text{ J}$ (i.e., 3.5 nC and $\eta = 10.6\%$).

From the results presented in this section, it is possible to conclude that we achieved unprecedented charge-per-Joule values with both nozzles and parabolas. Notably, using the 2 mm nozzle at $n_e = 0.59 n_c$ and $E_L = 0.13 \text{ J}$, we measured 89 nC/J/sr , with an efficiency of $\eta = 14.4\%$. The collecting cone was 0.5 sr , resulting in $\sim 45 \text{ nC/J}$, which exceeds the Multiscan 3D project requirements of 10 nC/J by more than four times.

4.2.3 Electron Beam Energy Spectrum and Divergence

The colored stripes in Fig. 4.9(a) and (b) represent examples of the energy spectra measured with the 0.4 mm and 2 mm nozzle respectively, for different laser energies and with the $f/4$ OAP. Specifically, the spectra in Fig. 4.9(a) were obtained at $n_e = 0.06 n_c$, while in Fig. 4.9(b) at $n_e = 0.29 n_c$. Each stripe was obtained as the RMSE on ten consecutive shots. Here, we can see that the spectra maintain a similar shape for different laser energies, while the only noticeable effect is an increase of the charge on the spectrometer for higher laser energies, as observed in previous works (Guillaume et al., 2015). For instance, in Fig. 4.9(a) we estimate that the charge increases from $13.4 \pm 2.5 \text{ pC}$ to $39.9 \pm 3.3 \text{ pC}$ between $E_L = 0.12 \text{ J}$ and $E_L = 1 \text{ J}$. Within the same laser energy range, we measure between $8.64 \pm 2.98 \text{ pC}$ and $65.9 \pm 8.43 \text{ pC}$ with the bigger nozzle (i.e., Fig. 4.9(b)). We also notice that the electron average energy remains consistent for different laser energies for both gas targets. Indeed, with the smaller nozzle we estimate an average energy of $5.26 \pm 0.1 \text{ MeV}$, while for the bigger one $5.25 \pm 0.12 \text{ MeV}$. In this chapter, we calculate the average energy considering the range between 1.2 MeV and 15 MeV , unless specified otherwise.

Thanks to the horizontally motorized electron spectrometer, we were able to measure the energy spectra at different positions, as shown in Fig. 4.10. In this figure, the spectra are shown between 3 MeV and 10 MeV and they were obtained as the average on five consecutive shots. Each colored surface corresponds to a spectrum measured at a different value of the horizontal angle Θ_x , which ranges between -245 mrad to 245 mrad with a step of around 80 mrad . The sampling position used to retrieve each spectrum is represented by the colored

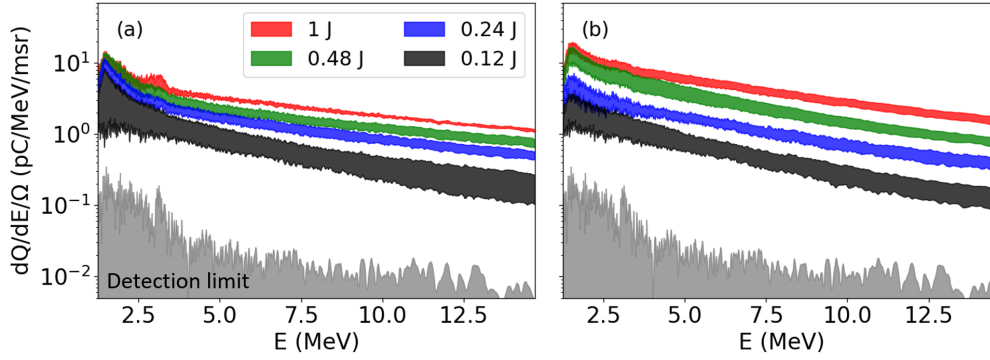


Figure 4.9: Energy spectra obtained using the f/4 OAP with (a) the 0.4 mm nozzle at $n_e = 0.06 n_c$ and (b) with the 2 mm nozzle at $n_e = 0.29 n_c$ for different laser energies. The gray surface represents the detection limit.

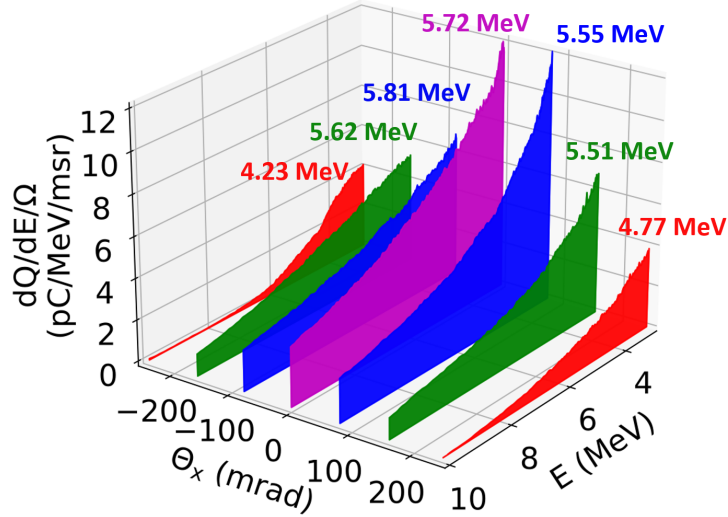


Figure 4.10: Energy spectra measured at different horizontal positions using the f/4 OAP and the 2 mm nozzle, considering $n_e = 0.29 n_c$ and $E_L = 1$ J. Here, Θ_x is the horizontal angle. The colored values represent the average energy of each corresponding spectrum.

circles in Fig. 4.12(b), where we present a BPM image obtained in the same conditions of Fig. 4.10. Thus, from Fig. 4.10 it is possible to conclude that the most divergent electrons are also the least energetic. If we compare, for instance, the spectrum measured on the laser axis (i.e., $\Theta_x = 0$) with the one at $\Theta_x = 245$ mrad, we estimate the electron average energy to decrease from 5.72 ± 0.01 MeV to 4.77 ± 0.02 MeV. In this case, the average energy is calculated between 3 MeV and 10 MeV. Furthermore, we observe that at $\Theta_x = \pm 245$ mrad the tail of the energy spectrum falls below ~ 10 MeV, the limit imposed by certain countries' regulations for preventing the activation of materials (U.S. Food and Drug Administration, 1977). This observation indicates the potential for selecting a desired energy range by filtering the electron beam according to its divergence. In Fig. 4.11(a) and (b) we see examples of the energy spectra produced using the f/8 OAP, for the 0.4 mm and 2 mm nozzle respectively. For a proper interpretation of these results, it is important to note that these spectra were obtained on two different days of the experimental campaign. Nonetheless, we notice that with this parabola we obtain spectra similar to those in Fig. 4.9(a) and (b). In this case, we estimate average energies around 5.97 ± 0.73 MeV and 5.53 ± 0.49 MeV for the smaller and bigger nozzle respectively.

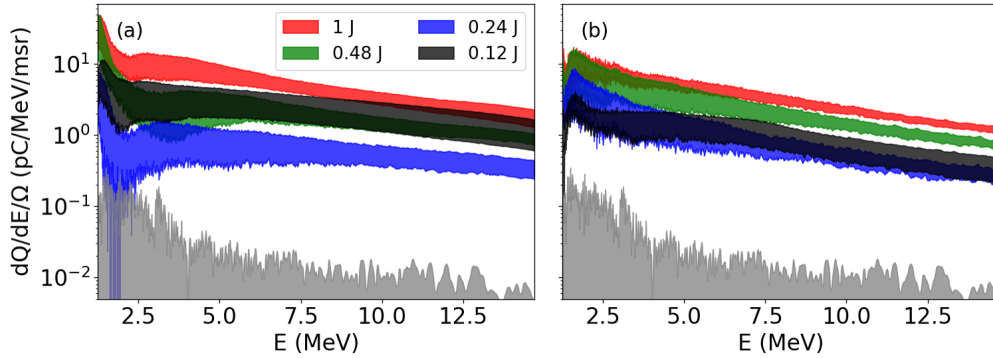


Figure 4.11: Energy spectra obtained using the f/8 OAP with (a) the 0.4 mm nozzle at $n_e = 0.045 n_c$ and (b) with the 2 mm nozzle at $n_e = 0.29 n_c$ for different laser energies. The gray surface represents the detection limit. These spectra were obtained on two different days.

In Figs. 4.12(a-d) we present four single-shot BPM images obtained with the 2 mm nozzle. These images provide us with the data to retrieve the charges-per-Joule discussed in Fig. 4.7(a) and (b) and to estimate the beam divergence. Specifically, Fig. 4.12(a) and (b) were obtained with a plasma density $n_e = 0.29 n_c$ at $E_L = 0.13$ J and $E_L = 1$ J. Fig. 4.12(c) and (d), instead, were produced with $n_e = 0.59 n_c$ and the same laser energies of Fig. 4.12(a) and (b). The white curves

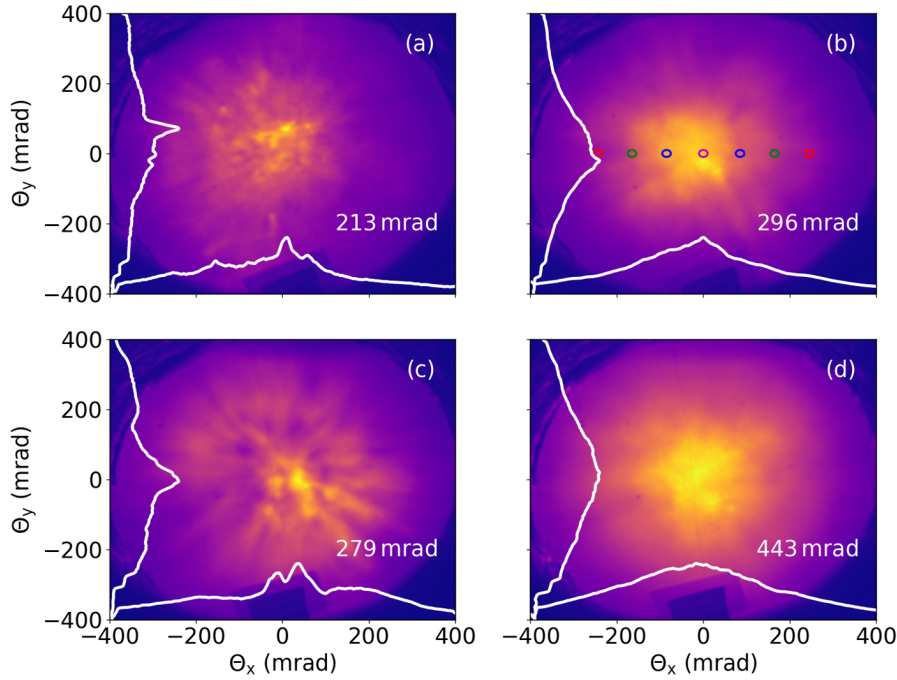


Figure 4.12: BPM images obtained with the 2 mm nozzle and f/4 OAP for (a) $n_e = 0.29 n_c$ and $E_L = 0.13$ J (b) $n_e = 0.29 n_c$ and $E_L = 1$ J (c) $n_e = 0.59 n_c$ and $E_L = 0.13$ J (d) $n_e = 0.59 n_c$ and $E_L = 1$ J. The value on each image refers to the FWHM beam divergence. The colored circles in (b) refer to the spectrometer sampling position, which allowed to retrieve the spectra in Fig. 4.10. Each image is normalized to its maximum value, with the white curves representing the transverse and longitudinal beam profiles passing through the peak of each image.

represent the transverse and longitudinal beam profile passing through the maxima of each image, allowing to better compare the beam dimension to the one of the scintillating screen. Figs. 4.12(a-d) prove that both an increase in the laser energy and plasma density yields a more significant beam expansion, leading to FWHM divergences between 200 mrad and 440 mrad. Fig. 4.13(a) and (b) illustrate BPM images obtained with the f/8 OAP and 2 mm nozzle for $n_e = 0.29 n_c$ at $E_L = 0.13$ J and $E_L = 1$ J respectively. For comparison, in Fig. 4.13(c) and (d) we present BPM images obtained on a different experiment day in the same conditions, using the f/4 OAP. Furthermore, it is essential to note that with the f/4 OAP the BPM screen was placed closer to the source. In conclusion, from these images, we deduce that for the same laser energy and plasma density, the f/4 OAP allows to produce more divergent electrons than the f/8 OAP case. At $E_L = 0.13$ J, for instance, we estimate a FWHM divergence of around 61 mrad and 231 mrad with the f/4 and f/8

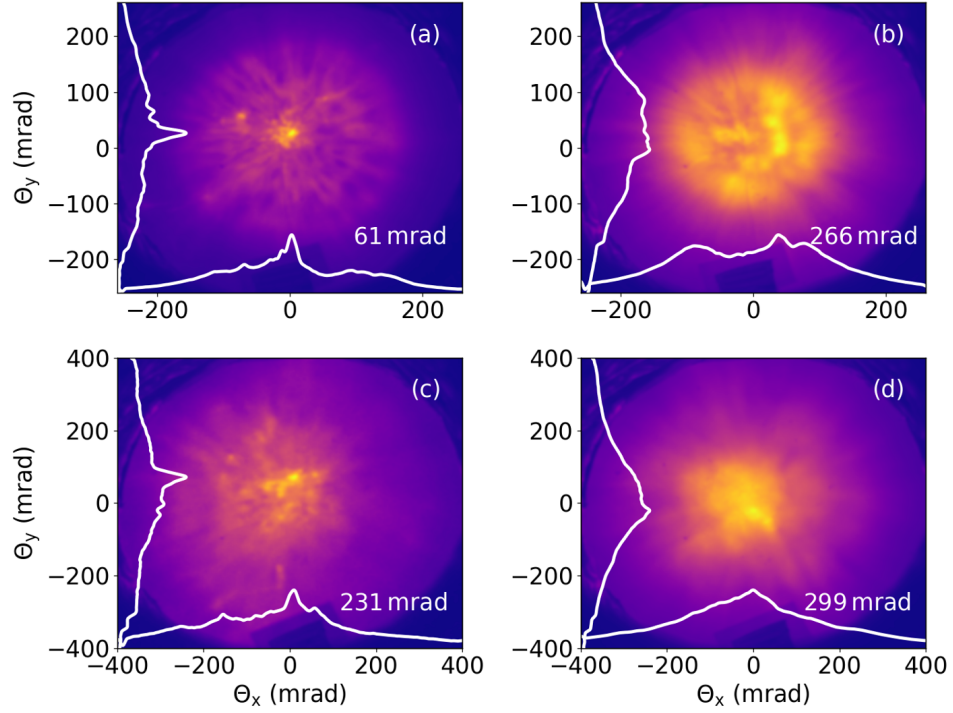


Figure 4.13: BPM images obtained with the 2 mm nozzle, f/8 OAP and at $n_e = 0.29 n_c$ for (a) $E_L = 0.13$ J (b) $E_L = 1$ J. Images obtained with the 2 mm nozzle, f/4 OAP and at $n_e = 0.29 n_c$ for (c) $E_L = 0.13$ J (d) $E_L = 1$ J. Each image is normalized to its maximum value, with the white curves representing the transverse and longitudinal beam profiles passing through the peak of each image.

OAPs respectively.

4.2.4 Electron Beam Dose

As discussed in Section 2.3.5, we performed dose measurements to further characterize this electron source. In Fig. 4.14 we present the setup employed to perform dose measurements using the film stack, which was positioned at 6 cm from the gas jet. Moreover, we recall that the stack was composed of eleven 10×10 cm² Gafchromic EBT3 films distanced using aluminum and Teflon bricks of different thicknesses (see Fig. 2.9).

Before presenting the actual doses we were able to measure, we define the projected density ρ_p , allowing to account for the different materials and thicknesses crossed by the electron beam. Thus, on the N -th EBT3 film we define the projected

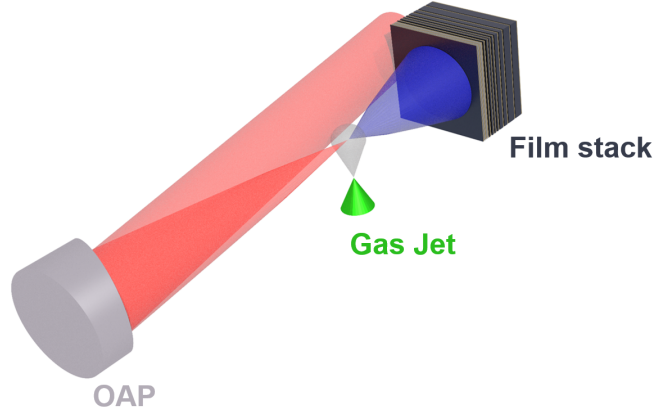


Figure 4.14: Dose measurements setup. The film stack was placed in the vacuum chamber at 6 cm from the electron source.

density as

$$\rho_p(N) = \rho_{Al} \sum_i^{N_{Al}} d_{i,Al} + \rho_T \sum_j^{N_T} d_{j,T} + \rho_E(N-1)d_E. \quad (4.1)$$

Here, $\rho_{Al} = 2.7 \text{ g/cm}^3$, $\rho_T = 2.2 \text{ g/cm}^3$ and $\rho_E = 1.4 \text{ g/cm}^3$ represent the aluminum, Teflon and EBT3 film density respectively, while $d_{i,Al}$, $d_{j,T}$ and d_E are their widths. Thus, before reaching the N -th film, the electron beam has to cross N_{Al} aluminum bricks, N_T Teflon bricks and $N - 1$ EBT3 films. Figs. 4.15(a-d) illustrate examples of the dose maps obtained with the dosimetry stack. Each map corresponds to a distinct EBT3 film positioned at different depths within the stack. Specifically, due to the EBT3 dynamic range (i.e., 0.1 Gy – 20 Gy), Fig. 4.15(a-d) displays the first four films with doses below 20 Gy. These dose maps were obtained accumulating over two shots, employing the 2 mm nozzle at $n_e = 0.29 n_c$ and $E_L = 1 \text{ J}$. The white dashed circles highlight a 20 mm diameter Region Of Interest (ROI) centered with respect to the maximum value in Fig. 4.15(a). This diameter corresponds to the beam FWHM divergence (i.e., $\sim 300 \text{ mrad}$) obtained at $n_e = 0.29 n_c$ and $E_L = 1 \text{ J}$. Hence, we employ this ROI to estimate the average dose per shot (\tilde{D}) on each film. The blue curves in Fig. 4.15(e) display the average dose-per-shot across the projected density ρ_p obtained with the f/4 OAP for the 0.4 mm (squares) and 2 mm (dots) nozzles. With the 0.4 mm nozzle we have accumulated the dose over four shots. The red curves, instead, refer to the average dose-per-shot obtained with the f/8 OAP for the two gas targets. In these cases, we have accumulated two shots with the bigger nozzle and one

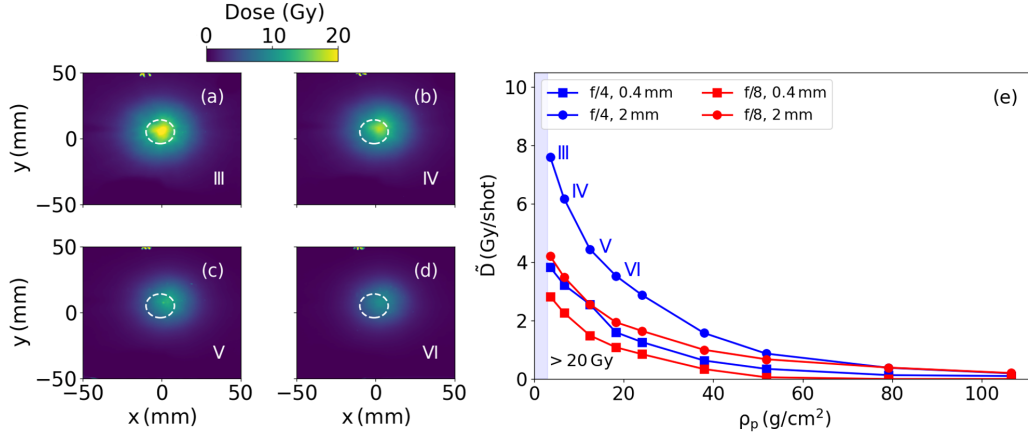


Figure 4.15: (a-d) Dose maps numbered with respect to the film position in the stack obtained with the 2 mm nozzle for $n_e = 0.29 n_c$ and $E_L = 1$ J. (e) Average dose per shot on each film in a 20 mm diameter circle, as indicated by the dashed circles in (a-d), obtained with the 2 mm nozzle (blue curve) and 0.4 mm at $n_e = 0.06 n_c$ and $E_L = 1$ J (red curve).

with the smaller target. Moreover, with the 0.4 mm nozzle, the plasma density was $n_e = 0.06 n_c$ and $E_L = 1$ J. For all curves of Fig. 4.15(e) we have assumed the same ROI we previously described, allowing for the comparison between the different configurations. Thus, from Fig. 4.15(e) we deduce that the electron beam produced with the bigger nozzle and the f/4 OAP delivers higher doses than the one produced with the smaller nozzle. If we consider, for instance, the third film (i.e., $\rho_p \approx 3.6$ g/cm²), we estimate an average dose-per-shot around 8 Gy with the 2 mm nozzle, while with the 0.4 mm nozzle we only estimate 4 Gy. Also with the f/8 OAP we notice that the beam produced with the bigger nozzle delivers higher doses than the one with the smaller nozzle. On the third film, for instance, we estimate an average dose-per-shot around 2.8 Gy and 4.2 Gy with the 0.4 mm and 2 mm nozzle respectively. The attainment of such high doses-per-shot could potentially prove this electron source interesting for irradiation studies.

4.3 Conclusion

In this chapter, we have explored the main experimental results of this work. After presenting the experimental setup and recalling the main diagnostics, we have characterized both the laser and gas targets we used, allowing to better identify the regime under investigation. During the experiment, we have employed different

nozzles, backing pressures, laser energies and off-axis parabolas. Thus, we were able to find the conditions to produce up to 45 nC/J (i.e., 5.7 nC) to few-MeVs, with a conversion efficiency $\sim 14\%$, one of the highest ever recorded. These results demonstrate that we exceeded 10 nC/J, thus reaching our goal. Furthermore, considering future laser systems that promise to achieve average powers above 100 W, this configuration could pave the way to the production of laser-plasma-accelerated electron beams with average currents $> 4 \mu\text{A}$, surpassing the current state of the art. This, in turn, could prove this electron source interesting for applications such as the Multiscan 3D project or even for irradiation studies.

In the following, we will explore the physics in detail by means of a detailed numerical study. This will ultimately allow us to understand the main phenomena related to both the laser propagation and electron acceleration under the conditions of interest.

Chapter 5

Simulations on few-MeV Highly-Charged Beams

In this chapter, we explore the production of few-MeV, highly-charged beams through FBPIC simulations. First, we introduce *FBPIC-Electric Work Profiler* (FBPIC-EWP), a tool we specifically developed to study the role of laser and plasma fields in the acceleration processes. In the second section, we present numerical results obtained from a set of simulations in an idealized case, providing insights into laser diffraction and acceleration mechanisms. Here, we offer a possible explanation for the charge-per-Joule saturation effect observed in Chapter 4. In the final section, we present a second set of simulations, which consider configurations similar to those used in the experiments.

Contents

5.1	FBPIC-Electric Work Profiler	90
5.2	Numerical Simulations: Idealized Case	91
5.2.1	Simulation Setup	91
5.2.2	Laser Diffraction in High Plasma Densities	93
5.2.3	Acceleration of few-MeV Electron Beams	96
5.2.4	Charge-per-Joule Saturation Effect	105
5.3	Numerical Simulations: Experimental Conditions	107
5.3.1	Simulation Setup	108
5.3.2	Laser Diffraction and Plasma Structures	109
5.3.3	Beam Properties	112
5.4	Conclusion	113

5.1 FBPIC-Electric Work Profiler

FBPIC-Electric Work Profiler (Martelli and Andriyash, 2024) is a post-processing tool for FBPIC. This code simply allows to estimate the work performed by the laser and the plasma fields on FBPIC-tracked electrons. As we have previously discussed, FBPIC employs a set of 2D cylindrical grids to represent fields with distinct azimuthal modes. While $m = 0$ corresponds to fields independent of the azimuthal angle, $m > 1$ represents fields varying proportionally to $\cos(\theta)$ and $\sin(\theta)$. Ideally, the mode corresponding to $m = 0$ represents the plasma field and $m = 1$ the laser field¹. Thus, at each FBPIC iteration, FBPIC-EWP retrieves the total electric field on every tracked particle, defined as the sum of the plasma and laser field, namely, $\mathbf{E}_T = \mathbf{E}_W + \mathbf{E}_L$. FBPIC-EWP also retrieves the velocity $\mathbf{v} = (v_x, v_y, v_z)$. For completeness, we recall that the electric fields and velocities are calculated on two different grids by FBPIC. Subsequently, a 2D linear interpolation is performed for $m = 0$ in order to determine the wakefield on each electron and the laser electric field is retrieved as $\mathbf{E}_L = \mathbf{E}_T - \mathbf{E}_W$. Finally, the work at a given instant t is calculated as

$$W(t)_{W,L} = -e \int_0^t \mathbf{E}_{W,L} \cdot \mathbf{v} dt', \quad (5.1)$$

where the subscripts W and L refer to the wakefield and laser field respectively.

As we will discuss in detail in the following, this code allowed us to identify three main acceleration mechanisms: ponderomotive acceleration, direct laser acceleration and wakefield acceleration.

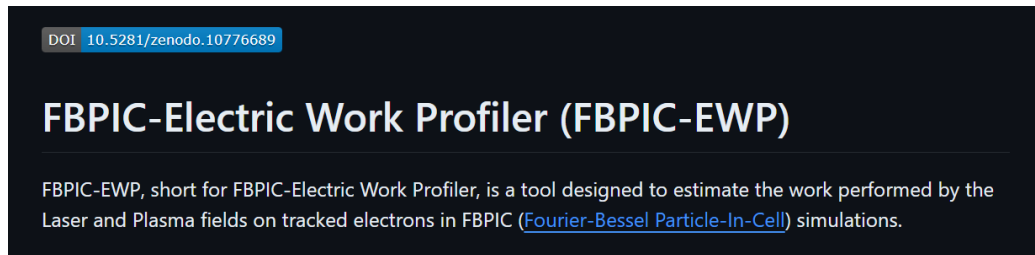


Figure 5.1: FBPIC-Electric Work Profiler GitHub repository.

¹This is valid because we are considering a linear laser polarization.

5.2 Numerical Simulations: Idealized Case

The simulations of this section have been performed in the case of a perfectly Gaussian beam propagating in a constant plasma density. We intend to get some insights concerning the laser propagation and electron beam properties under idealized conditions, to identify the main physical processes at play. Here, we first present an example that will allow to understand the rationale of the parametric study presented in this section.

5.2.1 Simulation Setup

In order for the simulation to run, it is necessary to define the laser pulse inside a *co-moving window* (or box). This window propagates with the laser at the speed of light and its size and meshing are of great importance to properly capture the interaction between the laser and the plasma. Fig. 5.2(a) depicts a 2D map of the laser at the first iteration, where x, y and z represent the transverse and longitudinal coordinates respectively with respect to the laboratory frame. Here, the laser is linearly polarized along the x -direction and it propagates toward positive z . The simulation box size is $\sim 102 \times 60 \mu\text{m}^2$, while in Fig. 5.2 it has been reduced for visual purposes. In Fig. 5.2(b) it is also possible to notice a longitudinal cut of the laser pulse presented along the white dashed line in Fig. 5.2(a). In this figure, we notice that the laser centroid has been defined at a distance of $2c\tau$ from the window's right boundary, where $\tau = 30$ fs, similar to what we can achieve in Salle Jaune. Concerning the sampling of the co-moving window, we have defined a (r, z) mesh with a longitudinal and radial step size equal to $\Delta z = \lambda/24$ and $\Delta r = 5\Delta z$ respectively, where $\lambda = 800$ nm. The simulations run for the whole interaction time, which is simply defined as the whole plasma density length (i.e., $1530 \mu\text{m}$ in this case) divided by the moving window velocity, while the timestep is $\Delta t = \Delta z/c$. Further details about the simulation setup can be found in Appendix A.

In Fig. 5.3 we show a schematic representation of FBPIC simulations in idealized conditions. Here, it is possible to observe a Gaussian laser pulse propagating in a $1500 \mu\text{m}$ constant plasma density profile. Before reaching the density plateau, we let the laser propagate through a rising ramp of $30 \mu\text{m}$, allowing for a smooth focusing in plasma and limited energy loss. To perform a meaningful study for the understanding of the experimental results of Chapter 4, the laser beam waist (i.e., w_0) is chosen considering the laser FWHM diameter focused with the $f/4$ OAP (i.e., $d \approx 5 \mu\text{m}$). It is easy to show that $w_0 = d/2 (\ln 2)^{-1/2}$, which yields $w_0 = 3 \mu\text{m}$. Furthermore, in Fig. 5.3 we highlight the laser energy range, namely between 0.05 J and 1 J. Thus, the laser intensity peak is varied between 1.1×10^{19} W/cm⁻² and 2.2×10^{20} W/cm⁻², corresponding to $a_0 \in [2.3, 10.2]$. Fig. 5.3 also depicts

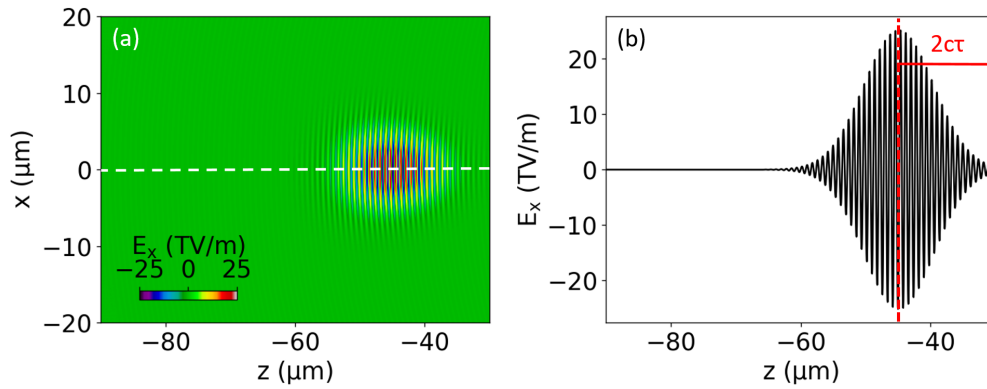


Figure 5.2: (a) 2D map of the laser pulse inside the co-moving box. (b) Longitudinal cut of the laser pulse map along the white dashed line in (a). It is possible to notice the laser centroid position with respect to the window's right boundary.

the densities we have considered, namely between $n_e = 0.02 n_c$ and $n_e = 0.18 n_c$, where we recall that $n_c(\text{cm}^{-3}) = 1.1 \times 10^{21}/\lambda(\text{nm})$ is the critical plasma density. Here, the plasma density is derived from the full nitrogen L-shell ionization (i.e., N^{+5}). Furthermore, for all the simulations that we will discuss in this section, we have assumed the nitrogen gas to be preionized to N^{+3} for numerical ease. This choice is justified since the first three nitrogen L-shell electrons are easily ionized by the laser leading edge, as discussed in Section 1.1.2.

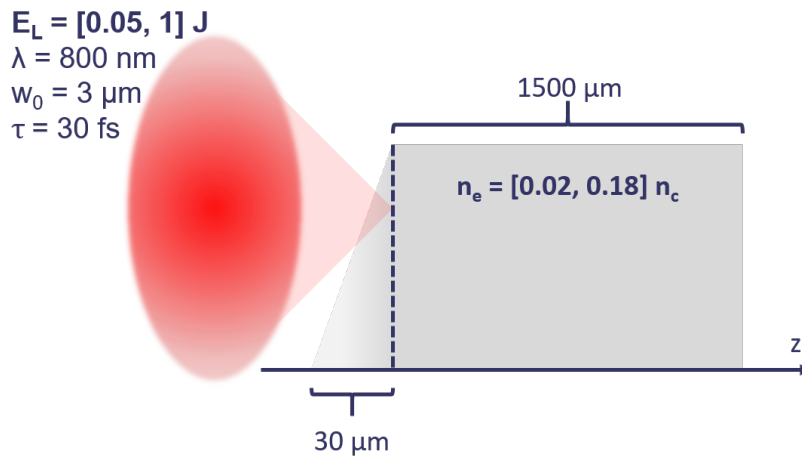


Figure 5.3: Schematic representation of FBPIC simulations in idealized conditions.

5.2.2 Laser Diffraction in High Plasma Densities

To discuss laser diffraction, we now proceed by considering the two simulations at $n_e = 0.06 n_c$ with $E_L = 0.12 \text{ J}$ and $E_L = 1 \text{ J}$ shown in Fig. 5.4(a) and (b). Specifically, the gray colormap illustrates the plasma density (i.e., n_e/n_c), while the red colormap represents the laser, expressed in terms of the normalized vector potential in the co-moving box reference frame, namely $(z - ct, x)$. On each

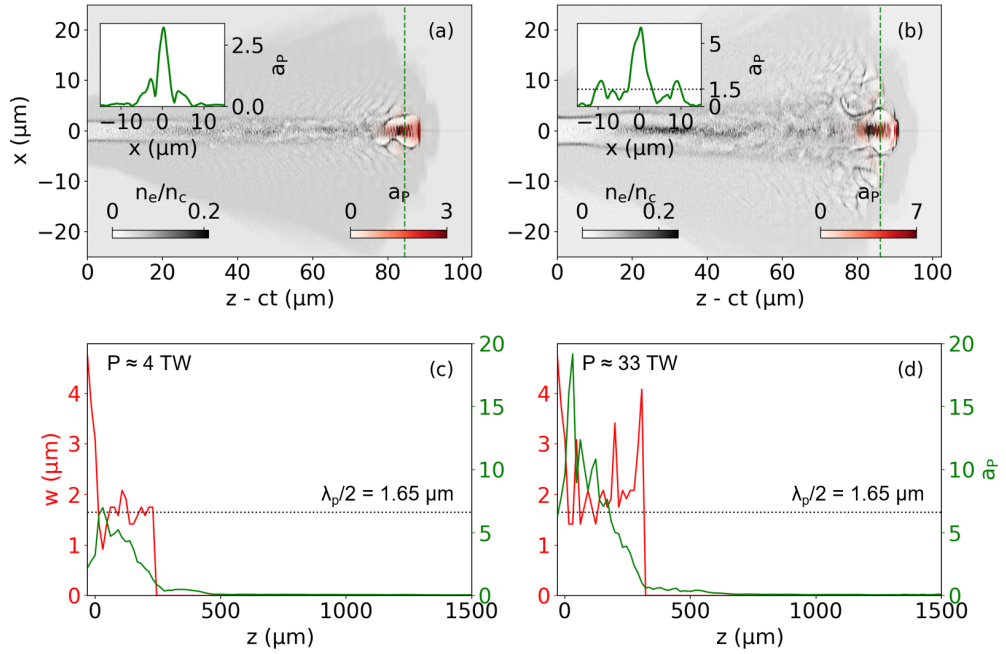


Figure 5.4: FBPIC results for $n_e = 0.06 n_c$. The gray colormap represents density snapshots at (a) $E_L = 0.12 \text{ J}$ and at (b) $E_L = 1 \text{ J}$. The red colormap represents the laser envelope, expressed in terms of the normalized vector potential. The insets refer to the laser transverse profile along the green dashed line. (c-d) Beam waist and normalized vector potential in plasma for $E_L = 0.12 \text{ J}$ and $E_L = 1 \text{ J}$.

snapshot, we also present the transverse laser profile along the green dashed line. From these images, we can already observe the emergence of interesting plasma structures, prompting questions about the underlying acceleration mechanisms, as we will discuss in Section 5.2.3. From these images, we can notice that the laser stops behaving as a Gaussian beam. Indeed, from the inset of each snapshot, it is possible to observe the appearance of sidelobes, highlighting the occurrence of *beam-break up* (Thomas et al., 2007), a phenomenon seeded by self-focusing. These sidelobes can reach sufficiently high intensities to cause K-shell ionization, as shown in the inset of Fig. 5.4(b), where we highlight that the laser normalized

vector potential in plasma $a_P > 1.5$. The density colormap of Fig. 5.4(b) also highlights the excitation of plasma modes far from the laser axis (i.e., at a distance exceeding $\sim 2w_0$), due to the presence of these intense sidelobes. In Fig. 5.4(c) and (d), we plot the laser spot size (w) and normalized vector potential over the depth in plasma (z), for the configurations presented in Fig. 5.4(a) and (b) respectively. Considering the range of laser energy and plasma density of interest, it is straightforward to notice that the laser power exceeds the critical power (i.e., $P > P_c(\text{GW}) \approx 17n_c/n_e$), which ensures the occurrence of self-focusing. Indeed, for $n_e = 0.06 n_c$ we estimate $P_c \approx 0.3 \text{ TW}$, while the laser power is $P = 4 \text{ TW}$ and $P = 33 \text{ TW}$ for $E_L = 0.12 \text{ J}$ and $E_L = 1 \text{ J}$ respectively. Hence, from Fig 5.4(c) and (d) we deduce that self-focusing allows to keep the laser focused in plasma for distances several times the Rayleigh length ($Z_R \approx 35 \mu\text{m}$). For instance, in Fig 5.4(c), we see that the laser remains guided over a distance $L \approx 7 Z_R$ before being depleted. Moreover, we notice that the laser waist oscillates around $\lambda_p/2$, as already observed in other works (Thomas et al., 2007, Mangles et al., 2008). This, in turn, means that higher plasma densities would lead to a tighter focusing and, consequently, to higher values of the normalized vector potential. As it is possible to infer from Fig 5.4(d), displaying the results obtained at $n_e = 0.06 n_c$ and $E_L = 1 \text{ J}$, the normalized vector potential in plasma can reach up to $a_{P,max} \approx 20$ shortly after the density ramp. In a vacuum, instead, we recall that with $E_L = 1 \text{ J}$ the maximum normalized vector potential is $a_0 \approx 10$. To describe this effect in a simple way, we now consider a 30 fs-Gaussian beam focused in a vacuum down to $w_0 = \lambda_p/2$. From Eq. (1.24) we recall the definition of laser peak intensity, namely $I_0 = 2 E_L / (\pi w_0^2 \tau)$. Hence, considering $w_0 = \lambda_p/2$ and from Eq. (1.24) we write

$$I_0 = \frac{8 E_L}{\pi \lambda_p^2 \tau}. \quad (5.2)$$

Knowing that $a_0 \approx 0.86\lambda(\mu\text{m}) \times \sqrt{I_0(10^{18}\text{W}/\text{cm}^2)}$ and from Eq. (5.2) we can write the following expression for the maximum normalized vector potential in plasma (i.e., $a_{P,max}$) in practical units

$$a_{P,max} \approx 91 \sqrt{n_e/n_c \times E_L(\text{J})}, \quad (5.3)$$

The colored dots in Fig 5.5(a) represent the $a_{P,max}$ values obtained with FBPIC, while the discontinuous lines have been obtained with Eq. (5.3). Hence, we can notice the good agreement of Eq. (5.3) with the numerical results for the first three plasma densities, namely between $n_e = 0.02 n_c$ and $n_e = 0.06 n_c$. At $n_e = 0.18 n_c$, instead, we see that Eq. (5.3) overestimates the normalized vector potential. At higher plasma densities, phenomena like laser depletion, dispersion and reflection can occur over the density ramp leading to lower values of $a_{P,max}$ than those

predicted by Eq. (5.3). Nonetheless, we empirically found Eq. (5.4), which allows for a better agreement with the numerical results, as displayed in Fig 5.5(b).

$$a_{P,max} \approx 91 \sqrt{n_e/n_c \times E_L(\text{J})} (1 - n_e/n_c), \quad (5.4)$$

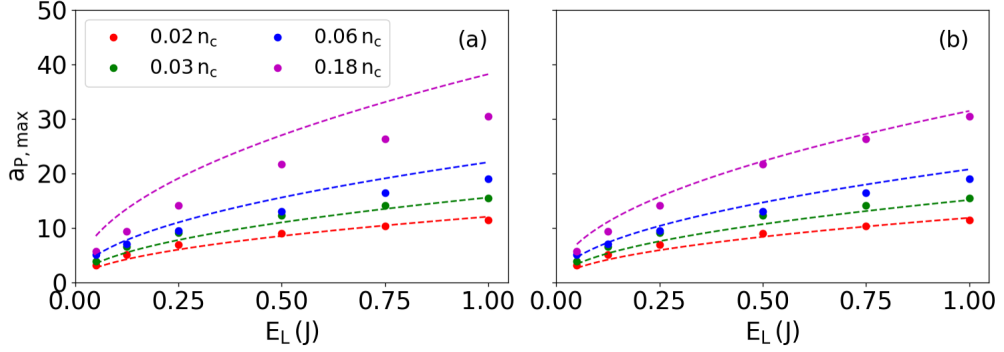


Figure 5.5: (a) Maximum normalized vector potential in plasma ($a_{P,max}$) for different plasma densities and laser energies. The dots refer to the values obtained through FBPIC simulations, while the discontinuous lines in (a) have been obtained with Eq. (5.3) and in (b) with Eq. (5.4).

We conclude this section by examining the pump depletion length L_{pd} . Here, we define L_{pd} as the distance in plasma where the laser has $a_P \gtrsim 1$, i.e., ensuring the generation of a non-linear wakefield. As we discussed in Chapter 1, this quantity is relevant since it allows to describe one mechanism that hinders the electron energy gain in laser-plasma accelerators. Furthermore, laser pulse depletion can significantly limit the maximum achievable charge. Hence, in Fig 5.6 we present the pump depletion length (dots) for different densities as a function of the vacuum maximum normalized vector potential a_0 . In this figure, we observe that the pump depletion length displays a small linear increase over a_0 , while it strongly depends on the plasma density. Specifically, we deduce the following empiric scaling of the pump depletion length

$$L_{pd} \propto \frac{a_0 + K}{n_e/n_c}, \quad (5.5)$$

where K is a constant we numerically determined and since $K \gg a_0$ for $a_0 \in [2, 10]$, we can write $L_{pd} \propto K n_c/n_e$. A similar scaling was obtained by [Lu et al. \(2007\)](#) for $k_p w_0 = 2\sqrt{a_0}$, with $a_0 > 2$ (see Section 1.2.4). From the numerical study, we obtain the following expression of the depletion length in practical units

$$L_{pd}(\mu\text{m}) \approx 16 n_c/n_e. \quad (5.6)$$

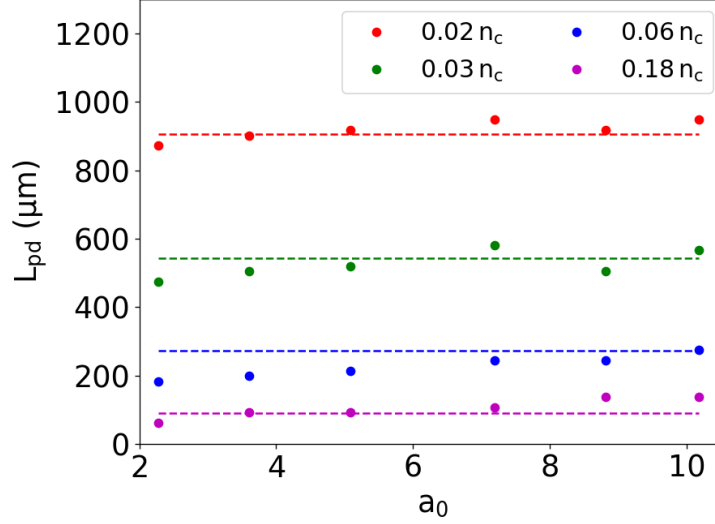


Figure 5.6: Pump depletion length (L_{pd}) for different densities, across different a_0 s. The dots represent the numerical results, while the dashed lines are a fit of the form $L_{pd}(\mu\text{m}) \approx 16 n_c/n_e$.

5.2.3 Acceleration of few-MeV Electron Beams

In this section, we discuss the acceleration mechanisms under the conditions of interest. Specifically, we examine the simulation at $n_e = 0.03 n_c$, considering a 1 J laser pulse. As already discussed, this is done by analyzing FBPIC particle tracking results with FBPIC-EWP. However, before exploring the actual acceleration mechanisms in detail, we wish to illustrate some generalities about the structures in plasma. This, in turn, allows for a better understanding of the overall physics and electron dynamics. Following this, we explore the identified acceleration mechanisms and discuss some representative examples. We begin by presenting the trajectories of K-shell electrons. Since L-shell electrons exhibit similar dynamics and experience analogous acceleration mechanisms, they will be discussed subsequently.

Channel Formation The numerical analysis underlines the formation of a massive and rapidly changing channel-like structure shortly after the end of the density ramp. Fig. 5.7 depicts the density snapshots of four consecutive iterations (1 – 4),

where the gray (green) colormap refers to L-shell (K-shell) electrons, while the red colormap is a_P . Here, we notice that the laser's ponderomotive force radially pushes L-shell electrons upon interacting with the density plateau, creating a copropagating ion cavity (1). Simultaneously, a significant number of K-shell electrons are ionized into the cavity. The continuous loading leads to the accumulation of K-shell electrons on the laser axis (2 – 3). Thus, due to the high concentration of K-shell electrons on axis, L-shell electrons cannot close their trajectories to form ion cavities. Instead, they slip to the rear, forming a channel-like sheath, surrounding K-shell electrons (4). We estimate a maximum channel

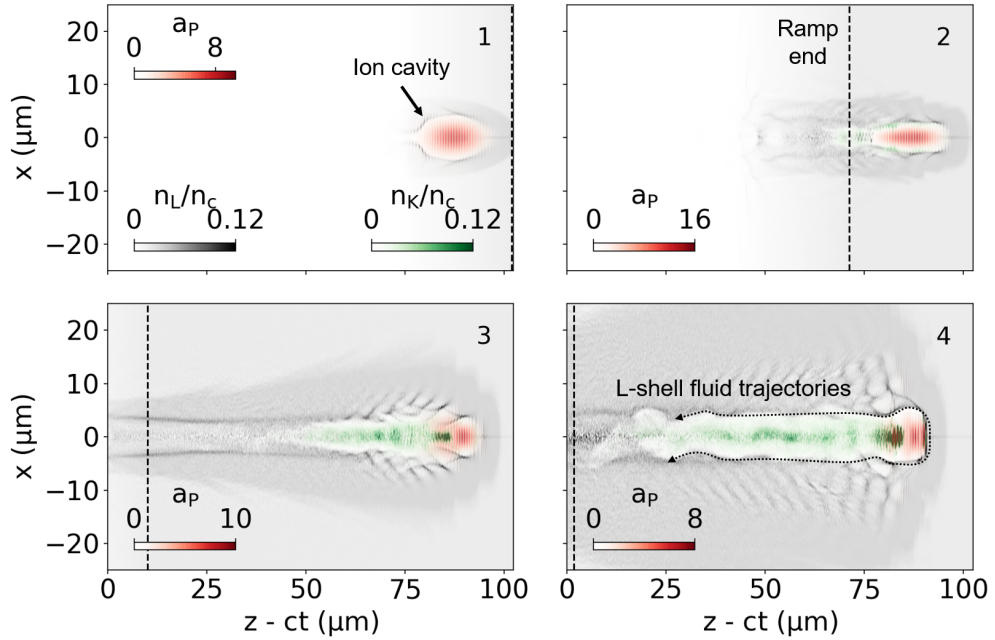


Figure 5.7: (1 – 4) Plasma density snapshots of four consecutive iterations. The gray and green colormaps refer to the L- and K-shell electron density. In red we depict a_P . These panels allow to observe the generation of a channel-like structure.

length of $\sim 70 \mu\text{m}$, corresponding to $\sim 15\lambda_p$ and a radius of around $6 \mu\text{m}$, slightly exceeding the ion cavity radius in the blowout regime (Lu et al., 2007), namely $r_b = 2\sqrt{a_0}/k_p \approx 4.7 \mu\text{m}$. Compared to Lu et al. (2007), here, the laser is experiencing a much stronger self-focusing, reaching higher intensities in plasma than in a vacuum, as discussed in the previous section (i.e., see Eq. (5.4)). Furthermore, Lu et al. (2007) considers a resonant laser pulse, as discussed in Section 1.2.3. Hence, if we now substitute a_0 with $a_{P,max}$ in $r_b = 2\sqrt{a_0}/k_p$, we yield a radius of $\sim 5.7 \mu\text{m}$, which is in better agreement with the simulation results. Thus, as

we will further discuss in the following, we empirically find that the channel's maximum radius is $r_c \approx 2\sqrt{a_{P,max}}/k_p$ and from Eq. (5.4), we can write in practical units

$$r_c(\mu\text{m}) \approx 2.4 E_L^{1/4}(\text{J}) (n_e/n_c)^{-1/4} (1 - n_e/n_c)^{1/2}. \quad (5.7)$$

In Fig. 5.8(a) we present the last density snapshot of Fig. 5.7. For visual pur-

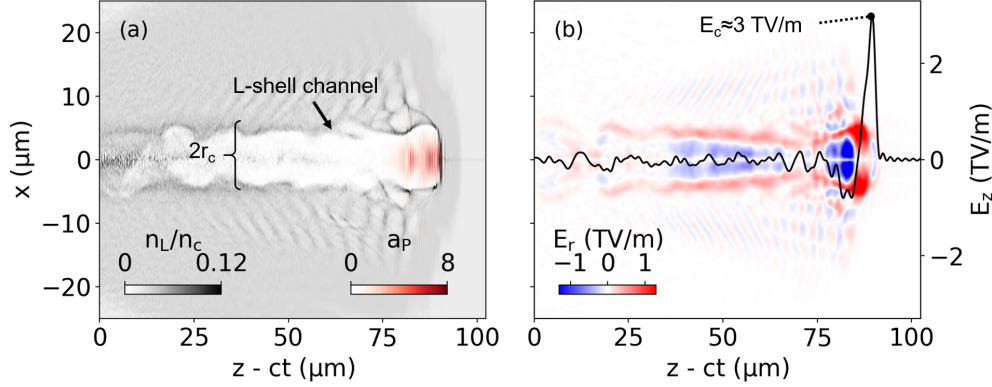


Figure 5.8: (a) Plasma density snapshot of the last panel of Fig. 5.7. The gray colormap refers to L-shell electrons, while the red one refers to the laser. (b) Radial wakefield map (E_r) and longitudinal wakefield (E_z) corresponding to the snapshot shown in (a).

poses, in Fig. 5.8(a) we only display the density of L-shell electrons, allowing to highlight the channel structure. In this figure, it is also possible to notice that the channel diameter corresponds to approximately $2r_c \approx 11 \mu\text{m}$. Fig. 5.8(b), instead, illustrates the radial wakefield map (E_r) and the longitudinal wakefield (E_z) corresponding to the iteration of Fig. 5.8(a). At the front of the channel structure, the laser ponderomotive force allows for an effective charge separation, generating an ion cavity. Here, the wakefield reaches a maximum of $\sim 3 \text{ TV/m}$, slightly exceeding the value predicted by (Lu et al., 2007) with Eq. (1.88), namely $E_0(\text{GV}\cdot\text{m}^{-1}) \approx 96\sqrt{a_0 n_e(10^{18}\text{cm}^{-3})} \approx 2.2 \text{ TV/m}$. Similarly to our prior discussion, we replace a_0 with $a_{P,max}$ in Eq. (1.88) and we find the following expression for the maximum wakefield

$$E_c(\text{GV}\cdot\text{m}^{-1}) \approx 4.1 \times 10^4 E_L^{1/4}(\text{J}) (n_e/n_c)^{3/4} (1 - n_e/n_c)^{1/2}. \quad (5.8)$$

Substituting $E_L = 1 \text{ J}$ and $n_e/n_c = 0.03$ in Eq. (5.8) yields $E_c = 2.8 \text{ TV/m}$, which is closer to the value obtained with the simulation. Lastly, in Fig. 5.8(b) we notice that the longitudinal wakefield quickly drops to maximum of around 0.2 TV/m inside the channel, due to the screening effect of K-shell electrons. Moreover, the

massive accumulation of K-shell electrons on the axis results in a defocusing radial wakefield, which significantly differs from that of a classical plasma cavity.

To validate the scaling in Eq. (5.7) and (5.8), in Fig. 5.9 we present the results for $E_L = 1$ J with $n_e = 0.06 n_c$ (first column) and $n_e = 0.18 n_c$ (second column). The top row shows L-shell density snapshots at the iterations where we reach the

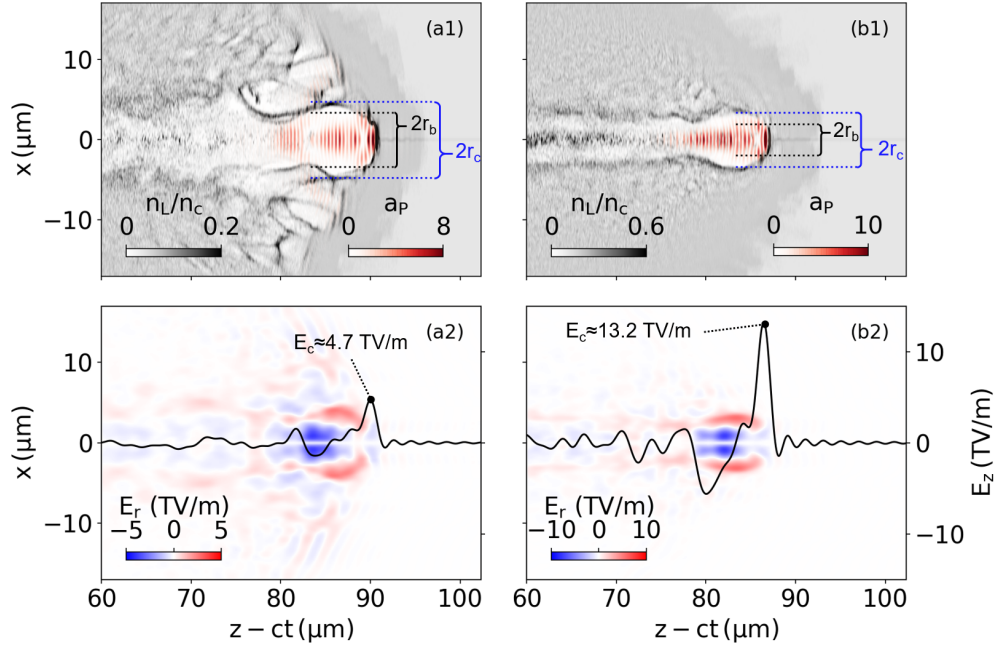


Figure 5.9: Results with $E_L = 1$ J and (a1-2) $n_e = 0.06 n_c$ and (b1-2) $n_e = 0.18 n_c$. (a1, b1) The gray colormap refers to the L-shell electron density, while in red we represent a_p . (a2, b2) Radial wakefield in blue and red, while the black curve refers to the longitudinal wakefield.

maximum wakefield. Here, it is possible to notice that Eq. (5.7) allows to better estimate the maximum channel radius, compared to $r_b = 2\sqrt{a_0}/k_p$. In the bottom row, instead, we illustrate the radial and longitudinal wakefield, which reaches a maximum of around 4.7 TV/m and 13.2 TV/m at $n_e = 0.06 n_c$ and $n_e = 0.18 n_c$ respectively. In the first case, Eq. (5.8) yields 4.6 TV/m, in the second 10 TV/m, proving the good agreement with the numerical results. For completeness, we report the values predicted with Eq. (1.88), namely 3.1 TV/m and 5.3 TV/m for the lower and higher density respectively.

The channel structure we discussed above differs significantly from the cavities observed in *regular* wakefield acceleration. Consequently, one can expect different acceleration mechanisms to be at play. In the following, we will describe the

acceleration processes identified using FBPIC-EWP, namely wakefield acceleration, direct laser acceleration, and ponderomotive acceleration.

Wakefield Acceleration The black curve in Fig. 5.10(a) illustrates an example of Wakefield Acceleration (WA). In this figure, we also depict the plasma density and a_p in the top half and the radial wakefield in the bottom half. In Fig. 5.10(b), instead, we present the wakefield longitudinal work (W_W^z), the laser radial work ($W_L^r = W_L^x + W_L^y$) exerted on the particle in Fig. 5.10(a) and its kinetic energy (E). From Fig. 5.10(a) we notice that the electron is ionized at $z - ct \approx 100 \mu\text{m}$ (i.e.,

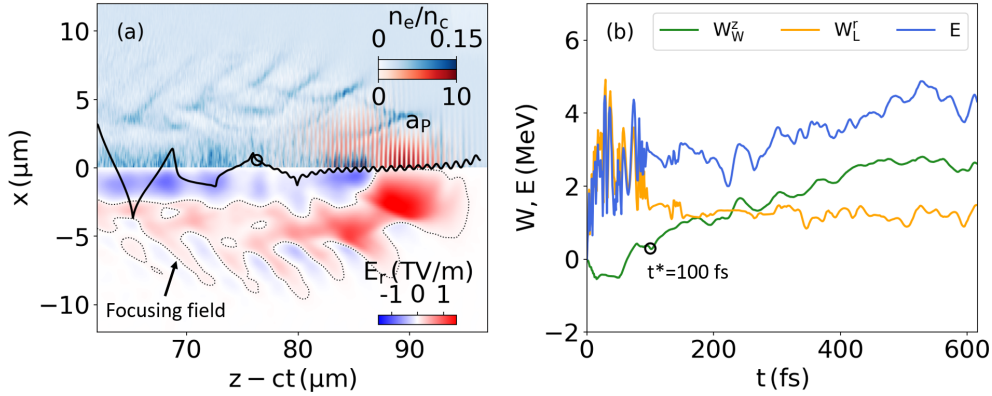


Figure 5.10: (a) Example of one K-shell electron trajectory experiencing wakefield acceleration. (b) Wakefield longitudinal work (W_W^z), laser radial work (W_L^r) and kinetic energy curves (E) for the electron in (a). The circle in (a) refers to the instant $t^* = 100 \text{ fs}$, when the electron leaves the laser pulse and slips into the channel.

$t = 0$ in Fig. 5.10(b)) and it slips through the laser pulse, experiencing $N_{oc} = 24$ optical cycles, before leaving the laser. At this point, namely at $t^* \approx 100 \text{ fs}$ as denoted by the circle in Fig. 5.10(a), the particle has received around 1.47 MeV and -0.28 MeV of radial and longitudinal laser work. While slipping to the back, the electron experiences the accelerating phase of the front ion cavity. The wakefield, indeed, provides 0.75 MeV along the longitudinal direction, while radially it exerts a work of 0.29 MeV. Subsequently (i.e., at $t^* \gtrsim 100 \text{ fs}$), the electron slips into the channel-like structure discussed above, where it performs radial oscillations. Inside this structure, it crosses regions of accelerating wakefield, reaching 4.3 MeV by the end of the simulation. Unlike regular wakefield acceleration, where particles are trapped in phase with the wakefield within an ion cavity, this electron continuously slips through the channel. We estimate that 2.6 MeV and 0.41 MeV of the electron

final energy come from the wakefield longitudinal and radial work respectively, ultimately proving the wakefield central role in accelerating the particle under investigation.

Direct Laser Acceleration In Fig. 5.11 we present an example of Direct Laser Acceleration (DLA). Fig. 5.11(a) shows the trajectory of one K-shell electron that, once ionized at $z - ct \approx 90 \mu\text{m}$, it slips through $N_{oc} = 6$ optical cycles, experiencing a minimum energy gain until $z - ct \approx 85 \mu\text{m}$, namely at $t^* = 55 \text{ fs}$. Here, the electron has acquired $\sim 1.5 \text{ MeV}$ in energy, mostly from the longitudinal wakefield, as underlined in Fig. 5.11(b). At this point, the particle is trapped in the front cavity, where it starts performing oscillations along the laser polarization direction. As discussed in Section 1.2.3, these oscillations can lead to a gain in longitudinal momentum via the $\mathbf{v} \times \mathbf{B}$ term of the laser. Additionally, since the electron is trapped, it also remains in the accelerating phase of the wakefield, which further enhances the electron energy gain. However, in Fig. 5.11(b) we observe that DLA has a more significant role in the electron acceleration process, which reaches $\sim 83 \text{ MeV}$, of which 79 MeV are provided by the laser radial work.

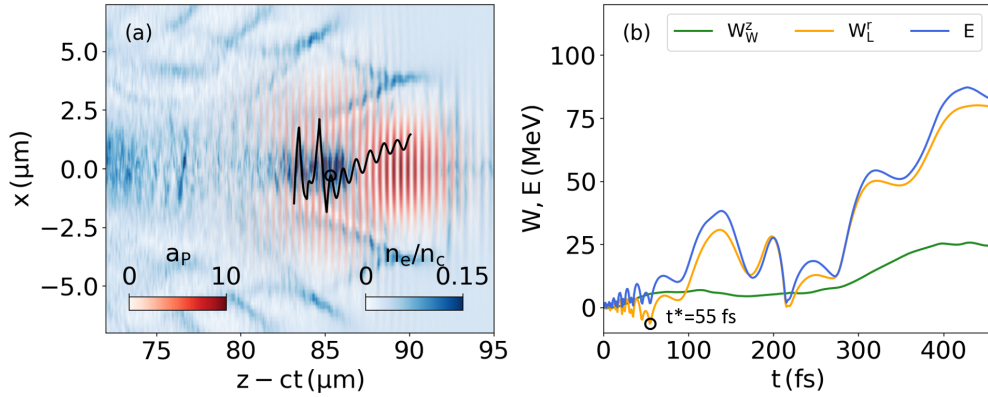


Figure 5.11: (a) Example of one K-shell electron trajectory experiencing direct laser acceleration. (b) Wakefield longitudinal work (W_W^z), laser radial work (W_L^r) and kinetic energy curves (E) for the electron in (a). The circle in (a) refers to the instant $t^* = 55 \text{ fs}$, when the electron is trapped in the front cavity and starts experiencing DLA.

Ponderomotive Acceleration Lastly, Fig. 5.12(a) presents two trajectories of K-shell electrons undergoing ponderomotive acceleration. Considering first the case denoted by the continuous trajectory in Fig. 5.12(a), we estimate that the particle

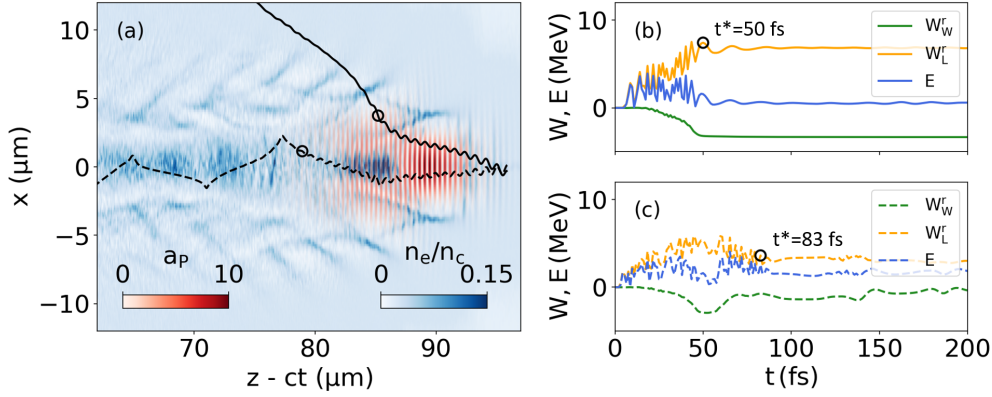


Figure 5.12: (a) Example of two K-shell electron trajectories experiencing ponderomotive acceleration. (b) Wakefield radial work (W_W^r), laser radial work (W_L^r) and kinetic energy curves (E) for the electron denoted by the continuous trajectory in (a). The circle on this trajectory refers to the instant $t^* = 50$ fs, when the electron leaves the laser pulse. (c) Works and kinetic energy for the electron denoted by the dashed trajectory in (a). The circle on this trajectory refers to the instant $t^* = 83$ fs, when the electron leaves the laser pulse.

experiences $N_{oc} = 12$ optical cycles before being expelled by the laser pulse at $t^* = 50$ fs. Similar to what is observed in other acceleration regimes (Thévenet et al., 2016), this sort of dynamics is typical of ponderomotive electrons: they slip through several optical cycles experiencing low energy gains, as shown in Fig. 5.12(b). Here, we show the wakefield and laser radial works (i.e., W_W^r and W_L^r respectively) along with the particle kinetic energy (E). We estimate that the laser provides 6.8 MeV in radial push at $t^* = 50$ MeV. Simultaneously, the electron loses 3.2 MeV crossing regions of space where the focusing radial wakefield opposes the ponderomotive push (i.e., at $z - ct \approx 85 \mu\text{m}$). Concerning the longitudinal dynamics, instead, the numerical analysis underlines that at $t = 22$ fs (i.e., $z - ct \approx 93 \mu\text{m}$) the electron crosses the wakefield decelerating region in the front cavity, causing a 1 MeV loss, while also the laser performs a negative work around 2.1 MeV. Finally, the electron leaves the laser with an energy $E = 0.5$ MeV.

The particle denoted with the dashed trajectory in Fig. 5.12(a) experiences a somewhat similar acceleration process. It slips through the laser field oscillating over $N_{oc} = 21$ optical cycles, before leaving the laser field at $t^* = 83$ fs, as denoted by the circle on the electron trajectory. From Fig. 5.12(c) we deduce that also in this case, the laser provides most of the energy, with a radial push of 2.7 MeV, while the wakefield exerts a pull of 1.1 MeV. Longitudinally, the particle receives 0.7 MeV from the plasma field, since it experiences its accelerating phase at $t = 50$ fs (i.e.,

$z - ct \approx 86 \mu\text{m}$), while the laser performs a negative work of 0.8 MeV. The electron leaves the laser pulse with an energy of $E = 1.5 \text{ MeV}$. Moreover, for $t > 83 \text{ fs}$ we notice that from Fig. 5.12(a) this particle remains closer to the laser axis and is radially trapped in the channel-like structure discussed above. Here, it performs radial oscillations until leaving the channel without a significant difference in energy.

Examples of L-shell Trajectories As previously mentioned, L-shell electrons undergo similar acceleration mechanisms to those of K-shell electrons. In Fig. 5.13(a) we show two examples of L-shell trajectories. In this figure, the continuous tra-

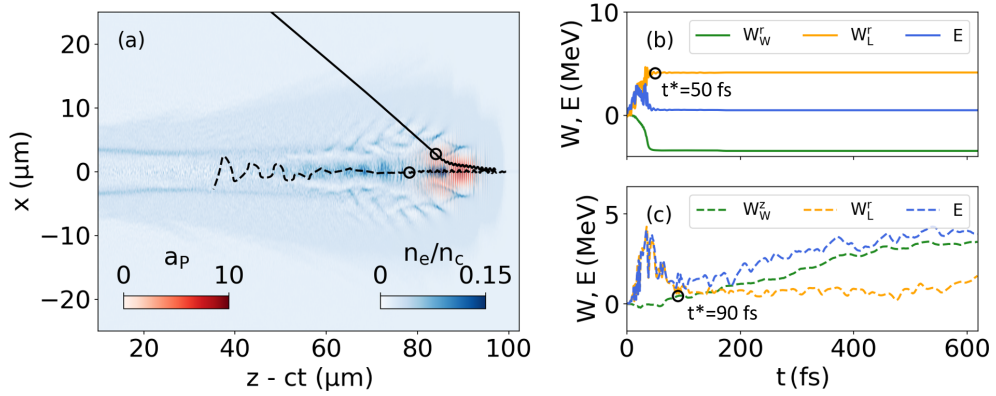


Figure 5.13: Example of two L-shell electron trajectories experiencing (continuous) ponderomotive acceleration and (dashed) wakefield acceleration. (b) Wakefield radial work, laser radial work and kinetic energy of the electron denoted with the continuous trajectory. At $t^* = 50 \text{ fs}$ the electron leaves the laser pulse. (c) Wakefield longitudinal work, laser radial work and kinetic energy of the electron denoted with the dashed trajectory. The electron leaves the laser pulse at $t^* = 90 \text{ fs}$.

jectory refers to an electron experiencing ponderomotive acceleration, exhibiting a behavior similar to the continuous trajectory in Fig. 5.12(a). This particle slips through the laser pulse, traversing $N_{oc} = 14$ optical cycles and it leaves the pulse at $t^* = 50 \text{ fs}$ (i.e., $z - ct \approx 85 \mu\text{m}$). As underlined by Fig. 5.13(b), the laser provides most of the energy to the particles, while the wakefield causes a deceleration in the radial direction, ultimately leaving the electron with an energy of around 0.5 MeV. The dashed trajectory, instead, has a similar dynamics to the dashed trajectory in Fig. 5.12(a). After slipping through $N_{oc} = 28$ optical cycles, the electron starts being accelerated by the wakefield at $t^* = 90 \text{ fs}$, as it is possible to infer from

Fig. 5.13(c). By the end of the simulation, this particle has an energy of around 3.9 MeV.

Statistical Study Having discussed in detail the different acceleration mechanisms, we now wish to present a statistically relevant study on the number of electrons accelerated by the laser and the wakefield. Therefore, for each tracked electron at the instant t , we now define the following parameter

$$\chi(t) = \left| \frac{W_L(t)}{W_W(t)} \right| - 1, \quad (5.9)$$

allowing to compare the laser and plasma work contributions. A positive χ value clearly indicates the laser's central role in driving the electron acceleration process.

In Fig. 5.14(a) we plot the beam angular distribution for both K- and L-shell electrons with $E > 2$ MeV, which can be of interest for industrial applications, such as X-ray tomography. Each electron in the top half of this figure is colored based on its χ value. Thus, we define two criteria for χ and we identify the corresponding electron populations. In the range $-1 \leq \chi < 0$ we find yellow electrons that gain most of their energy through wakefield acceleration, displaying trajectories as those discussed above. The red particles, instead, have $\chi \geq 0$ and are primarily accelerated by the laser. In this population, we find ponderomotive electrons, displaying dynamics similar to the two examples in Fig. 5.12(a). As discussed below, some of the red electrons can also experience direct laser acceleration. We estimate that around 60 % of the particles exhibit positive values of χ , proving the laser as the primary driver in particle acceleration. In the bottom half of Fig. 5.14(a), instead, the color represents the energy of each particle. The average energy for $E > 2$ MeV is around 9 MeV for both yellow and red electrons, and we notice a concentration of higher energies closer to the laser axis, which is consistent with the experimental results presented in Chapter 4. For instance, if we consider a solid angle of 0.25 sr (white circle in Fig. 5.14(a)), the average energy increases to 14 MeV.

Fig. 5.14(b) depicts the $(z - ct, E)$ phase space of red and yellow K-shell electrons. This figure underlines the different behaviors of red electrons. As previously mentioned, in this population we find particles undergoing ponderomotive acceleration. We estimate that around 85 % of red K-shell electrons gain up to $m_e c^2 a_{p,max} \approx 8$ MeV through the ponderomotive push (see Eq. (1.52)). Here, $a_{p,max} \approx 16$ is the maximum laser normalized vector potential in plasma. Instead, the remaining 15 % experiences direct laser acceleration, allowing these particles to reach 10s – 100s MeV. In Fig. 5.14(b) we also recognize yellow K-shell electrons. The trajectories of these particles display the behavior discussed in the example

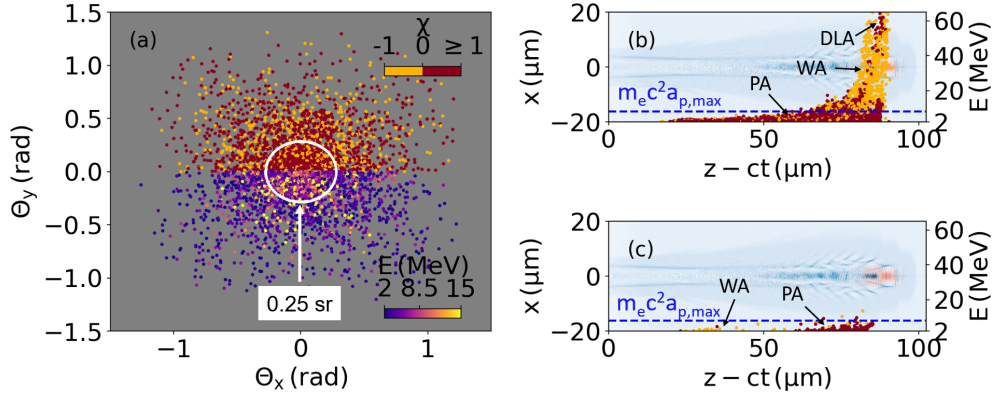


Figure 5.14: (a) Electron angular distribution. In the top half, the color refers to the parameter χ (see text), while in the bottom half, it represents the energy. The white circle represents a solid angle of 0.25 sr (see text). $(z - ct, E)$ phase space for (b) K-shell electrons and (c) L-shell electrons. For visual reference, we show the plasma density and laser intensity.

of Fig. 5.10(a), undergoing wakefield acceleration. In other instances, similar to DLA electrons, we find yellow K-shell electrons trapped in the front ion cavity via ionization injection. These particles remain in phase with the wakefield long enough to reach 10s – 100s MeV. Analogously, Fig. 5.14(c) displays the $(z - ct, E)$ phase space of red and yellow L-shell electrons. We estimate that around 83 % of L-shell electrons undergo PA, while the remaining fraction is mainly accelerated via WA while momentarily crossing the longitudinal wakefield accelerating phase.

5.2.4 Charge-per-Joule Saturation Effect

In this section, we provide a possible explanation to the charge-per-Joule saturation effect observed in Chapter 4, employing the configurations presented in the previous section.

In Fig. 5.15(a), the colormap illustrates the charge-per-Joule ($Q_{/J}$) derived from linearly interpolated numerical results. Here, we consider all electrons (i.e., within a 4π sr solid angle) with a minimum energy $E = 2$ MeV, coherent with the discussion in Section 5.2.3. The white dashed lines, instead, are charge-per-Joule isolines. From Fig. 5.15(a) it is possible to notice that for $E_L \gtrsim 0.12$ J and $n_e \gtrsim 0.03 n_c$ the charge-per-Joule slowly increases from 40 nC/J to ~ 50 nC/J with the laser energy. This region is outlined by black dotted lines for visual reference. Moreover, within this range, we observe that increasing the plasma density at a

fixed laser energy does not result in significantly higher charges-per-Joule. This saturation effect is attributed to the saturation of the energy conversion efficiency (η) with respect to plasma density. Here, η is defined as the ratio of the electrons' kinetic energy to the laser energy. In other words, regardless of variations in plasma density, the same amount of laser energy ionizes and allows to accelerate the same number of electrons at the same average energy. This analysis is corroborated by the energy spectra in Fig. 5.15(b), where we consider electrons with energies in the range $2 \text{ MeV} < E < 15 \text{ MeV}$, comprising over 80 % of the charge with energy $E > 2 \text{ MeV}$ (i.e., the range we considered in Fig. 5.15(a)). In Fig. 5.15(b), we notice that the curves at $E_L = 1 \text{ J}$ for $n_e = 0.03 n_c$ and $n_e = 0.06 n_c$ superimpose, presenting an average energy around 4.7 MeV. For these configurations, we estimate the efficiency to be $\eta \sim 21 \%$. A similar behavior is also observed at $E_L = 0.12 \text{ J}$, where we estimate the average energy to be 5.7 MeV and the conversion efficiency is $\eta \sim 18 \%$ for both densities.

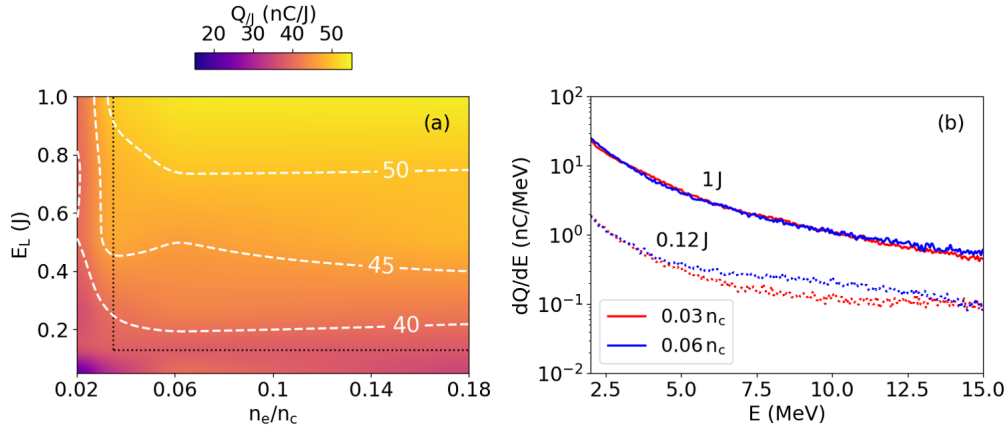


Figure 5.15: Charge-per-Joule for the different configurations of interest, for electrons exceeding $E > 2 \text{ MeV}$. The colormap is the linear interpolation of the simulations, while the white dashed lines refer to constant values of the charge-per-Joule. The black dotted lines highlight the region of charge-per-Joule saturation. (b) Examples of energy spectra. The continuous lines refer to the case at $E_L = 1 \text{ J}$ for $n_e = 0.03 n_c$ and $n_e = 0.06 n_c$. The dotted curves refer to the case at $E_L = 0.12 \text{ J}$ at $n_e = 0.03 n_c$ and $n_e = 0.06 n_c$.

The curves in Fig 5.16 illustrate the electrons' kinetic energy dynamics (i.e., dE/dz), considering 1 J laser energy and three different plasma densities. The integral of each curve amounts to the laser energy spent for ionizing and accelerating the electrons with $2 \text{ MeV} < E < 15 \text{ MeV}$. From Fig 5.16, we deduce that increasing the plasma density results in a contraction of the characteristic length of

each curve, as indicated by the shift in the position of their maxima. We estimate this characteristic length to correspond to approximately $L_{pd}/2$, namely the pump depletion length we discussed in Fig. 5.6, scaling as n_e^{-1} . Simultaneously, we notice that at higher plasma densities the electrons' energy gain rate (i.e., the maximum of each curve) increases. Thus, despite the curve contraction experienced at higher densities, a faster energy gain ultimately results in the same integral for all curves, namely ~ 0.21 J, consistently with the conversion efficiency saturation effect.

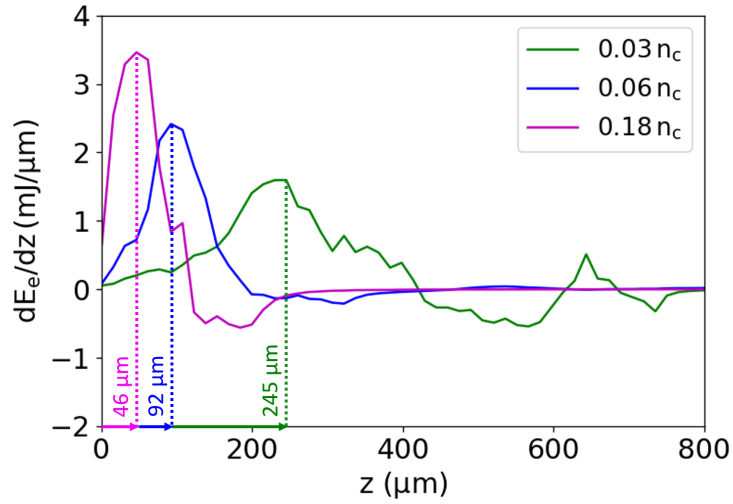


Figure 5.16: Electron energy gain dynamics for $n_e = 0.03 n_c$, $n_e = 0.06 n_c$ and $n_e = 0.18 n_c$ at $E_L = 1$ J. From these curves, we estimate that the laser energy spent for ionizing and accelerating the electrons between 2 MeV and 15 MeV is around 0.21 J for the three densities, explaining the saturation effect in Fig 5.15(a).

5.3 Numerical Simulations: Experimental Conditions

The numerical study discussed thus far highlighted the physics at play, specifically pertaining to the electron acceleration mechanisms. Now, we intend to briefly discuss a set of FBPIC simulations performed in conditions more similar to the experimental ones. This, in turn, will allow for a better understanding and interpretation of the experimental results.

In this last section, we first start by presenting the numerical configuration adopted for this set of simulations. Following this, we explore the laser diffraction and plasma density structures, comparing one configuration of interest with what we have observed in Section 5.2.2. Specifically, here, we present a detailed analysis of the simulation results obtained at $n_e = 0.05 n_c$ and $E_L = 0.1 \text{ J}$, which allowed to reach the highest charge-per-Joule with the 0.4 mm nozzle (see Sec. 4.2.2). To better characterize the electron beam produced with this configuration, we conclude this section by discussing the beam charge average energy and divergence.

5.3.1 Simulation Setup

Fig. 5.17 is a schematic representation of the setup employed for the simulations of this section. In this case, we consider a 30 fs Gaussian laser pulse with $\lambda_0 = 800 \text{ nm}$, $w_0 = 3 \mu\text{m}$ and with energies ranging from 0.05 J and 0.8 J. Thus, the laser intensity peak is varied between $1.1 \times 10^{19} \text{ W/cm}^{-2}$ and $1.8 \times 10^{20} \text{ W/cm}^{-2}$, corresponding to $a_0 \in [2.3, 9.1]$. The laser is focused at $z = 0$, namely at the peak of a Lorentzian plasma density profile (gray surface), which was obtained by fitting the measured plasma density produced with the 0.4 mm nozzle (blue curve). The peak plasma density ranges between $n_e = 0.01 n_c$ and $n_e = 0.05 n_c$, coherent with the experimental configuration.

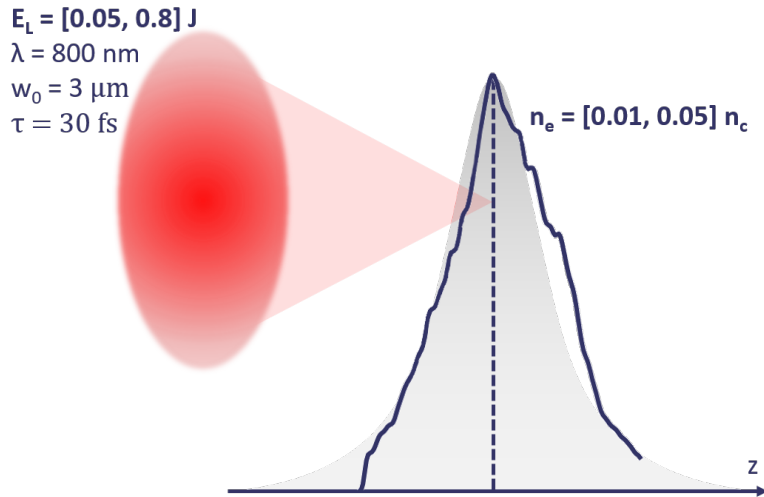


Figure 5.17: Schematic representation of FBPIC simulations in the experimental conditions.

5.3.2 Laser Diffraction and Plasma Structures

As previously mentioned, in this section, we provide a detailed analysis of the simulation at $n_e = 0.05 n_c$ and $E_L = 0.1 \text{ J}$. For this case, quantities such as the plasma wavelength and critical power are calculated with respect to the plasma density peak.

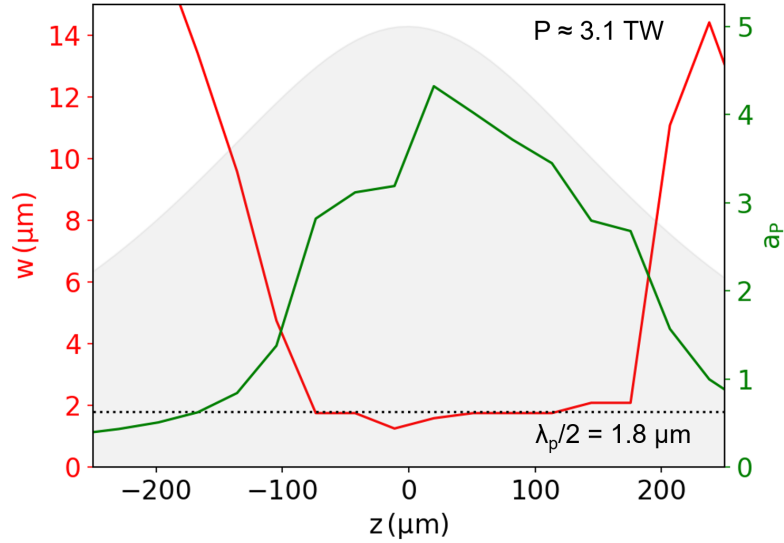


Figure 5.18: Beam waist and normalized vector potential in plasma for $n_e = 0.05 n_c$ and $E_L = 1 \text{ J}$. The horizontal dotted line refers to $\lambda_p/2 = 1.8 \mu\text{m}$. For reference, we also illustrate the plasma density (gray area).

Following a similar approach to that of Section 5.2.2, in Fig. 5.18 we illustrate the beam spot size (red curve) and the normalized laser vector potential in plasma (green). We also plot the plasma density profile (gray-shaded area) for visual reference. Also in this case, we notice that the laser experiences self-focusing, since its power $P \approx 3.1 \text{ TW}$ significantly exceeds the critical power $P_c = 350 \text{ GW}$. Specifically, we observe that the waist is focused down to $\lambda_p/2$ at $z \approx -100 \mu\text{m}$, where $\lambda_p = 3.6 \mu\text{m}$. Subsequently, the laser pulse remains focused down to $\lambda_p/2$ for a total length of around $L \approx 10Z_R$, where we recall that in this case $Z_R = 30 \mu\text{m}$. In this figure, we notice that the maximum vector potential reaches $a_{P,max} = 4.4$ at around $z = 30 \mu\text{m}$, exceeding the vacuum maximum value, namely $a_0 = 3.7$. Using Eq. (5.4) we predict $a_{P,max} = 6$ considering $n_e = 0.05 n_c$ and $E_L = 0.1 \text{ J}$, which is around 50% more than the value obtained with the simulation. We believe that the discrepancy is partially due to the energy loss experienced by the laser in the plasma profile tail leading to the density peak. Indeed, at $z = 30 \mu\text{m}$,

where the laser normalized vector potential reaches its maximum, we estimate that the laser has lost around 30% of its initial energy (i.e., $E_L = 0.07$ J). Considering $n_e = 0.05 n_c$ and $E_L = 0.07$ J we yield $a_{P,max} = 5$ with Eq. (5.4), which is in better agreement with the numerical results.

Fig. 5.19(1 – 4) illustrates an evolution of the plasma structures. Similar to Section 5.2.3, we distinguish K- and L-shell electrons with a green and gray colormap respectively, while the laser is denoted with a red colormap. Initially,

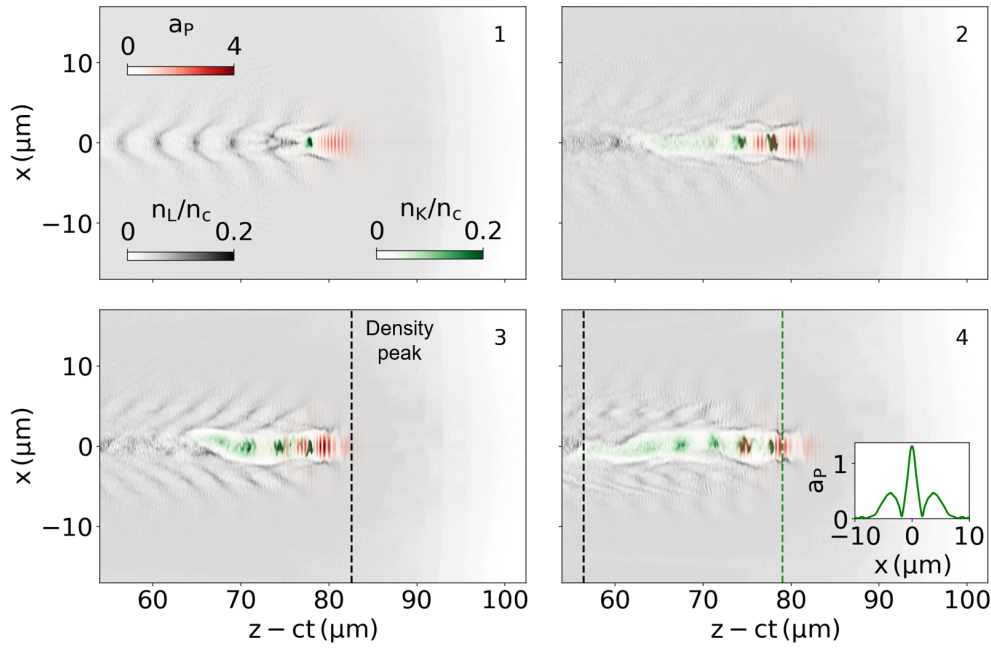


Figure 5.19: (1 – 4) Plasma density snapshots of four consecutive iterations. The gray and green colormaps refer to the L- and K-shell electron density. In red we depict a_P . Similar to the idealized case, these panels highlight the generation of a channel-like structure. The inset in (4) depicts the laser transverse profile along the green dashed line. The black dashed line is a visual reference for the plasma density peak.

the laser propagates in the plasma up-ramp, where it excites multiple longitudinal oscillations and nitrogen experiences a limited K-shell depletion (1), since $a_P \lesssim 1.5$, the K-shell ionization threshold. At this point, we can clearly distinguish different plasma cavities formed by L-shell electrons. As the pulse gets closer to the density peak, it experiences self-focusing and it reaches intensities allowing for a more significant K-shell ionization. These particles are ionized close to the laser axis, where we presume they accumulate within the plasma cavities through

ionization injection (Guillaume et al., 2015), forming a train of electron bunches. The continuous ionization and accumulation of K-shell electrons on axis ultimately lead these cavities to merge, generating a massive L-shell sheath surrounding K-shell electrons (2 – 3), which can partially screen the wakefield, similar to what we described in Section 5.2.3. Compared to the idealized case, however, the more prominent K-shell density modulation along the longitudinal direction leads to the formation of cavities and the generation of a longitudinal wakefield, which we will discuss in the following. We estimate the L-shell channel length to be around $L = 26 \mu\text{m}$, corresponding to $\sim 7\lambda_p$ (4). Lastly, in the inset of Fig. 5.19(4) we also plot the laser transverse profile along the green dashed line. Thus, coherent with our prior analysis, the laser still presents sidelobes, highlighting the occurrence of beam-breakup (Thomas et al., 2007).

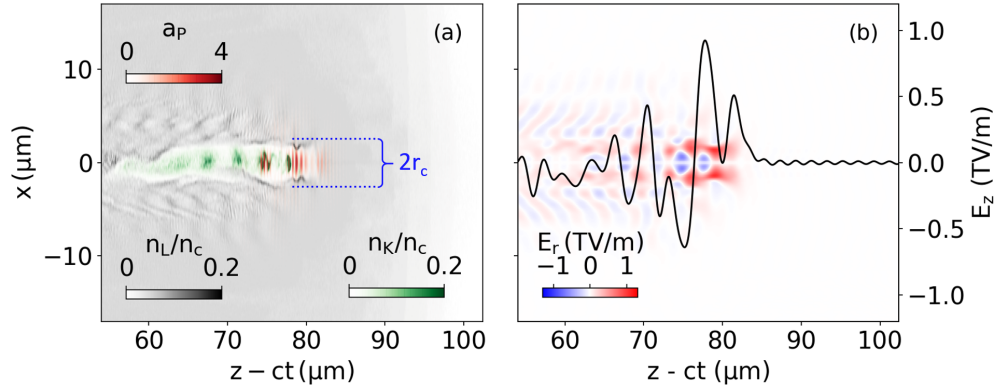


Figure 5.20: (a) Plasma density snapshot of the last panel of Fig. 5.19. The gray colormap refers to L-shell electrons, the green to K-shell electrons and the red one refers to the laser. (b) Radial wakefield map (E_r) and longitudinal wakefield (E_z) corresponding to the snapshot shown in (a).

In Fig. 5.20(a) we present the last panel of Fig. 5.19. Here, we notice that the maximum channel radius $r_c = 2.56 \mu\text{m}$ calculated with Eq. (5.7) assuming $n_e = 0.05 n_c$ and $E_L = 0.07 \text{ J}$ is in good agreement with the simulation. Moreover, as mentioned above, in Fig. 5.20(a) we observe a more prominent K-shell density modulation along the longitudinal direction compared to the idealized case. This is due to the initial moderate injection of K-shell electrons in the L-shell cavities formed in the plasma up-ramp, which leaves these particles equally spaced. Consequently, this K-shell modulation allows for the generation of plasma cavities, whose radial sheath is formed by L-shell electrons. Longitudinally, instead, the sheath is provided by K-shell electrons. Thus, inside the channel, we find a longitudinal wakefield which is not dumped as in the idealized case, as underlined in

Fig. 5.20(b). In this figure, the black curve refers to the longitudinal wakefield (i.e., E_z), while the red and blue colormap represents the radial wakefield (i.e., E_r).

5.3.3 Beam Properties

For completeness, we conclude this chapter by illustrating some properties of the electron beam in the configuration of interest, namely for $n_e = 0.05 n_c$ and $E_L = 0.1$ J.

In Fig. 5.21(a) we present the beam angular distribution for electrons with energy $E > 0.5$ MeV, within a solid angle of ~ 1.7 sr. Each electron is colored based on its energy at the last simulation iteration. In these conditions, we estimate a beam charge of around 5 nC. If we limit the solid angle to 0.25 sr, coherent with the BPM, the beam charge drops to 2.3 nC, which is close to the experimental measurement (i.e., 2.5 ± 0.11 nC). From Fig. 5.21(a) we estimate the beam FWHM divergence to be 76 mrad, while experimentally we estimate only around 50 mrad. We presume that the higher divergence obtained with the simulation is due to a higher concentration of electrons along the laser polarization direction. Furthermore, it is possible to observe that closer to the laser axis we find high energy electrons, coherent with Section 5.2.3. In Fig. 5.21(b), we show the $(z - ct, E)$ phase space. In this case, the color of each particle is based on its emission angle, defined as $\Theta_r = (\Theta_x^2 + \Theta_y^2)^{1/2}$. Thus, we further prove that electrons at higher

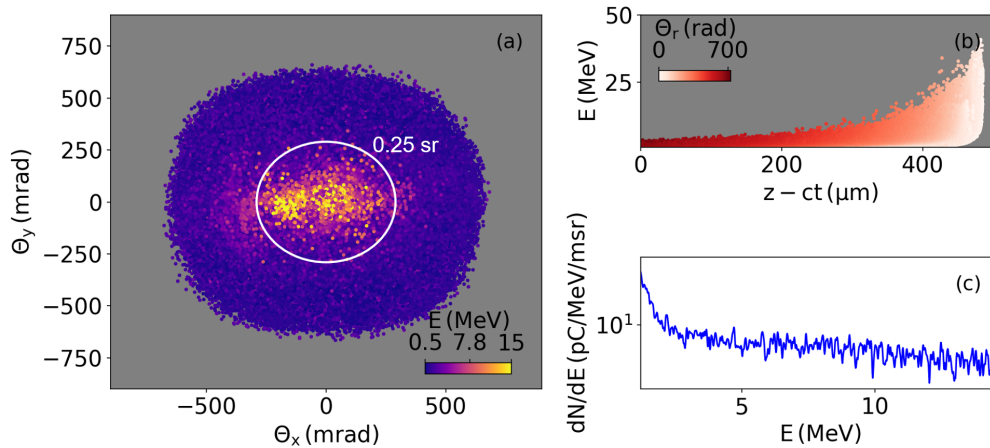


Figure 5.21: (a) Electron angular distribution. Each particle is colored based on its energy. (a) $(z - ct, E)$ phase space. The color of each electron refers to its radial divergence Θ_r (see text). (c) Electron beam energy spectrum. The white circle refers to a solid angle of 0.25 sr (see text).

energy are less divergent than those less energetic. In Fig. 5.21(c) we plot the beam energy spectrum between $E = 1.2$ MeV and $E = 14.7$ MeV, considering electrons in a ~ 1.2 msr solid angle, coherent with the spectrometer pinhole collecting angle. Thus, we notice that the spectrum follows a quasi-Maxwellian distribution, similar to the experimental results of Chapter 4. Within this energy range, we estimate the average energy to be 4.5 MeV and the conversion efficiency is around $\eta = 10\%$. Under these conditions, we experimentally measured an average energy of 4.3 ± 0.26 MeV and $\eta \approx 5.4\%$. The difference between the numerical and experimental values of the conversion efficiency is due to the laser energy considered for the calculation. Since the laser pulse in experiment is not perfect, a significant part of the energy lies out of the central spot, which contains $\sim 57\%$ of the total laser energy. Thus, the total laser energy on target in this case is ~ 0.2 J and with this value we obtain $\eta \approx 5.4\%$. If we considered, instead, the energy in the laser central spot (i.e., $E_L \approx 0.1$ J), the experimental value would rise to $\eta = 9.4\%$, which is in better agreement with the simulation that indicates what could be obtained with a perfect laser.

5.4 Conclusion

In this chapter, we have presented a detailed numerical study through two sets of FBPIC simulations. We have first explored the interaction between a superintense laser pulse and a nitrogen plasma plateau with $n_e \gtrsim 0.02 n_c$. Similar to previous studies, our analysis highlights the occurrence of beam-breakup initiated by self-focusing, which also enables the laser pulse to be focused down to approximately $\sim \lambda_p/2$. Furthermore, we demonstrate that this tight focusing in plasma results in laser normalized vector potentials up to three times higher than those in a vacuum. From these observations, we are able to deduce scaling laws, allowing to better understand the regime of interest.

We subsequently explore the different acceleration mechanisms. First, we illustrate the different plasma structures and we discuss the generation of a massive L-shell channel-like structure, surrounding K-shell electrons. The accumulation of K-shell electrons on the laser axis screens the longitudinal wakefield, leading to a scenario notably different from classical wakefield acceleration.

Through the code FBPIC-EWP, we analyze the numerical simulations and we calculate the work performed by both the laser and the plasma electric fields. Through this detailed study, we identify three acceleration mechanisms: ponderomotive acceleration, wakefield acceleration and direct laser acceleration. Among these, we find that ponderomotive acceleration is the most prevalent process. This first set of simulations also allows us to provide an explanation to the charge-per-

Joule saturation with the plasma density, which we have observed in Chapter 4. Specifically, we prove that regardless of variations in plasma density, the same amount of laser energy ionizes and allows to accelerate the same number of electrons at the same average energy.

Finally, we conclude this chapter illustrating an example of FBPIC simulation performed in the experimental conditions. Thus, in this last section, we explore the laser diffraction and plasma density structures, comparing this case with the idealized case. Moreover, we employ and verify the scaling laws deduced in the first section of this chapter.

Conclusion and Outlook

Overview of Main Results

In this work, we have presented a laser-plasma interaction regime allowing to increase the average electron beam current, particularly in the range of a few MeV. These electron beams can be valuable for low-energy applications that do not necessarily require high-quality, monoenergetic beams, such as industrial X-ray tomography ([Multiscan 3D project, 2020](#)).

Our research activity addressed various aspects, including the development of gas targets and specific diagnostics used for the experimental campaign. In Chapter 3, we presented a study that resulted in the production of a sub-millimetric supersonic nozzle in collaboration with the FTMC laboratory in Lithuania. Additionally, we detailed the creation of magnetic dipoles, essential for measuring few-MeV electron energy spectra. We concluded this chapter by introducing a novel energy spectrometer developed with Vacuumschmelze, which enables the measurement of highly divergent, few-MeV electron beams, representing an improvement over current spectrometry techniques. Chapter 4 was devoted to the experimental findings of this work. Using the 60 TW Salle Jaune laser system of the Laboratoire d'Optique Appliquée, we conducted a parametric study, employing different plasma densities, laser energies, gas targets, and degrees of focusing. This led us to identify the conditions for producing highly divergent electron beams (i.e., > 100 mrad), with energies of a few MeV, charges of 5 to 30 nC, and a maximum laser-to-electron energy conversion efficiency of about 14 %, one of the highest ever measured.

The work of this thesis also involved Particle-In-Cell simulations, enabling an in-depth study of the physics in the regime we explored. The numerical study presented in Chapter 5 allowed us to identify the main phenomena concerning laser diffraction and we were able to determine scaling laws. Using a numerical tool specifically developed for processing PIC simulation results, we proved that most electrons are accelerated by the laser's ponderomotive force. Notably, we observe

that the majority of particles are not injected into the plasma waves but rather slide on the laser pulse, gaining just a few MeVs.

Perspectives

Industrial 3D X-ray Tomography Given current 10 W laser systems, the regime we explored opens pathways for generating laser-plasma accelerated electron beams with average currents approaching $1 \mu\text{A}$, surpassing the current state of the art by three orders of magnitude. Recent advancements in laser technology (Pellegrina et al., 2022, Kiani et al., 2023) suggest the upcoming development of $\sim 100 \text{ W}$ laser systems, which could potentially lead to the attainment of unprecedented average currents exceeding the μA -level. With such capabilities, this electron source emerges as a promising candidate for various applications requiring few-MeV electrons, as previously mentioned.

In Fig. 5.22(a) we present an example of X-ray tomography, performed using the 10 TW Salle Sheril laser system at LOA, capable of delivering $\sim 0.35 \text{ J}$, 40 fs laser pulses. The driver laser pulse is focused down to $w_0 \approx 3 \mu\text{m}$ using an $f/6$ off-axis parabola on a pure nitrogen gas jet, produced with a 2 mm exit diameter supersonic nozzle. In this case, we estimate the peak plasma density to be $n_e = 0.02 n_c$. The produced electron beam subsequently interacts with a 1 mm thick tungsten conversion plate, generating X-rays via bremsstrahlung. These X-rays allow to realize a radiography of an inox specimen with a defect, using an imaging plate. In Fig. 5.22(b) we illustrate the radiography, where it is possible to notice a fracture with an estimated characteristic width of less than 1 mm.

While promising, these results indicate that the produced beams and the setup itself may still require further improvement. As it is possible to notice from Fig. 5.22(a), for instance, the tungsten conversion plate has been ablated by the laser, which retains a sufficiently high intensity upon exiting the plasma. Using a secondary gas jet could facilitate further laser pulse depletion, thus preventing damage to the conversion plate.

For certain industrial applications, it is also crucial to control the maximum electron energy to prevent the activation of materials. Certain country regulations (U.S. Food and Drug Administration, 1977) set the maximum allowed electron energy at approximately 10 MeV for specific applications involving X-rays, as higher energies could pose a public hazard. Nonetheless, both the experimental and numerical studies of this work proved the presence of electrons exceeding several tens-MeV. Thus, addressing this issue is of utmost importance for the successful use of laser-plasma-based accelerators for such applications. Thanks to the detailed

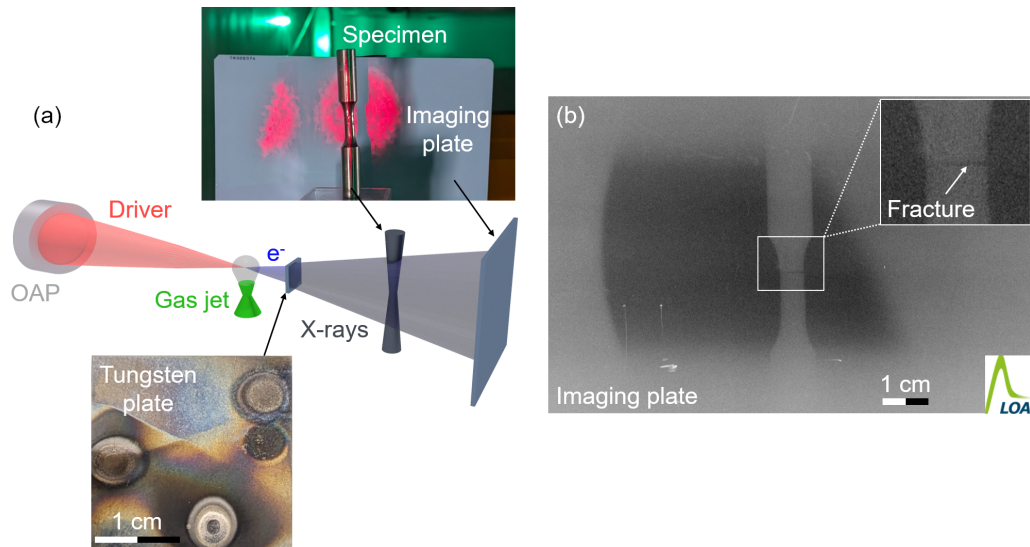


Figure 5.22: (a) Salle Sheril experimental setup for bremsstrahlung X-ray generation. The tungsten plate is positioned at ~ 2 cm from the nozzle, the specimen at 40 cm and the imaging plate at 50 cm. (b) Resulting X-ray imaging plate tomography.

numerical analysis provided in this thesis, it has been possible to identify the main acceleration mechanisms. Specifically, the results suggest that completely suppressing electron trapping could mitigate the mechanisms responsible for accelerating electrons above 10 MeV. Indeed, once injected, these particles can be accelerated to high energies by the wakefield or through direct laser acceleration, reaching energies around 100 MeV.

Limiting the beam maximum divergence can also be important for certain applications. As proved by the experimental results, while increasing the laser energy allows to reach higher charges it also yields more divergent electrons, which can be difficult to collect or use. This, in turn, leads to a decrease in the charge-per-Joule and conversion efficiency. One possible approach to limit beam divergence is to use a lower energy pulse. However, this naturally leads to a decrease in electron beam charge. Alternatively, it is possible to employ a train of two laser pulses, spaced by a delay ranging from three to thirty times the plasma period ([Andriyash et al., 2024](#)). This technique can produce the same amount of charge as a single pulse. By splitting the laser into two pulses, the divergence of the electron beams produced by each pulse is reduced, since each pulse in the train carries only half the energy of the single pulse.

Appendix A

FBPIC Simulation Setup

Once we have defined the main numerical parameters regarding this example, it is necessary to define the `Simulation` object to run an FBPIC simulation, as shown below. This object encapsulates the parameters we have discussed above. More specifically, it is possible to observe the number of longitudinal (N_z) and radial (N_r) points of the co-moving window, naturally related to the meshing we have presented. Here, z_{\max} (z_{\min}) represent the maximum (minimum) box longitudinal coordinate, while N_m is the number of spectral modes. The `Simulation` object also allows to define the charge profile distribution (`particle_shape`) that it has been set to be `cubic` for the best available resolution. The boundary conditions have been set to be `open` in both directions, while the `current_correction` parameter represents the method used to satisfy the continuity equation. For the simulations of this chapter, we have chosen the `cross-deposition` method, i.e., the most precise available in FBPIC. Finally, we mention for completeness the `n_order` and `use_cuda` parameters. The first defines the number of stencils for z derivatives in the Maxwell solver, while the second allows to use the GPU parallelization.

```
1 sim = Simulation( Nz, zmax, Nr, rmax, Nm, dt,
  → zmin=zmin,
2     n_order = 16, use_cuda = True,
3     particle_shape = 'cubic',
4     boundaries = {'z':'open', 'r':'open'},
5     current_correction='cross-deposition' )
```

After defining the `Simulation` object in the FBPIC input file, we can introduce the nitrogen atoms. Below, we present the input file lines related to the whole definition of the nitrogen gas and the corresponding electron species we aim to study. As it is possible to observe, we can add the nitrogen atoms to the

Simulation object via the `add_new_species` method. The main parameters of this method are `p_nz`, `p_nr` and `p_nt` that represent the number of macroparticles per cell in the z , r and θ direction respectively. Instead, `n` represents the density of the specific species, while `dens_func` is the normalized function describing the density profile. Hence, here we also introduce all the different electron species, namely `elec_L3`, `elec_L`, `elec_K6` and `elec_K7`. The first two relate to the L-shell electrons, while the last two refer to the K-shell. Therefore, we use the dictionary `target_species` that allows us to store the ionized electrons. Each dictionary key is an integer between 0 and 6 representing the corresponding ionization level. Finally, we introduce nitrogen ionization via the `make_ionizable` method that employs the ADK model (Chen et al., 2013), as previously mentioned. The `make_ionizable` method has the `target_species` as input parameter and also the `level_start`, necessary to define the plasma pre-ionization degree.

```

1 # Add the nitrogen atoms
2 atoms_N = sim.add_new_species( q=5*e, m=14.*m_p, n=n_e
   ↪ / 5,
3     dens_func=dens_func, p_nz=1, p_nr=1, p_nt=4,
   ↪ p_zmin=p_zmin, p_zmax=p_zmax, p_rmax=p_rmax )
4
5 # Create the N-electrons and make nitrogen ionizable
6 target_species = {}
7 elec_L3 = sim.add_new_species( q=-e, m=m_e, n=3*n_e/5,
8     dens_func=dens_func, p_nz=p_nz, p_nr=p_nr, p_nt=p_nt,
   ↪ p_zmin=p_zmin, p_zmax=p_zmax, p_rmax=p_rmax )
9 elec_L = sim.add_new_species( q=-e, m=m_e )
10 elec_K6 = sim.add_new_species( q=-e, m=m_e )
11 elec_K7 = sim.add_new_species( q=-e, m=m_e )
12
13 for i_level in range(0, 3) :
14     target_species[i_level] = elec_L3
15 for i_level in range(3, 5) :
16     target_species[i_level] = elec_L
17
18 target_species[5] = elec_K6
19 target_species[6] = elec_K7
20
21 atoms_N.make_ionizable( 'N',
   ↪ target_species=target_species, level_start=3 )

```

Appendix B

List of Figures

1	Examples of laser-plasma-based betatron computed tomographies. (a) A Chrysopa. Each inset refers to a tomographic slice along the dashed arrows. <i>Figure adapted from Svendsen et al. (2018)</i> . (b) Tomographic slice of a mouse embryo. <i>Figure adapted from Cole et al. (2018)</i>	2
2	Multiscan 3D project conceptual design. A rectangular frame hosts multiple laser-plasma-based bremsstrahlung sources and the X-ray detector. Each source is reached by a laser pulse, allowing to generate an electron beam. (Inset) Schematic representation of a laser-plasma X-ray source.	3
1.1	Field calculation at the position P, assuming $\tilde{E}(x_0, y_0, z_0)$ to be known. <i>The image has been adapted from Svelto (2010)</i>	7
1.2	Illustration of the characteristic Gaussian beam parameters. <i>The image has been adapted from Svelto (2010)</i>	9
1.3	Depiction of the electric field E and its envelope E_{env} . Here, we have assumed a time duration $\tau_e \sim 30$ fs and $\lambda = 0.8 \mu\text{m}$	11
1.4	Depiction of the atomic Coulomb potential in the presence of a strong-field. Φ_p denotes the actual bonding potential (a) Unperturbed atom potential. (b) Multi-photon ionization. (c) Tunnel ionization. (d) Barrier suppression Ionization. <i>The image has been adapted from Hansen (2012)</i>	12

- 1.5 Numerical example of relativistic self-focusing obtained using the code FBPIC (Lehe et al., 2016). The blue and green curves represent the laser spot-size propagating in plasma and in vacuum respectively. The gray-shaded area is the normalized plasma density profile. For visual purposes, we plot $w/w_0 - 1$, and the horizontal dotted line represents the condition $w = w_0$. The laser is initially defined in vacuum at $z \approx -1200 \mu\text{m}$ and it is focused at $z = 0$, where $n_e = 3.6 \times 10^{19} \text{cm}^{-3}$. The laser parameters are $\tau_0 = 30 \text{fs}$, $\lambda = 0.8 \mu\text{m}$ and $a_0 = 3.8$ 20
- 1.6 Linear regime quantities: (a) Normalized longitudinal wakefield E_ζ/E_0 , (b) normalized radial wakefield E_r/E_0 and (c) normalized plasma density oscillation $\delta n/n_0$ 23
- 1.7 FBPIC non-linear wakefield quantities obtained with a 30-fs laser for $a_0 \approx 2$ and with a plasma density $n_0 = 1.2 \times 10^{19} \text{cm}^{-3}$. Here, a is the normalized laser amplitude, ϕ and E_z/E_0 are the normalized wakefield potential and electric field. We plot the normalized plasma density as $\delta n/n_0 - 1$ for visual purposes. 25
- 1.8 Trajectories in phase space obtained using Eq. (1.79) and the numerical example of Fig. 1.7. The black line represents the orbit of non-injected electrons, the red one the separatrix and the blue dashed lines the trapped orbits. 27
- 1.9 (a) FBPIC simulation of the bubble regime. The laser pulse is propagating from left to right. Here, the color map represents the normalized plasma density variation $\delta n/n_e$ and $\xi = z - v_g t$. *Figure from Oubrerie (2022)*. (b) Schematic representation of the electron sheath and trapped electrons (green dots) on the top of the image and the longitudinal electric field E_z on the bottom. 29
- 1.10 Schematics of the transverse injection for different electron transverse positions. For $|x| \gtrsim r_b$ and $|x| \lesssim r_b$ it is not possible for the electrons to be injected. For $|x| \approx r_b$ the electrons can be injected because of wavebreaking. The rapid expansion of the cavity (orange circle) facilitates the whole injection process. 30
- 1.11 PIC simulation displaying the (a) longitudinal and (b) transverse self-injection mechanism. The red and blue colormaps relate to the laser intensity and plasma density. The green lines represent the electron trajectories. *Figure from Corde et al. (2013b)*. 32
- 1.12 Nitrogen ionization rate (colored curves) for a laser (red area) with $a_0 \approx 2.2$ that propagates toward the right. 33

1.13	Schematic representation of the ionization injection mechanism for electrons born in front of the laser pulse (purple curves) and in the middle (green curve).	34
1.14	2D EPOCH (Arber et al., 2015) simulation. Here the laser pulse with $a_0 = 8.5$ interacts with a plasma density plateau at $n_e = 10^{19} \text{ cm}^{-3}$ and it fills the whole window. (top) Normalized plasma density profile $\langle n_e \rangle / n_c$. The modulations in the plasma density are related to the laser period. (bottom) Normalized longitudinal and transverse electric fields $\langle E_x \rangle$ and $\langle E_y \rangle$. The quantities have been averaged over ten laser periods. <i>Figure from Arefiev et al. (2016)</i>	36
1.15	(top) Electron trajectory and (bottom) γ as functions of ξ . Here, $a_0 = 8.5$. The colormap refers to the laser amplitude, while the arrows indicate the electron transverse velocity direction. <i>Figure from Arefiev et al. (2016)</i>	38
1.16	Trajectory of one accelerated particle. (top) Trajectory colored after the electron γ -factor. (bottom) Trajectory colored after the value of the longitudinal electric field $\langle E_x \rangle$ on the electron. The density and field colormaps are averaged over ten laser periods. <i>Figure from Arefiev et al. (2016)</i>	39
2.1	Depiction of a particle moving across the grid in the PIC approach. Here, the particle is described by a normalized triangular density profile g , whose width spans over twice the grid spacing.	46
2.2	FBPIC cycle. First, the electromagnetic field is gathered from the grid, then the particles are pushed. Secondly, the resulting charge and current are deposited on the grid. Finally, the electromagnetic field is updated. <i>Figure from fbpic.github.io</i>	48
2.3	Salle Jaune laser system architecture. <i>Figure adapted from Kabacinski (2022)</i>	50
2.4	(a) Electron spectrometer composed by a magnetic dipole that deviates the electrons on a Lanex Regular Carestream screen. Each electron interacts with the screen on a different position, depending on its energy. The light produced is then collected by a CCD camera. (b) Spectrometer calibration employed for the experiments discussed in Chapter 4. Here, we show the position of each electron s on the Lanex screen and the corresponding resolution as functions of the electrons' energy E	51

- 2.5 (a) Schematic view of the motorized Beam Profile Monitor. (b) Colorized image acquired with a 16-bit CCD Andor Solis camera of the BPM Lanex screen. From this image, we are able to determine the beam charge inside a given solid angle (dashed circle) and divergence. 52
- 2.6 Schematic depiction of the Phasics SID4 Camera: a laser pulse undergoes a phase shift traversing a plasma. The camera detects the dephasing that allows to reconstruct the density profile. 54
- 2.7 Example of density reconstruction. Here, we retrieve the plasma density profile produced with a supersonic nozzle. (a) Dephasing map obtained with the Phasics SID4 Camera. (b) Density map derived with Neutrino. In both images we show the inversion axis R . 55
- 2.8 (a) Focal spot camera scheme. Here, it is possible to observe the pick-up mirror, that deflects the laser pulse on a 8-bit CCD camera. This allows to control and correct for eventual aberrations and to estimate the laser FWHM diameter d , a_0 and energy within the laser central peak. (b-c) Images recorded with the CCD camera with a $f/4$ and $f/8$ off-axis parabola. 56
- 2.9 Exploded view of the dosimetry stack, composed by eleven GAFchromic EBT3 films. We separate each film with bricks in aluminum or Teflon of different thicknesses. The values on the image refer to the width of each brick in millimeters. (Inset) The stack was placed at 6 cm from the electron source in the experimental chamber. 56
- 2.10 (a) First four GAFchromic EBT3 films from the dosimetry stack, as indicated by the Roman numerals. (b) Calibration curve of the radiochromic films used in this thesis. 57
- 3.1 Schematic representation of a supersonic nozzle. Here, the fluid moves from left to right, following the arrows' direction. 60
- 3.2 Exit Mach number (M_e) as a function of the ratio S_e/S^* for nitrogen and monoatomic gases. 62
- 3.3 (a) Side and (b) top view of the glass nozzle we developed. (c) Example of glass nozzle tomography. Here, we can observe the inner structure at the middle plane. 63
- 3.4 2D-axisymmetric ANSYS Fluent simulation result. Here, the colormap represents the Mach number inside the supersonic nozzle. Further details about the simulation are provided in the text. 64

3.5	Estimated plasma density profiles along the radius r and at different heights from the nozzle exit.	64
3.6	(a) The permanent dipole used for the experiments discussed in chapter 4. In the inset, we show a view of the magnetic study conducted with CST Studio Suite, necessary for the dipole development. (b) Particle tracking simulation performed using the dipole middle plane magnetic field map. In this simulation, we have initialized five hundred electrons at 6 cm from the dipole, with energies between 1.2 MeV and 14.7 MeV.	65
3.7	Schematic representations on the role of a pinhole. (a) Case without the pinhole. Here, two electrons with energies $E_1 = E_2$ interact with the Lanex at two different positions s_1 and s_2 . (b) Introducing a pinhole makes sure that the electrons enter the magnetic field at the same position. This allows them to land at $s_1 \approx s_2$ on the Lanex.	67
3.8	Novel electron spectrometer prototype. Here, we underline the dipole entrance and the position of the two Lanex screens. In the inset we present a top view of the system.	68
3.9	(a) Magnetic field map measured at the dipole middle plane. (b) Measured and simulated magnetic field profiles along the x^* and y^* axes.	68
3.10	CST particle tracking results. (a) Results pertaining a 0.5 MeV, 400 mrad electron beam. (b) Results considering electrons between 0.5 MeV and 20 MeV with a maximum divergence of 400 mrad.	69
4.1	Simplified experimental setup, displaying the (a) beam profile monitor, allowing for beam charge and divergence measurements. (b) Setup for the electron spectrometer, which can be positioned on the laser axis using motorized stages, once the beam profile monitor has been removed. Here, we also notice the probe beam, used to perform plasma density or gas density measurements with a Phasics SID4 Camera.	73
4.2	(a) Experimental chamber and main diagnostics. We only show the driver path for visual purposes. (b) Close-up of the BPM and electron spectrometer.	74
4.3	Laser focal spot obtained with the $f/4$ OAP. The white curves represent the profiles through the laser intensity peak and d is the FWHM diameter. The dashed circle delineates the region considered for calculating the energy within the central spot	75

- 4.4 (a) Plasma density map obtained with the 0.4 mm exit diameter glass nozzle and a 10 bar backing pressure. The nozzle center is at $x = 0$ and its exit is at $y = 0$. (b) Plasma density profile measured across the white dashed line in (a), namely at $\sim 500 \mu\text{m}$ from the nozzle exit. 76
- 4.5 (a) Density map obtained with the 0.4 mm exit diameter nozzle at 80 bar. In this case, the density is retrieved assuming a full nitrogen L-shell ionization. (b) The light blue curve is the density profile measured across the white dashed line in (a), while the dark blue profile was extrapolated scaling the profile in Fig. 4.4(b) by a factor of eight. 77
- 4.6 (a) Density map obtained with a 2 mm exit diameter metallic nozzle at 60 bar. (b) Density profiles measured across the white dashed lines in (a), namely at 1 mm and 2 mm from the nozzle exit. 78
- 4.7 Charge-per-Joule in a given solid angle ($Q_{/J,\Omega}$) produced with the f/4 OAP. (a) Results obtained with the 0.4 mm nozzle for three different plasma densities and a 0.25 sr aperture. The curve at $n_e = 0.06 n_c$ was obtained with a 0.5 sr solid angle and the dashed curves refer to an FBPIC simulation set. (b) Results obtained with the 2 mm nozzle for three different plasma densities and a 0.5 sr aperture. 79
- 4.8 Charge-per-Joule in a given solid angle ($Q_{/J,\Omega}$) produced with the f/8 OAP. (a) Results obtained with the 0.4 mm nozzle for three different plasma densities and a 0.25 sr aperture. (b) Results obtained with the 2 mm nozzle for $n_e = 0.29 n_c$. Here, we show the charge-per-Joule measure at $n_e = 0.29 n_c$ with the f/4 OAP for comparison in a 0.5 sr solid angle. 80
- 4.9 Energy spectra obtained using the f/4 OAP with (a) the 0.4 mm nozzle at $n_e = 0.06 n_c$ and (b) with the 2 mm nozzle at $n_e = 0.29 n_c$ for different laser energies. The gray surface represents the detection limit. 82
- 4.10 Energy spectra measured at different horizontal positions using the f/4 OAP and the 2 mm nozzle, considering $n_e = 0.29 n_c$ and $E_L = 1 \text{ J}$. Here, Θ_x is the horizontal angle. The colored values represent the average energy of each corresponding spectrum. 82

- 4.11 Energy spectra obtained using the f/8 OAP with (a) the 0.4 mm nozzle at $n_e = 0.045 n_c$ and (b) with the 2 mm nozzle at $n_e = 0.29 n_c$ for different laser energies. The gray surface represents the detection limit. These spectra were obtained on two different days. 83
- 4.12 BPM images obtained with the 2 mm nozzle and f/4 OAP for (a) $n_e = 0.29 n_c$ and $E_L = 0.13$ J (b) $n_e = 0.29 n_c$ and $E_L = 1$ J (c) $n_e = 0.59 n_c$ and $E_L = 0.13$ J (d) $n_e = 0.59 n_c$ and $E_L = 1$ J. The value on each image refers to the FWHM beam divergence. The colored circles in (b) refer to the spectrometer sampling position, which allowed to retrieve the spectra in Fig. 4.10. Each image is normalized to its maximum value, with the white curves representing the transverse and longitudinal beam profiles passing through the peak of each image. 84
- 4.13 BPM images obtained with the 2 mm nozzle, f/8 OAP and at $n_e = 0.29 n_c$ for (a) $E_L = 0.13$ J (b) $E_L = 1$ J. Images obtained with the 2 mm nozzle, f/4 OAP and at $n_e = 0.29 n_c$ for (c) $E_L = 0.13$ J (d) $E_L = 1$ J. Each image is normalized to its maximum value, with the white curves representing the transverse and longitudinal beam profiles passing through the peak of each image. 85
- 4.14 Dose measurements setup. The film stack was placed in the vacuum chamber at 6 cm from the electron source. 86
- 4.15 (a-d) Dose maps numbered with respect to the film position in the stack obtained with the 2 mm nozzle for $n_e = 0.29 n_c$ and $E_L = 1$ J. (e) Average dose per shot on each film in a 20 mm diameter circle, as indicated by the dashed circles in (a-d), obtained with the 2 mm nozzle (blue curve) and 0.4 mm at $n_e = 0.06 n_c$ and $E_L = 1$ J (red curve). 87
- 5.1 FBPIC-Electric Work Profiler GitHub repository. 90
- 5.2 (a) 2D map of the laser pulse inside the co-moving box. (b) Longitudinal cut of the laser pulse map along the white dashed line in (a). It is possible to notice the laser centroid position with respect to the window's right boundary. 92
- 5.3 Schematic representation of FBPIC simulations in idealized conditions. 92

- 5.4 FBPIC results for $n_e = 0.06 n_c$. The gray colormap represents density snapshots at (a) $E_L = 0.12\text{J}$ and at (b) $E_L = 1\text{J}$. The red colormap represents the laser envelope, expressed in terms of the normalized vector potential. The insets refer to the laser transverse profile along the green dashed line. (c-d) Beam waist and normalized vector potential in plasma for $E_L = 0.12\text{J}$ and $E_L = 1\text{J}$ 93
- 5.5 (a) Maximum normalized vector potential in plasma ($a_{P,max}$) for different plasma densities and laser energies. The dots refer to the values obtained through FBPIC simulations, while the discontinuous lines in (a) have been obtained with Eq. (5.3) and in (b) with Eq. (5.4). 95
- 5.6 Pump depletion length (L_{pd}) for different densities, across different a_0 s. The dots represent the numerical results, while the dashed lines are a fit of the form $L_{pd}(\mu\text{m}) \approx 16 n_c/n_e$ 96
- 5.7 (1 – 4) Plasma density snapshots of four consecutive iterations. The gray and green colormaps refer to the L- and K-shell electron density. In red we depict a_P . These panels allow to observe the generation of a channel-like structure. 97
- 5.8 (a) Plasma density snapshot of the last panel of Fig. 5.7. The gray colormap refers to L-shell electrons, while the red one refers to the laser. (b) Radial wakefield map (E_r) and longitudinal wakefield (E_z) corresponding to the snapshot shown in (a). 98
- 5.9 Results with $E_L = 1\text{J}$ and (a1-2) $n_e = 0.06 n_c$ and (b1-2) $n_e = 0.18 n_c$. (a1, b1) The gray colormap refers to the L-shell electron density, while in red we represent a_P . (a2, b2) Radial wakefield in blue and red, while the black curve refers to the longitudinal wakefield. 99
- 5.10 (a) Example of one K-shell electron trajectory experiencing wakefield acceleration. (b) Wakefield longitudinal work (W_W^z), laser radial work (W_L^r) and kinetic energy curves (E) for the electron in (a). The circle in (a) refers to the instant $t^* = 100\text{fs}$, when the electron leaves the laser pulse and slips into the channel. 100
- 5.11 (a) Example of one K-shell electron trajectory experiencing direct laser acceleration. (b) Wakefield longitudinal work (W_W^z), laser radial work (W_L^r) and kinetic energy curves (E) for the electron in (a). The circle in (a) refers to the instant $t^* = 55\text{fs}$, when the electron is trapped in the front cavity and starts experiencing DLA. 101

- 5.12 (a) Example of two K-shell electron trajectories experiencing ponderomotive acceleration. (b) Wakefield radial work (W_W^r), laser radial work (W_L^r) and kinetic energy curves (E) for the electron denoted by the continuous trajectory in (a). The circle on this trajectory refers to the instant $t^* = 50$ fs, when the electron leaves the laser pulse. (c) Works and kinetic energy for the electron denoted by the dashed trajectory in (a). The circle on this trajectory refers to the instant $t^* = 83$ fs, when the electron leaves the laser pulse. 102
- 5.13 Example of two L-shell electron trajectories experiencing (continuous) ponderomotive acceleration and (dashed) wakefield acceleration. (b) Wakefield radial work, laser radial work and kinetic energy of the electron denoted with the continuous trajectory. At $t^* = 50$ fs the electron leaves the laser pulse. (c) Wakefield longitudinal work, laser radial work and kinetic energy of the electron denoted with the dashed trajectory. The electron leaves the laser pulse at $t^* = 90$ fs. 103
- 5.14 (a) Electron angular distribution. In the top half, the color refers to the parameter χ (see text), while in the bottom half, it represents the energy. The white circle represents a solid angle of 0.25 sr (see text). ($z - ct, E$) phase space for (b) K-shell electrons and (c) L-shell electrons. For visual reference, we show the plasma density and laser intensity. 105
- 5.15 Charge-per-Joule for the different configurations of interest, for electrons exceeding $E > 2$ MeV. The colormap is the linear interpolation of the simulations, while the white dashed lines refer to constant values of the charge-per-Joule. The blacked dotted lines highlight the region of charge-per-Joule saturation. (b) Examples of energy spectra. The continuous lines refer to the case at $E_L = 1$ J for $n_e = 0.03 n_c$ and $n_e = 0.06 n_c$. The dotted curves refer to the case at $E_L = 0.12$ J at $n_e = 0.03 n_c$ and $n_e = 0.06 n_c$ 106
- 5.16 Electron energy gain dynamics for $n_e = 0.03 n_c$, $n_e = 0.06 n_c$ and $n_e = 0.18 n_c$ at $E_L = 1$ J. From these curves, we estimate that the laser energy spent for ionizing and accelerating the electrons between 2 MeV and 15 MeV is around 0.21 J for the three densities, explaining the saturation effect in Fig 5.15(a). 107
- 5.17 Schematic representation of FBPIC simulations in the experimental conditions. 108

- 5.18 Beam waist and normalized vector potential in plasma for $n_e = 0.05 n_c$ and $E_L = 1$ J. The horizontal dotted line refers to $\lambda_p/2 = 1.8 \mu\text{m}$. For reference, we also illustrate the plasma density (gray area). 109
- 5.19 (1 – 4) Plasma density snapshots of four consecutive iterations. The gray and green colormaps refer to the L- and K-shell electron density. In red we depict a_P . Similar to the idealized case, these panels highlight the generation of a channel-like structure. The inset in (4) depicts the laser transverse profile along the green dashed line. The black dashed line is a visual reference for the plasma density peak. 110
- 5.20 (a) Plasma density snapshot of the last panel of Fig. 5.19. The gray colormap refers to L-shell electrons, the green to K-shell electrons and the red one refers to the laser. (b) Radial wakefield map (E_r) and longitudinal wakefield (E_z) corresponding to the snapshot shown in (a). 111
- 5.21 (a) Electron angular distribution. Each particle is colored based on its energy. (a) $(z - ct, E)$ phase space. The color of each electron refers to its radial divergence Θ_r (see text). (c) Electron beam energy spectrum. The white circle refers to a solid angle of 0.25 sr (see text). 112
- 5.22 (a) Salle Sheril experimental setup for bremsstrahlung X-ray generation. The tungsten plate is positioned at ~ 2 cm from the nozzle, the specimen at 40 cm and the imaging plate at 50 cm. (b) Resulting X-ray imaging plate tomography. 117

Appendix C

List of Publications and Contributions

Publications

Published: K. Oubrierie, A. Leblanc, O. Kononenko, R. Lahaye, I. A. Andriyash, J. Gautier, J.-P. Goddet, L. Martelli, A. Tafzi, K. T. Phuoc, S. Smartsev and C. Thaury. “Controlled acceleration of GeV electron beams in an all-optical plasma waveguide.” *Light Science & Applications*, **11**, 180 (2022).

Under review: L. Martelli, O. Kononenko, I. A. Andriyash, J. Gautier, J.-P. Goddet, A. Tafzi, J. Wheeler, R. Lahaye, C. Giaccaglia, A. Flacco, V. Tomkus, M. Mackevičiūtė, J. Dudutis, V. Stankevici, P. Gečys, G. Račiukaitis, H. Kraft, X.Q. Dinh and C. Thaury. “Highly-efficient electron ponderomotive acceleration in underdense plasmas.” (2024).

Presentations

Conference (Speaker): “Average Current Enhancement of Laser-Plasma Accelerators”, *SPIE Optics + Optoelectronics (EOO23)*, Prague, Czech Republic, April 26th, 2023.

Conference (Poster): “Average Current Enhancement of Laser-Plasma Accelerators”, *6th European Advanced Accelerator Concepts Workshop (EAAC2023)*, Isola d’Elba, Italy, September 20th, 2023.

Seminar: “Average Current Enhancement of Laser-Plasma Accelerators”, Deutsches Elektronen-Synchrotron, Hamburg, Germany, April 19th, 2024.

Prizes

Student Grant: “6th European Advanced Accelerator Concepts Workshop (EAAC2023)”, Isola d’Elba, Italy, September 20th, 2023.

Bibliography

- Akhiezer, A. I. and Polovin, R. V. (1956). Theory of wave motion of an electron plasma. *Soviet Phys. JETP*, 3.
- Albert, F. and Thomas, A. G. R. (2016). Applications of laser wakefield accelerator-based light sources. *Plasma Physics and Controlled Fusion*, 58(10):103001.
- Ammosov, M. V., Delone, N. B., and Krainov, V. P. (1986). Tunnel Ionization Of Complex Atoms And Atomic Ions In Electromagnetic Field. In Alcock, J. A., editor, *High Intensity Laser Processes*, volume 0664, pages 138 – 141. International Society for Optics and Photonics, SPIE.
- Andriyash, I., Lehe, R., Lifschitz, A., Thaury, C., Rax, J.-M., Krushelnick, K., and Malka, V. (2014). An ultracompact x-ray source based on a laser-plasma undulator. *Nature communications*, 5:4736.
- Andriyash, I., Thaury, C., and Flacco, A. (2024). Pulse-train laser-plasma accelerator. <https://patents.google.com/patent/US20240170232A1/en?q=US20240170232>. Patent.
- Arber, T. D., Bennett, K., Brady, C. S., Lawrence-Douglas, A., Ramsay, M. G., Sircombe, N. J., Gillies, P., Evans, R. G., Schmitz, H., Bell, A. R., and Ridgers, C. P. (2015). Contemporary particle-in-cell approach to laser-plasma modelling. *Plasma Physics and Controlled Fusion*, 57(11):113001.
- Arefiev, A. V., Khudik, V. N., Robinson, A. P. L., Shvets, G., Willingale, L., and Schollmeier, M. (2016). Beyond the ponderomotive limit: Direct laser acceleration of relativistic electrons in sub-critical plasmas. *Physics of Plasmas*, 23(5):056704.
- Ashland (2024). Gafchromic dosimetry media, type ebt-3. http://www.gafchromic.com/documents/EBT3_Specifications.pdf.
- Bauer, D. and Mulser, P. (1999). Exact field ionization rates in the barrier-suppression regime from numerical time-dependent schrödinger-equation calculations. *Phys. Rev. A*, 59:569–577.

- Behm, K., Hussein, A., Zhao, T. Z., Dann, S., Hou, B. X., Yanovsky, V., Nees, J., Maksimchuk, A., Schumaker, W., Thomas, A. G. R., and Krushelnick, K. (2019). Measurements of electron beam ring structures from laser wakefield accelerators. *Plasma Physics and Controlled Fusion*, 61(6):065012.
- Birdsall, C. and Langdon, A. (2004). *Plasma Physics via Computer Simulation*. Series in Plasma Physics and Fluid Dynamics. Taylor & Francis.
- Bisgaard, C. Z. and Madsen, L. B. (2004). Tunneling ionization of atoms. *American Journal of Physics*, 72(2):249–254.
- Boroumand, N., Thorpe, A., Parks, A. M., and Brabec, T. (2022). Keldysh ionization theory of atoms: mathematical details. *Journal of Physics B: Atomic, Molecular and Optical Physics*, 55(21):213001.
- Bracewell, R. (2000). *The Fourier Transform and Its Applications*. Circuits and systems. McGraw Hill.
- Brantov, A. V., Esirkepov, T. Z., Kando, M., Kotaki, H., Bychenkov, V. Y., and Bulanov, S. V. (2008). Controlled electron injection into the wake wave using plasma density inhomogeneity. *Physics of Plasmas*, 15(7):073111.
- Brijesh, P., Thaury, C., Phuoc, K. T., Corde, S., Lambert, G., Malka, V., Mangles, S. P. D., Bloom, M., and Kneip, S. (2012). Tuning the electron energy by controlling the density perturbation position in laser plasma accelerators. *Physics of Plasmas*, 19(6):063104.
- Brümmer, T., Bohlen, S., Grüner, F., Osterhoff, J., and Poder, K. (2022). Compact all-optical precision-tunable narrowband hard compton x-ray source. *Scientific Reports*, 12.
- Buck, A., Wenz, J., Xu, J., Khrennikov, K., Schmid, K., Heigoldt, M., Mikhailova, J. M., Geissler, M., Shen, B., Krausz, F., Karsch, S., and Veisz, L. (2013). Shock-front injector for high-quality laser-plasma acceleration. *Phys. Rev. Lett.*, 110:185006.
- Bulanov, S., Inovenkov, I., Kirsanov, V., Naumova, N., and Sakharov, A. (1992). Nonlinear depletion of ultrashort and relativistically strong laser pulses in an underdense plasma. *Physics of Fluids B: Plasma Physics*, 4:1935–1942.
- Bulanov, S., Naumova, N., Pegoraro, F., and Sakai, J. (1998). Particle injection into the wave acceleration phase due to nonlinear wake wave breaking. *Phys. Rev. E*, 58:R5257–R5260.

- Bulanov, S. V., Pegoraro, F., Pukhov, A. M., and Sakharov, A. S. (1997). Transverse-wake wave breaking. *Phys. Rev. Lett.*, 78:4205–4208.
- Chen, M., Cormier-Michel, E., Geddes, C., Bruhwiler, D., Yu, L., Esarey, E., Schroeder, C., and Leemans, W. (2013). Numerical modeling of laser tunneling ionization in explicit particle-in-cell codes. *Journal of Computational Physics*, 236:220–228.
- Chen, M., Cormier-Michel, E., Geddes, C. G. R., Bruhwiler, D. L., Yu, L. L., Esarey, E., Schroeder, C. B., and Leemans, W. P. (2013). Numerical modeling of laser tunneling ionization in explicit particle-in-cell codes. *Journal of Computational Physics*, 236:220–228.
- Chen, M., Esarey, E., Schroeder, C., Geddes, C., and Leemans, W. (2012). Theory of ionization-induced trapping in laser-plasma accelerators. *Physics of Plasmas*, 19.
- Cole, J. M., Symes, D. R., Lopes, N. C., Wood, J. C., Poder, K., Alatabi, S., Botchway, S. W., Foster, P. S., Gratton, S., Johnson, S., Kamperidis, C., Kononenko, O., Lazzari, M. D., Palmer, C. A. J., Rusby, D., Sanderson, J., Sandholzer, M., Sarri, G., Szoke-Kovacs, Z., Teboul, L., Thompson, J. M., Warwick, J. R., Westerberg, H., Hill, M. A., Norris, D. P., Mangles, S. P. D., and Najmudin, Z. (2018). High-resolution μct of a mouse embryo using a compact laser-driven x-ray betatron source. *Proceedings of the National Academy of Sciences*, 115(25):6335–6340.
- Corde, S., Ta Phuoc, K., Lambert, G., Fitour, R., Malka, V., Rousse, A., Beck, A., and Lefebvre, E. (2013a). Femtosecond x rays from laser-plasma accelerators. *Rev. Mod. Phys.*, 85:1–48.
- Corde, S., Thaury, C., Lifschitz, A., Lambert, G., Phuoc, K., Davoine, X., Lehe, R., Douillet, D., Rousse, A., and Malka, V. (2013b). Observation of longitudinal and transverse self-injections in laser-plasma accelerators. *Nature communications*, 4:1501.
- Couperus Cabadağ, J., Pausch, R., Köhler, A., Zarini, O., Krämer, J., Garten, M., Huebl, A., Gebhardt, R., Helbig, U., Bock, S., Zeil, K., Debus, A., Bussmann, M., Schramm, U., and Irman, A. (2017). Demonstration of a beam loaded nanocoulomb-class laser wakefield accelerator. *Nature Communications*, 8:487.
- Dawson, J. M. (1959). Nonlinear electron oscillations in a cold plasma. *Phys. Rev.*, 113:383–387.
- Dawson, J. M. (1983). Particle simulation of plasmas. *Rev. Mod. Phys.*, 55:403–447.

- Doepf, A., Guillaume, E., Thaur, C., Lifschitz, A., Sylla, F., Goddet, J.-P., Tafzi, A., Iaquanello, G., Lefrou, T., Rousseau, P., Conejero, E., Ruiz, C., Phuoc, K., and Malka, V. (2016). A bremsstrahlung gamma-ray source based on stable ionization injection of electrons into a laser wakefield accelerator. *Nuclear Instruments and Methods in Physics Research Section A Accelerators Spectrometers Detectors and Associated Equipment*, 830.
- Edwards, R. D., Sinclair, M. A., Goldsack, T. J., Krushelnick, K., Beg, F. N., Clark, E. L., Dangor, A. E., Najmudin, Z., Tatarakis, M., Walton, B., Zepf, M., Ledingham, K. W. D., Spencer, I., Norreys, P. A., Clarke, R. J., Kodama, R., Toyama, Y., and Tampo, M. (2002). Characterization of a gamma-ray source based on a laser-plasma accelerator with applications to radiography. *Applied Physics Letters*, 80(12):2129–2131.
- Esarey, E., Schroeder, C. B., and Leemans, W. P. (2009). Physics of laser-driven plasma-based electron accelerators. *Rev. Mod. Phys.*, 81:1229–1285.
- Esarey, E., Sprangle, P., Krall, J., and Ting, A. (1996). Overview of plasma-based accelerator concepts. *IEEE Transactions on Plasma Science*, 24(2):252–288.
- Esarey, E., Ting, A., and Sprangle, P. (1990). Frequency shifts induced in laser pulses by plasma waves. *Phys. Rev. A*, 42:3526–3531.
- Esirkepov, T., Bulanov, S. V., Yamagiwa, M., and Tajima, T. (2006). Electron, positron, and photon wakefield acceleration: Trapping, wake overtaking, and ponderomotive acceleration. *Phys. Rev. Lett.*, 96:014803.
- Faure, J. (2016). Plasma injection schemes for laser–plasma accelerators. *Proceedings of the CAS-CERN Accelerator School: Plasma Wake Acceleration, Geneva, Switzerland, 23–29 November 2014*, 1.
- Faure, J., Glinec, Y., Pukhov, A., Kiselev, S., Gordienko, S., Lefebvre, E., Rousseau, J.-P., Burgi, f., and Malka, V. (2004). A laser-plasma accelerator producing monoenergetic electron beams. *Nature*, 431:541–4.
- Faure, J., Rechatin, C., Lundh, O., Ammoura, L., and Malka, V. (2010). Injection and acceleration of quasimonoenergetic relativistic electron beams using density gradients at the edges of a plasma channel. *Physics of Plasmas*, 17(8):083107.
- Feng, J., Li, Y., Tan, J., Wang, W., Li, Y., Zhang, X., Meng, Y., Ge, X., Liu, F., Yan, W., Fu, C., Chen, L., and Zhang, J. (2023). Laser plasma-accelerated ultra-intense electron beam for efficiently exciting nuclear isomers. *Laser & Photonics Reviews*.

- Flacco, A. (2013). Neutrino: A light, expandable and full-featured image analysis tool for research. <https://github.com/NeutrinoToolkit/Neutrino>.
- Geddes, C., Toth, C., Tilborg, J., Esarey, E., Schroeder, C., Bruhwiler, D., Nieter, C., Cary, J., and Leemans, W. (2004). High-quality electron beams from a laser wakefield accelerator using plasma-channel guiding. *Nature*, 431:538–41.
- Geddes, C. G. R., Nakamura, K., Plateau, G. R., Toth, C., Cormier-Michel, E., Esarey, E., Schroeder, C. B., Cary, J. R., and Leemans, W. P. (2008). Plasma-density-gradient injection of low absolute-momentum-spread electron bunches. *Phys. Rev. Lett.*, 100:215004.
- Gibbon, P. (2005). *Short Pulse Laser Interactions with Matter: An Introduction*. Imperial College Press.
- Gibbon, P. (2012). Physics of high intensity laser-plasma interactions. *La Rivista del Nuovo Cimento*, 35:607.
- Glinec, Y., Faure, J., Dain, L. L., Darbon, S., Hosokai, T., Santos, J. J., Lefebvre, E., Rousseau, J. P., Burgy, F., Mercier, B., and Malka, V. (2005). High-resolution γ -ray radiography produced by a laser-plasma driven electron source. *Phys. Rev. Lett.*, 94:025003.
- Gorbunov, L. and Kirsanov, V. (1987). The excitation of plasma waves by an electromagnetic wave packet. *Zhurnal Eksperimentalnoi i Teoreticheskoi Fiziki*, 93:509–518.
- Gordon, D., Tzeng, K. C., Clayton, C. E., Dangor, A. E., Malka, V., Marsh, K. A., Modena, A., Mori, W. B., Muggli, P., Najmudin, Z., Neely, D., Danson, C., and Joshi, C. (1998). Observation of electron energies beyond the linear dephasing limit from a laser-excited relativistic plasma wave. *Phys. Rev. Lett.*, 80:2133–2136.
- Götzfried, J., Döpp, A., Gilljohann, M. F., Foerster, F. M., Ding, H., Schindler, S., Schilling, G., Buck, A., Veisz, L., and Karsch, S. (2020). Physics of high-charge electron beams in laser-plasma wakefields. *Phys. Rev. X*, 10:041015.
- Griffiths, D., Ciccacci, F., and Quartapelle, L. (2005). *Introduzione alla meccanica quantistica*. CEA.
- Guillaume, E., Döpp, A., Thaury, C., Lifschitz, A., Goddet, J.-P., Tafzi, A., Sylla, F., Iaquanello, G., Lefrou, T., Rousseau, P., Phuoc, K. T., and Malka, V. (2015). Physics of fully-loaded laser-plasma accelerators. *Phys. Rev. ST Accel. Beams*, 18:061301.

- Gurnett, D. and Bhattacharjee, A. (2005). *Introduction to Plasma Physics: With Space and Laboratory Applications*. Cambridge University Press.
- Hafizi, B., Ting, A., Sprangle, P., and Hubbard, R. F. (2000). Relativistic focusing and ponderomotive channeling of intense laser beams. *Phys. Rev. E*, 62:4120–4125.
- Hansen, J. L. (2012). *Imaging Molecular Fram Dynamics Using Spatially Oriented Molecules*. PhD Dissertation, Aarhus University.
- He, Z.-H., Hou, B., Nees, J. A., Easter, J. H., Faure, J., Krushelnick, K., and Thomas, A. G. R. (2013). High repetition-rate wakefield electron source generated by few-millijoule, 30 fs laser pulses on a density downramp. *New Journal of Physics*, 15(5):053016.
- Jalas, S., Kirchen, M., Messner, P., Winkler, P., Hübner, L., Dirkwinkel, J., Schnepf, M., Lehe, R., and Maier, A. R. (2021). Bayesian optimization of a laser-plasma accelerator. *Phys. Rev. Lett.*, 126:104801.
- Kabacinski, A. (2022). *Physique et application d'une source cohérente femtoseconde à 32.8nm par interaction laser-plasma*. PhD thesis. Institut Polytechnique de Paris.
- Kalmykov, S., Yi, S. A., Khudik, V., and Shvets, G. (2009). Electron self-injection and trapping into an evolving plasma bubble. *Phys. Rev. Lett.*, 103:135004.
- Katsouleas, T. (1986). Physical mechanisms in the plasma wake-field accelerator. *Phys. Rev. A*, 33.
- Katsouleas, T. and Mori, W. B. (1988). Wave-breaking amplitude of relativistic oscillations in a thermal plasma. *Phys. Rev. Lett.*, 61:90–93.
- Keldysh, L. V. (1964). Ionization in the field of a strong electromagnetic wave. *J. Exp. Theor. Phys*, 47.
- Kiani, L., Zhou, T., Bahk, S.-W., Bromage, J., Bruhwiler, D., Campbell, E. M., Chang, Z., Chowdhury, E., Downer, M., Du, Q., Esarey, E., Galvanauskas, A., Galvin, T., Häfner, C., Hoffmann, D., Joshi, C., Kanskar, M., Lu, W., Menoni, C., Messerly, M., Mirov, S. B., Palmer, M., Pogorelsky, I., Polyanskiy, M., Power, E., Reagan, B., Rocca, J., Rothenberg, J., Schmidt, B. E., Sistrunk, E., Spinka, T., Tochitsky, S., Vafaei-Najafabadi, N., van Tilborg, J., Wilcox, R., Zuegel, J., and Geddes, C. (2023). High average power ultrafast laser technologies for driving future advanced accelerators. *Journal of Instrumentation*, 18(08):T08006.

- Kogelnik, H. and Li, T. (1966). Laser beams and resonators. *Applied optics*, 5 10:1550–67.
- Kostyukov, I., Nerush, E., Pukhov, A., and Sereedov, V. (2010). A multidimensional theory for electron trapping by a plasma wake generated in the bubble regime. *New Journal of Physics*, 12(4):045009.
- Kostyukov, I., Pukhov, A., and Kiselev, S. (2004). Phenomenological theory of laser-plasma interaction in “bubble” regime. *Physics of Plasmas*, 11(11):5256–5264.
- Krall, J., Ting, A., Esarey, E., and Sprangle, P. (1993). Self-modulated-laser wakefield acceleration. *Proceedings of International Conference on Particle Accelerators*, pages 2629–2631 vol.4.
- Kruer, W. (2019). *The Physics Of Laser Plasma Interactions*. CRC-Press.
- Kurz, T., Couperus, J., Krämer, J., et al. (2018). Calibration and cross-laboratory implementation of scintillating screens for electron bunch charge determination. *Review of Scientific Instruments*, 89(9):093303.
- LakeShore (2004). Lake shore model 421 gaussmeter user’s manual. https://www.lakeshore.com/docs/default-source/product-downloads/421_manual.pdf?sfvrsn=df2b523_1.
- Landau, L. and Lifshitz, E. (1969). *Meccanica quantistica: teoria non relativistica*. Programma di matematica, fisica, elettronica. Boringhieri.
- Leemans, W. P., Nagler, B., Gonsalves, A. J., Tóth, C., Nakamura, K., Geddes, C. G. R., Esarey, E., Schroeder, C. B., and Hooker, S. M. (2006). GeV electron beams from a centimetre-scale accelerator. *Nature Physics*, 2(10):696–699.
- Lehe, R., Kirchen, M., Andriyash, I. A., Godfrey, B. B., and Vay, J.-L. (2016). A spectral, quasi-cylindrical and dispersion-free particle-in-cell algorithm. *Computer Physics Communications*, 203:66–82.
- Lehe, R., Lifschitz, A., Thaury, C., Malka, V., and Davoine, X. (2013). Numerical growth of emittance in simulations of laser-wakefield acceleration. *Phys. Rev. ST Accel. Beams*, 16:021301.
- Lide, D. (1995). *CRC Handbook of Chemistry and Physics: A Ready-reference Book of Chemical and Physical Data*. CRC-Press.

- Lifschitz, A., Davoine, X., Lefebvre, E., Faure, J., Rechatin, C., and Malka, V. (2009). Particle-in-cell modelling of laser–plasma interaction using fourier decomposition. *Journal of Computational Physics*, 228(5):1803–1814.
- Lu, W., Huang, C., Zhou, M., Mori, W. B., and Katsouleas, T. (2006). Nonlinear theory for relativistic plasma wakefields in the blowout regime. *Phys. Rev. Lett.*, 96:165002.
- Lu, W., Tzoufras, M., Joshi, C., Tsung, F. S., Mori, W. B., Vieira, J., Fonseca, R. A., and Silva, L. O. (2007). Generating multi-gev electron bunches using single stage laser wakefield acceleration in a 3d nonlinear regime. *Phys. Rev. ST Accel. Beams*, 10:061301.
- Macchi, A. (2013). *A Superintense Laser-Plasma Interaction Theory Primer*. SpringerBriefs in Physics. Springer Netherlands.
- Maier, A. R., Delbos, N. M., Eichner, T., Hübner, L., Jalas, S., Jeppe, L., Jolly, S. W., Kirchen, M., Leroux, V., Messner, P., Schnepf, M., Trunk, M., Walker, P. A., Werle, C., and Winkler, P. (2020). Decoding sources of energy variability in a laser-plasma accelerator. *Phys. Rev. X*, 10:031039.
- Mainfray, G. and Manus, G. (1991). Multiphoton ionization of atoms. *Reports on Progress in Physics*, 54(10):1333.
- Malka, V., Fritzler, S., Lefebvre, E., Aleanard, M.-M., Burgy, F., Chambaret, J.-P., Chemin, J.-F., Krushelnick, K., Malka, G., Mangles, S. P. D., Najmudin, Z., Pittman, M., Rousseau, J.-P., Scheurer, J.-N., Walton, B., and Dangor, A. E. (2002). Electron acceleration by a wake field forced by an intense ultrashort laser pulse. *Science*, 298(5598):1596–1600.
- Mangles, S., Murphy, C., Najmudin, Z., Thomas, A., Collier, J., Dangor, A., Divall, E., Foster, P., Gallacher, J., Hooker, C., Jaroszynski, D., Langley, A., Mori, W., Norreys, P., Tsung, F., Viskup, R., Walton, B., and Krushelnick, K. (2004). Monoenergetic beams of relativistic electrons from intense laser-plasma interactions. *Nature*, 431(7008):535–538.
- Mangles, S., Thomas, A., Bellei, C., Dangor, A., Kamperidis, C., Kneip, S., Nagel, S., Willingale, L., and Najmudin, Z. (2008). Self-guided wakefield experiments driven by petawatt-class ultrashort laser pulses. *Plasma Science, IEEE Transactions on*, 36:1715 – 1721.
- Martelli, L. and Andriyash, I. (2024). laumrt/fbpic-ewp: Fbpic-ewp.

- McGuffey, C., Thomas, A. G. R., Schumaker, W., Matsuoka, T., Chvykov, V., Dollar, F. J., Kalintchenko, G., Yanovsky, V., Maksimchuk, A., Krushelnick, K., Bychenkov, V. Y., Glazyrin, I. V., and Karpeev, A. V. (2010). Ionization induced trapping in a laser wakefield accelerator. *Phys. Rev. Lett.*, 104:025004.
- Modena, A., Najmudin, Z., Dangor, A. E., Clayton, C. E., Marsh, K. A., Joshi, C., Malka, V., Darrow, C. B., Danson, C., Neely, D., and Walsh, F. N. (1995). Electron acceleration from the breaking of relativistic plasma waves. *Nature*, 377(6550):3.
- Mora, P. and Antonsen, Jr., T. M. (1997). Kinetic modeling of intense, short laser pulses propagating in tenuous plasmas. *Physics of Plasmas*, 4(1):217–229.
- Mori, W. (1997). The physics of the nonlinear optics of plasmas at relativistic intensities for short-pulse lasers. *IEEE Journal of Quantum Electronics*, 33(11):1942–1953.
- Multiscan 3D project (2020). European Commission, Horizon - 2020. <https://multiscan3d-h2020.eu/>.
- Osterhoff, J. (2009). *Stable, ultra-relativistic electron beams by laser-wakefield acceleration. PhD thesis.* LMU.
- Oubrierie, K. (2022). *Amélioration de l'efficacité des accélérateurs laser-plasma. PhD thesis.* Institut Polytechnique de Paris.
- Oubrierie, K., Leblanc, A., Kononenko, O., Lahaye, R., Andriyash, I., Gautier, J., Goddet, J.-P., Martelli, L., Tafzi, A., Phuoc, K., Smartsev, S., and Thauray, C. (2022). Controlled acceleration of gev electron beams in an all-optical plasma waveguide. *Light: Science & Applications*, 11:180.
- Pak, A., Marsh, K. A., Martins, S. F., Lu, W., Mori, W. B., and Joshi, C. (2010). Injection and trapping of tunnel-ionized electrons into laser-produced wakes. *Phys. Rev. Lett.*, 104:025003.
- Pellegrina, A., Jeandet, A., Lavenu, L., Ricaud, S., Simon-Boisson, C., Vernier, A., Flacco, A., and Faure, J. (2022). High average power tisa amplifier for high energy, high repetition rate laser plasma accelerator. In *Optica High-brightness Sources and Light-driven Interactions Congress 2022*, page HW4B.6. Optica Publishing Group.
- Phuoc, K., Corde, S., Thauray, C., Malka, V., Tafzi, A., Goddet, J.-P., Shah, R., Sebban, S., and Rousse, A. (2012). All-optical compton gamma-ray source. *Nature Photonics*, 6:308–311.

- Pollock, B. B., Clayton, C. E., Ralph, J. E., Albert, F., Davidson, A., Divol, L., Filip, C., Glenzer, S. H., Herpoldt, K., Lu, W., Marsh, K. A., Meinecke, J., Mori, W. B., Pak, A., Rensink, T. C., Ross, J. S., Shaw, J., Tynan, G. R., Joshi, C., and Froula, D. H. (2011). Demonstration of a narrow energy spread, ~ 0.5 GeV electron beam from a two-stage laser wakefield accelerator. *Phys. Rev. Lett.*, 107:045001.
- Primot, J. and Sogno, L. (1995). Achromatic three-wave (or more) lateral shearing interferometer. *J. Opt. Soc. Am. A*, 12(12):2679–2685.
- Pucella, G. and Segre, S. (2009). *Fisica dei plasmi*. Fisica sperimentale. Zanichelli.
- Pukhov, A. and Meyer-ter Vehn, J. (2002). Laser wakefield acceleration: The highly non-linear broken-wave regime. *Applied Physics B-Lasers and Optics*, v.74, 355-361 (2002), 74.
- Pukhov, A., Sheng, Z.-M., and Meyer-ter Vehn, J. (1999). Particle acceleration in relativistic laser channels. *Physics of Plasmas*, 6(7):2847–2854.
- Robinson, A. P. L., Arefiev, A. V., and Neely, D. (2013). Generating “superponderomotive” electrons due to a non-wake-field interaction between a laser pulse and a longitudinal electric field. *Phys. Rev. Lett.*, 111:065002.
- Rousse, A., Phuoc, K. T., Shah, R., Pukhov, A., Lefebvre, E., Malka, V., Kiselev, S., Burgy, F., Rousseau, J.-P., Umstadter, D., and Hulin, D. (2004). Production of a keV x-ray beam from synchrotron radiation in relativistic laser-plasma interaction. *Phys. Rev. Lett.*, 93:135005.
- Rovige, L., Huijts, J., Andriyash, I., Vernier, A., Tomkus, V., Girdauskas, V., Raciukaitis, G., Dudutis, J., Stankevicius, V., Gecys, P., Ouille, M., Cheng, Z., Lopez-Martens, R., and Faure, J. (2020). Demonstration of stable long-term operation of a kilohertz laser-plasma accelerator. *Phys. Rev. Accel. Beams*, 23:093401.
- Schmid, K., Buck, A., Sears, C. M. S., Mikhailova, J. M., Tautz, R., Herrmann, D., Geissler, M., Krausz, F., and Veisz, L. (2010a). Density-transition based electron injector for laser driven wakefield accelerators. *Phys. Rev. ST Accel. Beams*, 13:091301.
- Schmid, K., Buck, A., Sears, C. M. S., Mikhailova, J. M., Tautz, R., Herrmann, D., Geissler, M., Krausz, F., and Veisz, L. (2010b). Density-transition based electron injector for laser driven wakefield accelerators. *Phys. Rev. ST Accel. Beams*, 13:091301.

- Schmid, K. and Veisz, L. (2012). Supersonic gas jets for laser-plasma experiments. *Review of Scientific Instruments*, 83(5):053304.
- Schroeder, C. B., Esarey, E., and Shadwick, B. A. (2005). Warm wave breaking of nonlinear plasma waves with arbitrary phase velocities. *Phys. Rev. E*, 72:055401.
- Semushin, S. and Malka, V. (2001). High density gas jet nozzle design for laser target production. *Review of Scientific Instruments*, 72(7):2961–2965.
- Shadwick, B. A., Schroeder, C. B., and Esarey, E. (2009). Nonlinear laser energy depletion in laser-plasma accelerators. *Physics of Plasmas*, 16(5):056704.
- Shaw, J. L., Lemos, N., Marsh, K. A., Tsung, F. S., Mori, W. B., and Joshi, C. (2016). Estimation of direct laser acceleration in laser wakefield accelerators using particle-in-cell simulations. *Plasma Physics and Controlled Fusion*, 58(3):034008.
- Shaw, J. L., Tsung, F. S., Vafaei-Najafabadi, N., Marsh, K. A., Lemos, N., Mori, W. B., and Joshi, C. (2014). Role of direct laser acceleration in energy gained by electrons in a laser wakefield accelerator with ionization injection. *Plasma Physics and Controlled Fusion*, 56(8):084006.
- Shimoda, K. (1986). *Introduction to Laser Physics*. Springer.
- Siegman, A. (1986). *Lasers*. University Science Books.
- Sprangle, P., Ting, A., Esarey, E., and Fisher, A. (1992). Tunable, short pulse hard x-rays from a compact laser synchrotron source. *Journal of Applied Physics*, 72(11):5032–5038.
- Sprangle, P., Ting, A., and Tang, C. (1987). Radiation focusing and guiding in the free electron laser. *Nuclear Instruments and Methods in Physics Research Section A: Accelerators, Spectrometers, Detectors and Associated Equipment*, 259(1):136–142.
- Strickland, D. and Mourou, G. (1985). Compression of amplified chirped optical pulses. *Optics Communications*, 56(3):219–221.
- Suk, H., Barov, N., Rosenzweig, J. B., and Esarey, E. (2001). Plasma electron trapping and acceleration in a plasma wake field using a density transition. *Phys. Rev. Lett.*, 86:1011–1014.
- Suk, H., Lee, H. J., and Ko, I. S. (2004). Generation of high-energy electrons by a femtosecond terawatt laser propagating through a sharp downward density transition. *J. Opt. Soc. Am. B*, 21(7):1391–1396.

- Svelto, O. (2010). *Principles of Lasers*. Springer US.
- Svensden, K., González, I. G., Hansson, M., Svensson, J. B., Ekerfelt, H., Persson, A., and Lundh, O. (2018). Optimization of soft x-ray phase-contrast tomography using a laser wakefield accelerator. *Opt. Express*, 26(26):33930–33941.
- Tajima, T. and Dawson, J. M. (1979). Laser electron accelerator. *Phys. Rev. Lett.*, 43:267–270.
- Thomas, A. G. R., Najmudin, Z., Mangles, S. P. D., Murphy, C. D., Dangor, A. E., Kamperidis, C., Lancaster, K. L., Mori, W. B., Norreys, P. A., Rozmus, W., and Krushelnick, K. (2007). Effect of laser-focusing conditions on propagation and monoenergetic electron production in laser-wakefield accelerators. *Phys. Rev. Lett.*, 98:095004.
- Thévenet, M., Leblanc, A., Kahaly, S., Vincenti, H., Vernier, A., Quéré, F., and Faure, J. (2016). Vacuum laser acceleration of relativistic electrons using plasma mirror injectors. *Nature Physics*, 12(4):355–360.
- Tomkus, V., Girdauskas, V., Dudutis, J., Gecys, P., Stankevič, V., and Raciukaitis, G. (2018). High-density gas capillary nozzles manufactured by hybrid 3d laser machining technique from fused silica. *Optics Express*, 26:27965.
- U.S. Food and Drug Administration (1977). Code of federal regulations, title 21, chapter i, subchapter b, part 179. <https://www.ecfr.gov/current/title-21/chapter-I/subchapter-B/part-179>.
- Verluse, F., Laude, V., Cheng, Z., Spielmann, C., and Tournois, P. (2000). Amplitude and phase control of ultrashort pulses by use of an acousto-optic programmable dispersive filter: pulse compression and shaping. *Opt. Lett.*, 25(8):575–577.
- Vlasov, A. A. (1968). The vibrational properties of an electron gas. *Soviet Physics Uspekhi*, 10(6):721.
- Xie, B.-S., Wu, H.-C., Wang, H., Wang, N.-Y., and Yu, M. Y. (2007). Analysis of the electromagnetic fields and electron acceleration in the bubble regime of the laser-plasma interaction. *Physics of Plasmas*, 14(7):073103.
- Yang, X., Brunetti, E., Gil, D. R., Welsh, G. H., Li, F. Y., Cipiccia, S., Ersfeld, B., Grant, D. W., Grant, P. A., Islam, M. R., Tooley, M. P., Vieux, G., Wiggins, S. M., Sheng, Z. M., and Jaroszynski, D. A. (2017). Three electron beams from a laser-plasma wakefield accelerator and the energy apportioning question. *Scientific Reports*, 7(1):43910.

Zucker, R. and Biblarz, O. (2019). *Fundamentals of Gas Dynamics*. Wiley.

Titre : Augmentation du courant moyen des accélérateurs laser-plasma pour applications industrielles

Mots clés : Accélérateurs laser-plasma, Faisceaux d'électrons à haute charge, Faisceaux d'électrons à basse énergie, Applications industrielles

Résumé : Cette thèse de doctorat s'inscrit dans le cadre d'une collaboration CIFRE entre Thales AVS-MIS et le Laboratoire d'Optique Appliquée (LOA). L'objectif principal est d'améliorer le courant moyen des accélérateurs laser-plasma à faible énergie, notamment dans la gamme de quelques MeV. Cette avancée revêt un intérêt particulier pour les applications à faible énergie telles que celles proposées par le projet européen *Multiscan 3D - Horizon 2020*, dédié au développement d'une source de rayons X laser-plasma pour le contrôle du fret aux douanes.

Des expériences ont été menées au moyen du système laser de 60 TW installé dans la Salle Jaune du LOA, capable de générer des impulsions de 30 fs. À travers une exploration minutieuse des densités de plasma, des énergies laser, des cibles gazeuses et des degrés de focalisation, nous avons identifié les conditions propices à la production de faisceaux d'électrons hautement divergents (i.e., > 100 mrad) de quelques MeV, avec des charges variant de 5

à 30 nC. Nous avons également atteint une efficacité maximale de conversion d'énergie laser-électron d'environ 14 %, parmi les plus élevées jamais mesurées. En envisageant les futurs systèmes laser capables d'atteindre des puissances moyennes d'environ 100 W, ces configurations pourraient ouvrir la voie à la réalisation de faisceaux d'électrons accélérés par laser-plasma, avec des courants moyens dépassant 1 microampère, surpassant ainsi l'état de l'art actuel des accélérateurs laser-plasma.

Parallèlement aux expériences, cette thèse a également approfondi les simulations Particle-In-Cell (PIC) pour étudier les mécanismes d'accélération. Grâce à un outil numérique spécifiquement développé pour traiter les résultats des simulations PIC, nous avons démontré que la force pondéromotrice du laser joue un rôle prépondérant dans l'accélération des électrons. Notamment, la majorité des particules ne sont pas injectées dans les ondes du plasma, mais glissent plutôt sur l'impulsion laser, acquérant ainsi une faible énergie de l'ordre de quelques MeV.

Title : Average current enhancement of laser-plasma accelerators for industrial applications

Keywords : Laser-plasma accelerators, High-charge electron beams, Low-energy electron beams, Industrial applications

Abstract : This doctoral thesis is part of a CIFRE collaboration between Thales AVS-MIS and the Laboratoire d'Optique Appliquée (LOA). The main objective is to enhance the average current of low-energy laser-plasma accelerators, particularly in the range of a few-MeV. This advancement is of particular interest for low-energy applications, such as those proposed by the European project *Multiscan 3D - Horizon 2020*, dedicated to developing a laser-plasma X-ray source for freight inspection.

Experiments were conducted using the 60 TW laser system installed in the Salle Jaune at LOA, capable of generating 30 fs pulses. Through meticulous exploration of plasma densities, laser energies, gas targets, and focusing degrees, we identified conditions conducive to producing highly divergent electron beams (i.e., > 100 mrad) of a few-MeV, with charges ranging from 5 to 30 nC. We also achieved a maximum laser-

to-electron energy conversion efficiency of approximately 14 %, one of the highest ever measured. Looking ahead to future laser systems capable of achieving average powers of around 100 W, these configurations could pave the way for laser-plasma accelerated electron beams with average currents exceeding 1 microampere, surpassing the current state of the art in laser-plasma accelerators.

In parallel with the experiments, this thesis also delved into Particle-In-Cell (PIC) simulations to study acceleration mechanisms. Using a numerical tool specifically developed to process PIC simulation results, we demonstrated that the ponderomotive force of the laser plays a crucial role in electron acceleration. Notably, the majority of particles are not injected into plasma waves but rather slide on the laser pulse, acquiring low energies on the order of a few-MeV.